

Fast Charging of Lithium-Ion Batteries: A Review of Materials Aspects

Manuel Weiss, Raffael Ruess, Johannes Kasnatscheew, Yehonatan Levartovsky, Natasha Ronith Levy, Philip Minnmann, Lukas Stolz, Thomas Waldmann, Margret Wohlfahrt-Mehrens, Doron Aurbach, Martin Winter, Yair Ein-Eli,* and Jürgen Janek*

Fast charging is considered to be a key requirement for widespread economic success of electric vehicles. Current lithium-ion batteries (LIBs) offer high energy density enabling sufficient driving range, but take considerably longer to recharge than traditional vehicles. Multiple properties of the applied anode, cathode, and electrolyte materials influence the fast-charging ability of a battery cell. In this review, the physicochemical basics of different material combinations are considered in detail, identifying the transport of lithium inside the electrodes as the crucial rate-limiting steps for fast-charging. Lithium diffusion within the active materials inherently slows down the charging process and causes high overpotentials. In addition, concentration polarization by slow lithium-ion transport within the electrolyte phase in the porous electrodes also limits the charging rate. Both kinetic effects are responsible for lithium plating observed on graphite anodes. Conclusions drawn from potential and concentration profiles within LIB cells are complemented by extensive literature surveys on anode, cathode, and electrolyte materials—including solid-state batteries. The advantages and disadvantages of typical LIB materials are analyzed, resulting in suggestions for optimum properties on the material and electrode level for fast-charging applications. Finally, limitations on the cell level are discussed briefly as well.

1. Introduction

1.1. Aims, Scope, and Framework

A dozen senior battery and supercapacitor expert scientists, and approximately 30 Ph.D. students and postdoctoral fellows from both Israel and Germany gathered in 2019, in the frame of the 4th German-Israeli Battery School (GIBS 4) in Berlin, Germany. The Berlin workshop was focused on in-depth discussions on four “hot subjects,” including the following topics: 1) How will the far future of electrochemical power sources be after the lithium era, if ever? 2) Will the future of portable power sources be based on liquid or solid electrolytes? 3) Fuel cells versus battery technologies—complementary or competitors? And lastly, the 4th topic of fast charging—a reality or just a dream?

Here, we bring to the readers the outcome of Group 4 discussions that continued over the last two years on fast charging and materials aspects from a physicochemical point of view.

Dr. M. Weiss, Dr. R. Ruess, P. Minnmann, Prof. J. Janek
Institute of Physical Chemistry
Justus Liebig University Giessen
Heinrich-Buff-Ring 17, 35392 Giessen, Germany
E-mail: juergen.janek@phys.chemie.uni-giessen.de

Dr. M. Weiss, Dr. R. Ruess, P. Minnmann, Prof. J. Janek
Center for Materials Research (LaMa)
Justus Liebig University Giessen
Heinrich-Buff-Ring 16, 35392 Giessen, Germany

Dr. J. Kasnatscheew, L. Stolz, Prof. M. Winter
Helmholtz-Institute Münster
IEK-12
Forschungszentrum Jülich GmbH
Correnstraße 46, 48149 Münster, Germany

 The ORCID identification number(s) for the author(s) of this article can be found under <https://doi.org/10.1002/aenm.202101126>.

© 2021 The Authors. Advanced Energy Materials published by Wiley-VCH GmbH. This is an open access article under the terms of the Creative Commons Attribution-NonCommercial-NoDerivs License, which permits use and distribution in any medium, provided the original work is properly cited, the use is non-commercial and no modifications or adaptations are made.

DOI: 10.1002/aenm.202101126

Y. Levartovsky, Prof. D. Aurbach
Department of Chemistry and BINA
BIU Institute of Nanotechnology and Advanced Materials
Bar-Ilan University
Ramat-Gan 5290002, Israel

N. R. Levy, Prof. Y. Ein-Eli
Department of Materials Science and Engineering
Technion – Israel Institute of Technology
Haifa 3200003, Israel
E-mail: eineli@technion.ac.il

Dr. T. Waldmann, Dr. M. Wohlfahrt-Mehrens
ZSW – Zentrum für Sonnenenergie- und Wasserstoff-Forschung
Baden-Württemberg
Helmholtzstrasse 8, 89081 Ulm, Germany

Prof. M. Winter
MEET Battery Research Center
Institute of Physical Chemistry
University of Münster
Correnstraße 46, 48149 Münster, Germany

Prof. Y. Ein-Eli
Grand Technion Energy Program (GTEP)
Technion – Israel Institute of Technology
Haifa 3200003, Israel

1.2. An Overview

More energy in shorter time at lower cost and increased safety—battery research has always been striving for improvement. Significant progress has been made in the field of lithium-ion batteries (LIBs) since their commercialization in 1991.^[1,2] LIBs store more energy, meaning their specific energy could be significantly increased by alternative cathode materials, reaching, for example, 421 W h kg⁻¹ using LiNi_xCo_yMn_{1-x-y}O₂ (NCM) compared to 279 W h kg⁻¹ of the original LiCoO₂ (LCO).^[3] Additionally, the use of solid-state batteries (SSBs) exclusively consisting of solid components may enable the application of lithium metal anodes (LMAs), which can offer higher energy density compared to batteries with graphite anodes.^[4] Furthermore, SSBs may also improve the mechanical stability of the cell,^[5] making it safer—especially when using flexible polymer electrolytes (PEs). However, a major challenge for widespread adoption of electric vehicles is the charging speed of the batteries used, that is, LIBs take too long to refill compared to traditional combustion engine powered vehicles. Based on that experience of refueling (500–800) km of range at a gas station in just five minutes, customers expect similar practice from electric vehicles.^[6] Therefore, charging to 80% state of charge (SOC) within 15 min is targeted by the US Advanced Battery Consortium (USABC).^[7] In this review, we analyze how this target transforms into requirements for materials and components on the cell level.

To achieve fast-charging capabilities, the power density P_V of utilized battery cells has to be increased, which comes at the cost of reduced energy density W_V . Therefore, there are always trade-offs between wide range and fast charging. Kinetic models of battery cells show that overpotentials exist in every part of the battery cell. From transport of lithium ions and electrons in the electrodes, charge transfer across phase boundaries to transport through the electrolyte, polarization effects limiting the charging rate lead to Li metal plating, limited utilization of active material, and temperature increase.^[8] Current-state high-voltage DC chargers can deliver peak powers of up to 350 kW.^[9,10] The Porsche Taycan with 93.4 kW h battery allows a maximum charging power of 270 kW, while the average during charging is 187 kW.^[9–11] Thus, recharging from 5% to 80% SOC takes 23 min. For comparison, the Tesla Model 3 with 75 kW h battery is recharged to 80% SOC in 27 min using Tesla's own Supercharger delivering a peak power of 250 kW in its third generation. Thus, the average charging power is about 130 kW, with the maximum value only reached for five minutes during the initial 20%.^[12] Of course, bigger battery packs will charge longer at given charging power. Thus, the charger has to be improved as well for long-range vehicles with big battery packs.^[13]

These state-of-the-art parameters are still significantly below what is required to reach the USABC goal for extreme fast charging (XFC): recharging within 15 min.^[7] In the following, we take a closer look at the materials applied to reach these values in order to identify the rate-limiting steps. Considering the example of Tesla, LiNi_xCo_yAl_{1-x-y}O₂ (NCA) cathodes are used^[14] in combination with graphite anodes. We assume a 100 kW h battery pack providing 500 km of driving range. With a volume of 400 L at system level and

200 L at cell level, this pack reaches an energy density W_V of 500 W h L⁻¹ at cell level. Using the average voltage of 3.7 V, the charge density Q_V is thus 135 A h L⁻¹. If we assume an electrode thickness of 200 μm (neglecting current collectors and separator), the resulting Q_A arises as 2.7 mA h cm⁻², thus approximately 3 mA h cm⁻². The required current density for charging is therefore 3 mA cm⁻² at 1C or 12 mA cm⁻² (4C), which would be needed to reach the XFC goal of 15 min charging time.

In view of research on fast charging, a few key steps have been identified as rate-limiting: a) diffusion of lithium ions within the anode active material, b) diffusion of lithium ions in the cathode active material (CAM), c) lithium-ion transport in the electrolyte phase (liquid or solid), and d) charge-transfer kinetics at the phase boundaries. In this case, we define charge transfer as the whole process of transport between electrolyte and electrode, thus it includes desolvation in the case of liquid electrolytes, the actual charge transfer across the electrolyte–electrode interface, and—for the presence of an interphase—also the ion transport through this interphase, which goes along with two charge-transfer processes across the electrolyte–interphase and the interphase–electrode boundary, respectively. The influence of lithium-ion transport in the electrolyte is rather small within the separator, but inside the porous electrodes it plays a major role in the fast-charging ability of a given battery cell.

From the materials perspective, lithium plating at the graphite anode and lithium diffusion in the CAM are primarily rate-limiting. Essentially, slow diffusion of lithium in the liquid electrolyte and the active materials causes the true rate-limiting steps. Morphology, shape, and orientation of active material particles can improve the limiting influence of lithium diffusion in the solid-state, which explains, for example, the recent trend to single crystalline CAM.^[15] On the electrode level, the active particle size distribution, tortuosity, and porosity are relevant, since diffusion-based lithium transport on the electrode scale is strongly influenced by those parameters in anodes and—to less extent—in cathodes.^[16–22] For the latter, lithium-ion mobility greatly depends on the SOC,^[22–26] since the crystal structure and the sequence of diffusion jumps typically change with the lithium content. Though, a high ionic conductivity on the material level does not necessarily translate to a fast-chargeable electrode if the tortuosity is high, for example. Going further on the size scale to the cell level, the relevance of engineering aspects—thermal management and the applied charging protocol, for example—takes precedence over physicochemical properties of the materials involved. Thus, this will only be discussed briefly in this review.

The physicochemical basics of LIBs with focus on kinetics will be summarized in Section 2. The origin of different overpotentials is discussed by means of electrochemical potential profiles. Thereby, the role of a small active particle size is noted, which allows for full utilization of the active material. Furthermore, differences between non-phase-transformation and phase-transformation electrodes (along with conversion-type ones as a special case thereof) will be highlighted, concluding that the evaluation of diffusion phenomena is challenging in the latter type and that conversion electrodes are much less suitable for fast-charging applications.^[27–29]

In addition to these electrode-related overpotentials, charge transfer at interfaces and interface degradation leading to interphase formation also have to be considered at both anode and cathode.^[30–34] For liquid electrolytes (LEs), concentration polarization is responsible as the decisive factor for electrolyte overpotentials, showing that the limiting current can be a major problem for thick electrodes in particular. Solid electrolytes (SEs) offer increased charge-carrier concentrations and a lithium-ion transference number near unity, thus concentration polarization does not occur.^[35] Hence, the rate is not affected by current limitation due to depletion of lithium ions in the electrodes, but rather by the generally limited (effective) ionic conductivity of SEs. Furthermore, SEs are suggested to enable the use of a lithium metal anode. As a consequence, lithium plating would not be fatal anymore but rather desired, in the case that dendrite growth can effectively be suppressed.

Subsequently, these concepts will be translated to recent materials' applications in the following sections. For the anode (Section 3), studies showing the superior fast-charging performance of materials with low diffusion barriers are presented. The benefits of small particles are highlighted as well, but also the pitfalls of increased degradation because of higher surface area. We present an overview of different anode materials and discuss their advantages and disadvantages. Following with the cathode in Section 4, the SOC dependence of the cathode overpotential is established using experimental data of state-of-the-art NCM material. In addition, the dependence of rate performance on lithium diffusivity is highlighted, that is, faster charging is possible with increasing lithium diffusion coefficient, by comparing to other CAMs. Section 5 focuses on electrolytes, both on liquid and solid electrolytes. Experimental studies are presented, which show that ionic conductivity in the separator liquid electrolyte is not rate-determining. At the anode side, transport within the liquid electrolyte (in the porous electrode) becomes rate-limiting, however. At high current densities, reactions are confined at the anode parts close to the separator, leading to a severe local potential drop and lithium plating eventually. It will also be elaborated in Section 5 that charge transfer at the electrode interfaces may become critical. The mechanical properties of solid electrolytes are particularly critical, as contact loss and significant increase in charge-transfer resistance may result from missing plasticity. In any case, the electrode microstructure—together with the active particle morphology and microstructure—is crucial and needs to be tailored to allow for high current densities and fast charging. High temperatures can be applied to overcome this shortcoming, as shown using experimental studies. In fact, preheating the EV battery in cold climate either internally or by external means to allow for faster charging is common practice.^[7] However, an increased temperature for better kinetics is always accompanied by accelerated degradation and thus shorter lifetime. Therefore, we briefly discuss thermal management systems along with optimized charging protocols and other measures utilized on the cell level to enable fast-charging applications in Section 6.

By highlighting the rate-limiting aspects of different battery components on the material level and suggesting optimal properties required for fast-charging applications, we hope to stimulate further research on this crucial topic, which thus

might lead to better market adaptation of electric vehicles in the future. While certain aspects of anode and cathode materials are comparable, they are specific enough to justify the separation of their discussion.

2. Physicochemical Basics of Fast Charging

Fast charging of batteries requires high current densities that cause high overpotentials, which occur at the different components in the battery. If these overpotentials exceed certain limits, a physicochemical reaction takes place and the battery is likely to fail. The most prominent mechanism that leads to cell failure is lithium plating at the negative electrode,^[36,37,38] typically graphite. Degradation processes can also occur at the cathode, namely oxygen evolution at oxide cathode active materials such as NCM and other layered oxides.^[39]

The voltage of a battery cell V is given by the difference between the electrochemical potentials of electrons (Fermi levels) at the anode $\tilde{\mu}_e^c$ and cathode $\tilde{\mu}_e^a$, respectively, according to

$$V = -\frac{1}{F}(\tilde{\mu}_e^c - \tilde{\mu}_e^a) = V_{oc} + \Delta\varphi^c + \Delta\varphi^a \quad (1)$$

Hereby, F is Faraday's constant, $\tilde{\mu}_i$ is the electrochemical potential of species i (in this case either electrons or Li^+ ions), which in turn is the sum of the chemical potential of this species μ_i and its electrical potential $z_i F\phi$ with the charge number z_i , given by

$$\tilde{\mu}_i = \mu_i + z_i F\phi \quad (2)$$

During battery operation, lithium ions are transported within the cell and, therefore, $\tilde{\mu}_{\text{Li}^+}$ is lifted from its equilibrium value as schematically shown in **Figure 1**.^[40] Such transport needs to be driven by an overpotential, which is induced in the cell via a lifted $\tilde{\mu}_e^c$ or $\tilde{\mu}_e^a$ at the cathode or anode contacts, respectively. The total overpotential at each electrode in the battery $\Delta\varphi^c$ or $\Delta\varphi^a$ can be considered as the sum of the overpotentials needed to drive the solid-state diffusion inside the respective active cathode or anode material ($\Delta\varphi_{\text{AM}}^c$ or $\Delta\varphi_{\text{AM}}^a$), the overpotential to drive the charge transfer between electrode and electrolyte ($\Delta\varphi_{\text{CT}}^c$ or $\Delta\varphi_{\text{CT}}^a$), and the overpotential to drive ionic transport in the electrolyte phase ($\Delta\varphi_{\text{EL}}^c$ or $\Delta\varphi_{\text{EL}}^a$) within a porous electrode:

$$\Delta\varphi^c = \Delta\varphi_{\text{AM}}^c + \Delta\varphi_{\text{CT}}^c + \Delta\varphi_{\text{EL}}^c \quad (3)$$

$$\Delta\varphi^a = \Delta\varphi_{\text{AM}}^a + \Delta\varphi_{\text{CT}}^a + \Delta\varphi_{\text{EL}}^a \quad (4)$$

In the active materials, the electronic conductivities are mostly significantly higher than the ionic conductivities.^[41] Therefore, any overpotentials $\Delta\varphi_{\text{AM}}^c$ or $\Delta\varphi_{\text{AM}}^a$ are caused primarily by ionic transport. This leads to a gradient of μ_{Li^+} inside the active material because of the solid-state diffusion that is driven by an applied voltage during charging or by the cell voltage during discharging. Solid-state diffusion is further elaborated in Section 2.1.1.

At the interfaces between the electrodes and the electrolyte, charge transfer takes place, which also requires some driving

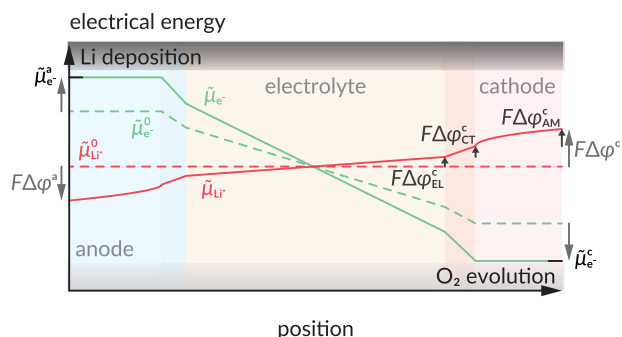


Figure 1. Schematic representation of the electrochemical potential profiles of electrons $\tilde{\mu}_e$ and lithium ions $\tilde{\mu}_{\text{Li}^+}$ in a battery cell during charging (solid lines) and in equilibrium (dashed lines). A higher electrochemical potential of electrons at the anode $\tilde{\mu}_e^a$ or lower at the cathode $\tilde{\mu}_e^c$ (relative to the OCV case) needs to be applied to drive the transport of lithium ions through the cell with the corresponding overpotentials $\Delta\phi^a$ and $\Delta\phi^c$, respectively. The overpotentials themselves drop at the different components in the battery, namely the electrolyte ($\Delta\phi_{\text{EL}}^c$ and $\Delta\phi_{\text{EL}}^a$), the interface between electrolyte and electrode ($\Delta\phi_{\text{CT}}^c$ and $\Delta\phi_{\text{CT}}^a$), and inside the electrode active material ($\Delta\phi_{\text{AM}}^c$ and $\Delta\phi_{\text{AM}}^a$).

force $\Delta\phi_{\text{CT}}$ that further alleviates $\tilde{\mu}_e$.^[40] As most CAMs in LIBs are high-voltage materials that exceed the stability window of typical electrolytes, side-reactions at the interface will occur that lead to the formation of a solid electrolyte interphase (SEI, or CEI for “cathode–electrolyte interphase”).^[30–33] Therefore, the charge transfer between active materials and electrolyte can involve several intermediate steps and may lead to significant overpotentials.^[30–33,40] The charge transfer is discussed in Section 2.1.2.

Also the transport of ions in the electrolyte needs to be driven by an overpotential $\Delta\phi_{\text{EL}}$ and adds up to the total overvoltage.^[40] Here, we have to distinguish typical liquid electrolytes with comparably low ion concentrations and transference number ($t_{\text{Li}^+} < 1$) and solid electrolytes with high ion concentrations and $t_{\text{Li}^+} \cong 1$.^[40] Transport in the electrolyte occurs via both diffusion (driven by $\nabla\mu_{\text{Li}^+}$) and migration (driven by $\nabla\phi$). Thereby, migration in liquid electrolytes is typically neglected whereas transport in the solid electrolyte is exclusively caused by migration.^[40,42] These mechanisms are further discussed in Sections 2.2.1 and 2.2.2, respectively.

2.1. Electrode Overpotentials

2.1.1. Solid-State Diffusion

Single-Phase Intercalation Electrodes: The overpotential that is required to drive the solid-state diffusion in an intercalation-type electrode is determined by the gradient of the chemical potential of the ions ($z_{\text{Li}^+} = 1$)

$$\Delta\phi_{\text{AM}}^c = -\frac{1}{F} [\mu_{\text{Li}^+}(x=L) - \mu_{\text{Li}^+}(x=0)] \quad (5)$$

under the assumption that electronic conductivity is significantly higher than ionic conductivity inside the electrode. Under this condition, the chemical diffusion coefficient \tilde{D}_{Li} of the neutral component lithium (Li^0) is only controlled by the

mobility of the lithium ions, and we use the symbol \tilde{D}_{Li^+} to denote this. Formally, however, in every electrochemical experiment \tilde{D}_{Li} is evaluated. The effect of mixed electronic and ionic conduction on the electrode polarization is discussed in detail by Usiskin and Meier.^[43] For simplicity, we consider here the overpotential at the cathode, and the analogue anode case is added below. In Equation (5), $\Delta\phi_{\text{AM}}$ is described by the difference between μ_{Li^+} at the surface of the active material ($x=L$) and at the center of the active material particle ($x=0$) in the case of spherical particle type (radius L) electrode materials.

Nernst’s equation connects the chemical potentials with the respective activities of Li^+ ions (a_{Li^+}) according to

$$\Delta\phi_{\text{AM}}^c = -\frac{RT}{F} [\ln(a_{\text{Li}^+}(L)) - \ln(a_{\text{Li}^+}(0))] = -\frac{RT}{F} \Delta \ln(a_{\text{Li}^+}) \quad (6)$$

Hereby, R is the gas constant, T the temperature, and F Faraday’s constant. If now only a small concentration gradient Δc_{Li^+} as compared to the total concentration of Li^+ ions in the electrode c_{Li^+} is established, Equation (6) can be written as^[44]

$$\Delta\phi_{\text{AM}}^c = -\frac{RT}{F} \left(\frac{\partial \ln(a_{\text{Li}^+})}{\partial \ln(c_{\text{Li}^+})} \right) \Delta \ln(c_{\text{Li}^+}) = -\frac{RT}{F} W \frac{\Delta c_{\text{Li}^+}}{c_{\text{Li}^+}} \quad (7)$$

Equation (7) links the overpotential with the gradient of Li^+ ions inside the electrode via the thermodynamic enhancement factor $W = \frac{\partial \ln(a_{\text{Li}^+})}{\partial \ln(c_{\text{Li}^+})}$.^[44] W can be determined from coulometric

titration of an electrode under the assumption that the electrode is not undergoing any phase transformation during lithium intercalation.^[44] The anode overpotential results similarly as

$$\Delta\phi_{\text{AM}}^a = \frac{RT}{F} \left(\frac{\partial \ln(a_{\text{Li}^+})}{\partial \ln(c_{\text{Li}^+})} \right) \Delta \ln(c_{\text{Li}^+}) = \frac{RT}{F} W \frac{\Delta c_{\text{Li}^+}}{c_{\text{Li}^+}} \quad (8)$$

The concentration profile of Li^+ can be calculated via Fick’s second law

$$\frac{\partial c_{\text{Li}^+}}{\partial t} = \tilde{D}_{\text{Li}^+} \frac{\partial^2 c_{\text{Li}^+}}{\partial x^2} \quad (9)$$

with the solid-state chemical diffusion coefficient of Li^+ ions in the intercalation electrode \tilde{D}_{Li^+} . We note that Equation (9) can only be applied for small concentration gradients, that is, under the assumption of constant \tilde{D}_{Li^+} inside the active material. To solve the differential Equation (9), the following boundary conditions (Equations (10)–(12)) can be assumed, which represent the galvanostatic charging with current I from $t=0$ onward.^[45] The current induces a higher concentration of Li^+ ions at the electrode’s surface (initial concentration $c_{\text{Li}^+}^0$), which then leads to an expansion of the Nernstian diffusion layer over time throughout the volume of the electrode.

$$c_{\text{Li}^+} = c_{\text{Li}^+}^0 \quad 0 \leq x \leq L; \quad t = 0 \quad (10)$$

$$-\tilde{D}_{\text{Li}^+} \frac{\partial c_{\text{Li}^+}}{\partial x} = \frac{I}{AF} \quad x = L; \quad t > 0 \quad (11)$$

$$\frac{\partial c_{\text{Li}^+}}{\partial x} = 0 \quad x = 0; \quad t \geq 0 \quad (12)$$

With A being the surface area of the electrode, this leads to the solution^[45]

$$c_{\text{Li}^+} = c_{\text{Li}^+}^0 + \frac{It}{FAL} + \frac{IL}{FA\tilde{D}_{\text{Li}^+}} \left[\frac{3x^2 - L^2}{6L^2} - \frac{2}{\pi^2} \sum_{n=1}^{\infty} \frac{(-1)^n}{n^2} \exp\left(-\frac{n^2\pi^2\tilde{D}_{\text{Li}^+}}{L^2}t\right) \cos\left(\frac{n\pi x}{L}\right) \right] \quad (13)$$

We note that Equation (12) generally only applies for a flat plate; for other geometries, such as cylinders or spheres, geometry-related constants have to be included,^[43] but the differences in the equations are only minor, which implies that the flat plate geometry describes the system sufficiently well. The concentration polarization can now be calculated as the difference in concentrations between the surface ($x = L$) and the center of the spherical particle ($x = 0$) as

$$\Delta c_{\text{Li}^+} = c_{\text{Li}^+}(x=L) - c_{\text{Li}^+}(x=0) = \frac{IL}{FA\tilde{D}_{\text{Li}^+}} \left[\frac{1}{2} - \frac{4}{\pi^2} \sum_{n=1}^{\infty} \frac{1}{(2n-1)^2} \exp\left(-\frac{(2n-1)^2\pi^2\tilde{D}_{\text{Li}^+}}{L^2}t\right) \right] \quad (14)$$

We note that although the concentration polarization would describe the solid-state diffusion overpotential as defined in Equation (13), the practical overpotential can be considered as the difference of electrode potential from the equilibrium open-circuit potential. Therefore, from an application point-of-view, the overpotential is given by the difference in concentration at the surface of the electrode and the equilibrated concentration

$$\Delta c_{\text{Li}^+}^{\text{eq}} = c_{\text{Li}^+}(x=L) - \frac{It}{FAL} = \frac{IL}{FA\tilde{D}_{\text{Li}^+}} \left[\frac{1}{3} - \frac{2}{\pi^2} \sum_{n=1}^{\infty} \frac{1}{n^2} \exp\left(-\frac{n^2\pi^2\tilde{D}_{\text{Li}^+}}{L^2}t\right) \right] \quad (15)$$

Equation (15) can now be inserted into Equation (7) to obtain the overpotential. Under the assumption of either short ($t_{\text{charge}} \ll \frac{L^2}{\tilde{D}_{\text{Li}^+}}$) or long ($t_{\text{charge}} \gg \frac{L^2}{\tilde{D}_{\text{Li}^+}}$) charging times t_{charge} , Equations (16) and (17) are obtained.^[46]

$$\Delta\varphi_{\text{AM}} = \frac{2}{\sqrt{\pi}} \frac{IWRt}{F^2Ac_{\text{Li}^+}\sqrt{\tilde{D}_{\text{Li}^+}}} \sqrt{t} \quad (16)$$

$$\Delta\varphi_{\text{AM}} = \frac{1}{3} \frac{IWRtL}{F^2Ac_{\text{Li}^+}\tilde{D}_{\text{Li}^+}} \quad (17)$$

In **Figure 2a,b** it is schematically shown how the concentration profiles in the material develop during delithiation. We use a nickel-rich NCM as example since it is a typical single-phase material at high concentration of intercalated

Li^+ ions (steps I–III). In step I, the concentration gradient did not yet fully progress throughout the material (semi-infinite diffusion) and the overpotential follows Equation (16). After charging for longer time, the concentration gradient will eventually reach the center of the active material particles (step II) and diffusion will be finite from this point on (step III). The overpotential is given by Equation (17) in this case. Upon relaxation, the concentration and the chemical potential equilibrate again (Figure 2c,d). The practical overpotential can then be visualized as in Figure 2d.

We emphasize that, even if fast charging of electrodes is desired, the electrodes should be designed to fully utilize the volume of active materials. Namely, the particle size should fulfil the relation^[47]

$$L < \sqrt{t_{\text{charge}}\tilde{D}_{\text{Li}^+}} \quad (18)$$

Therefore, Equation (17) would give a good measure of the overpotential from solid-state diffusion for realistic electrodes. To achieve this condition (Equation (18)), sufficiently small active materials should be employed whereas the maximum reasonable size should be correlated with \tilde{D}_{Li^+} . We note that it needs to be considered that \tilde{D}_{Li^+} is not a constant value for every material but is a function of temperature, lithium concentration, and lithium vacancy concentration.^[41,48,49]

To understand these dependencies, we have to take a look at the mechanism of ion transport in solids. The crystal structure creates a periodic potential profile with its minima being crystallographic sites for the transported species.^[50] Ion transport occurs when an ion moves from an occupied lattice site to a neighboring empty lattice site. The free energy barrier of migration ΔG_{m} that has to be overcome depends on the difference between initial state and the transition state of the jump. Thereby, the probability of a forward, that is, successful, jump is increased in the case of crystallographically equivalent initial and final states, which result in a symmetrical activation profile.^[51]

Here, the number of vacant sites n_{v} and that of normal sites N per unit volume gives the defect concentration per unit volume $[d]$ as^[52]

$$[d] = \frac{n_{\text{v}}}{N} \quad (19)$$

The self-diffusion coefficient of lithium ions D_{Li^+} can then be obtained from the jump frequency ν , the reciprocal number of jump directions α , and the jump distance a_0 by^[52,53]

$$D_{\text{Li}^+} = \alpha [d] a_0^2 \nu \quad (20)$$

If each jump were successful, ν would simply be equal to the vibrational frequency of the atoms ν_0 . Since this is not the case, ν is given as the product of ν_0 and the probability of a successful jump as

$$\nu = \nu_0 \exp\left(-\frac{\Delta G_{\text{m}}}{k_{\text{B}}T}\right) \quad (21)$$

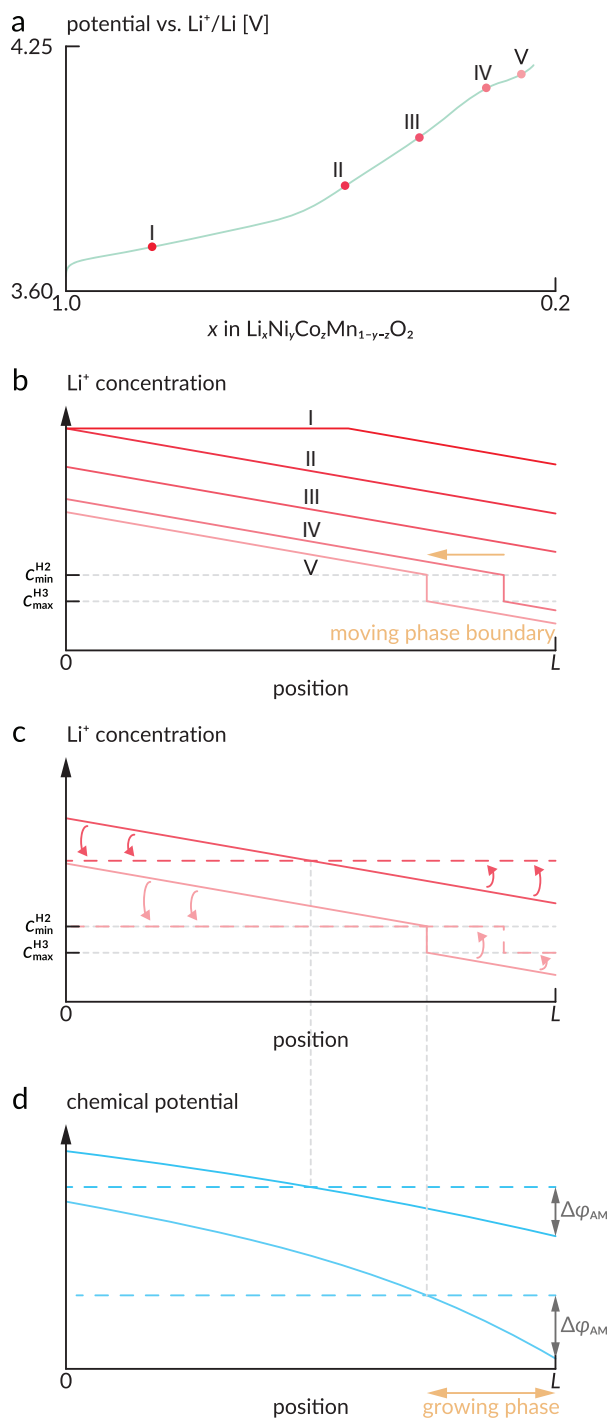


Figure 2. a) Exemplary charging profile of a nickel-rich NCM cathode. b) Simplified representation of the concentration gradients at the points I–V during charging of the NCM cathode in (a). For steps I–III, nickel-rich NCM behaves like a single-phase material, while for steps IV–V the H2 and H3 phases coexist with limited solubility of lithium ions c_{\min}^{H2} and c_{\max}^{H3} , respectively. c) Concentration profiles for steps III and V during charging (solid lines) and if the cell was in equilibrium (dashed line). A phase boundary in step V still exists in equilibrium. d) Chemical potential profiles for the cases shown in (c). The practical overpotential $\Delta\varphi_{\text{AM}}$ is given by the difference of the chemical potential during charging and the chemical potential in equilibrium. In the case of a two-phase coexistence, the overpotential is only determined by the phase, which is growing during charging.

using Boltzmann's constant k_B .^[52] Now, α can be replaced by a geometrical factor γ , which also accounts for different diffusion anisotropies.^[51,52] This leads to

$$D_{\text{Li}^+} = \gamma [d] a_0^2 v_0 \exp\left(-\frac{\Delta G_m}{k_B T}\right) \quad (22)$$

as general expression for D_{Li^+} .^[52] The free energy can be separated into the enthalpy of migration ΔH_m and the entropy of migration ΔS_m , which gives

$$D_{\text{Li}^+} = \gamma [d] a_0^2 v_0 \exp\left(\frac{\Delta S_m}{k_B}\right) \exp\left(-\frac{\Delta H_m}{k_B T}\right) \quad (23)$$

Now, the constants can be combined into a pre-exponential factor D_0 , which also contains the migration entropy, resulting in an Arrhenius-type form

$$D_{\text{Li}^+} = [d] D_0 \exp\left(-\frac{\Delta H_m}{k_B T}\right) \quad (24)$$

for the self-diffusion coefficient, where ΔH_m is the activation energy of the transport process.^[51] We note that D_{Li^+} is linked to \bar{D}_{Li^+} via the Li^+ concentration dependent enhancement factor W (as defined above) by^[44]

$$\bar{D}_{\text{Li}^+} = W D_{\text{Li}^+} \quad (25)$$

However, for an assessment of the fast-charging capability of electrodes, the concentration dependence only plays a minor role. Therefore, the overpotential needed to drive the solid-state diffusion in the active materials (Equation (17)) and its dependence on key parameters (active electrode area A and particle radius L) can be simplified as

$$\Delta\varphi_{\text{AM}} \sim I \cdot \frac{L}{A \cdot \bar{D}_{\text{Li}^+}} \quad (26)$$

We find that the overpotential is proportional to the particle size, the reciprocal surface area, and the reciprocal (chemical) lithium-ion diffusion coefficient of the electrode material at a given temperature of cell operation.

Phase-Transformation and Conversion-Type Electrodes: Other than in the previous section, phase-transformation electrodes do not necessarily exhibit a uniform concentration gradient throughout the full active material volume, but rather show distinctly separated phase boundaries within the material (moving boundary model). Upon lithiation or delithiation, the phase boundaries are considered to move.^[54,55] Therefore, as the activities of Li^+ ions a_{Li^+} within each phase stay constant during the phase-transformation reaction, the equilibrium potentials also remain constant and a plateau in the charge/discharge curves is observed for phase-transformation electrodes. As a result, a unique relation between c_{Li^+} and $\Delta\varphi_{\text{AM}}$ does not exist in this case. However, within each phase a concentration gradient of lithium may be present that obeys the

same equations as for non-phase-transformation materials (Equations (16) and (17)).^[54–56]

The concentration and potential in phase-transformation materials can again be visualized in the example in Figure 2, because nickel-rich NCM also has two coexisting phases at low concentrations of intercalated Li⁺ ions (steps IV and V). As depicted in Figure 2a, the electrode potential reaches a plateau at these steps, where the H2 and H3 phases coexist in parallel.^[57] The concentration of intercalated Li⁺ ions is different in both phases and further delithiation leads to a progression of the phase boundary. If the potential is relaxed, the concentration and chemical potential will equilibrate according to Figure 2c,d. As can be seen, only the phase that grows upon delithiation determines the overpotential. Therefore, it is hardly quantitatively accessible as the position of the phase boundary needs to be known.^[56] However, Equation (17) can still be used for estimation as it represents an upper limit for the overpotential also in the case of phase-transformation electrodes.

It is important to note that the overpotential as defined in Equation (1) requires knowledge of the open-circuit potential, which is well defined by the lithium concentration in the material for non-phase-transformation electrodes. For phase-transformation electrodes, however, there is a well-known hysteresis between the open-circuit potentials at charge and discharge.^[28,58] As a result, determination of *W* from coulometric titration can be intricate for phase-transformation electrodes. Therefore, the assessment and quantification of diffusion-related processes in such materials is challenging. The hysteresis is discussed to originate from residual strain from the phase transformation within the material that needs to be accommodated, leading to an offset of the open-circuit potential by the strain-accommodation energy.^[59] Another explanation is given by the coexistence of different phase fractions in individual particles in the electrode and, thus, the coexistence of various equilibria in the electrode.^[58]

Conversion-type electrodes can be considered as a special case of phase-transformation electrodes. However, the structural difference between lithiated and delithiated phases is much more substantial. Thus, besides a mostly very sluggish lithium transport within the material, the strain that has to be accommodated and the resulting hysteresis in open-circuit potential is huge.^[27–29] Both of these effects make this kind of electrodes still quite unattractive for fast-charging batteries, however, interesting approaches employing nanomaterials have early been reported, including impressively fast cycling kinetics.^[60]

2.1.2. Charge Transfer at Interfaces

The overpotential $\Delta\phi_{CT}$ to drive the charge transfer of lithium at the interface between electrode and electrolyte is governed by many factors. Again, we use $\Delta\phi_{CT}$ as a simplified expression for the overpotential at an electrode and it has to be noted that both the anode and cathode contribute individual overpotentials $\Delta\phi_{CT}^a$ and $\Delta\phi_{CT}^c$, respectively. In the simplest case, the electrode material is in direct contact with the electrolyte and no additional interfacial layers impede the charge transfer. Further,

it is assumed that the lithium-ion transfer determines the overpotential and that electrons are readily available. In this case, the overpotential is related to the interfacial current *I* via the Butler–Volmer equation^[61,62]

$$I = j_0 A \left[\exp\left(\frac{\alpha F}{RT} \Delta\phi_{CT}\right) - \exp\left(-\frac{(1-\alpha)F}{RT} \Delta\phi_{CT}\right) \right] \quad (27)$$

Hereby, j_0 is the exchange current density and α is the charge-transfer coefficient that describes the potential landscape at the interface. j_0 is a function of the lithium-ion concentration in the electrolyte $c_{Li^+}^{EL}$ and the concentrations of lithium ions, lithium vacancies, and electrons in the electrode c_{Li^+} , $c_{V_{Li}}$, c_{e^-} , as well as the rate constants and activation energies for lithium insertion and extraction k_{in} , k_{ex} , E_{in} , E_{ex} , respectively, and can be expressed as^[61]

$$j_0 = F \exp\left(-\frac{\alpha E_{ex}}{RT}\right) \exp\left(-\frac{(1-\alpha)E_{in}}{RT}\right) [k_{ex} c_{Li^+}]^\alpha [k_{in} c_{Li^+} c_{V_{Li}} c_{e^-}]^{1-\alpha} \quad (28)$$

Under the assumption that the energy barrier for lithium insertion and extraction is equivalent ($E_{in} = E_{ex} = E_A$),

$$j_0 = j'_0 \exp\left(-\frac{E_A}{RT}\right) \quad (29)$$

can be obtained as simplified expression for the exchange current density. Here, j'_0 is a prefactor that contains the rate constants and is dependent on the concentrations of lithium ions, vacancies, and electrons in the active material and the electrolyte. The charge-transfer resistance R_{CT} is given by^[63]

$$R_{CT} = \frac{RT}{zFAj_0} \quad (30)$$

and can thus be rewritten using Equation (29) as

$$\frac{1}{R_{CT}} = \frac{zFAj'_0}{RT} \exp\left(-\frac{E_A}{RT}\right) \quad (31)$$

revealing its temperature dependence. Linearization of Equation (27) under the assumption of small $\Delta\phi_{CT}$ yields

$$\Delta\phi_{CT} \sim I \cdot \frac{1}{Aj_0} \quad (32)$$

which presents the overpotential as a function of the electrode surface area and the exchange current density of the interface between electrode and electrolyte at a given temperature. However, as most electrode materials operate at potentials, where the electrolyte components are unstable, often an SEI layer forms at the interface between electrode and electrolyte that impedes the charge transfer between them. Additionally, artificial interfacial layers, that is, coatings, are commonly used on certain electrode materials to gain better control of such interfacial processes.^[64] These interfacial layers can manipulate the

charge-transfer kinetics drastically and determine the energy landscape as well as the charge-transfer coefficients,^[65] as will be shown in Section SEI and Artificial SEI.

In the case of phase-transformation or conversion-type electrodes, charge transfer followed by insertion or removal of Li⁺ ions from the electrode host structure initiates a phase transformation of the material. To initiate this phase transformation, a certain driving force is required, which can take very substantial values.^[28] The required overpotential to drive the phase-transformation or conversion reaction depends on the individual reaction pathway of the electrode material.^[28] It is possible to catalyze the phase transformation, for example, by using certain electrolyte additives that take part in the reaction.^[66]

2.2. Electrolyte Overpotentials

2.2.1. Concentration Polarization in Liquid Electrolytes

Application of a potential difference between the electrodes initiates an ionic current in the electrolyte. Despite ionic currents in electrolytes are caused by migration (field-driven) and diffusion (concentration gradient driven), diffusion is considered as eventually limiting cell performance at high rates.^[42] Therefore, we will focus on diffusion in the liquid electrolyte in the following.

Inside a porous electrode, the ionic flux is progressively consumed by the active materials, which can even lead to the depletion of ions deeper inside the electrode (close to the current collector). When using a 1D-description of Fick's law, the differential equation needs to be modified by a term that accounts for the consumption of ionic flux^[47]

$$\frac{\partial c_{\text{Li}^+}^{\text{EL}}}{\partial t} = \tilde{D}_{\text{Li}^+}^{\text{EL}} \frac{\partial^2 c_{\text{Li}^+}^{\text{EL}}}{\partial x^2} + \frac{I}{FA d} (1 - t_{\text{Li}^+}) \quad (33)$$

with $c_{\text{Li}^+}^{\text{EL}}$ being the concentration of Li⁺ ions in the electrolyte phase, d the thickness of the electrode, and $\tilde{D}_{\text{Li}^+}^{\text{EL}}$ the chemical diffusion coefficient of Li⁺ ions in the electrolyte. x is the spatial coordinate in the electrolyte with $x = 0$ being the tip of the electrode (at the separator) and $x = d$ being the bottom of the electrode (at the current collecting foil). Equation (33) can be solved using the boundary conditions in Equations (34)–(36) with $c_{\text{Li}^+}^{\text{EL},0}$ being the concentration of lithium ions in equilibrium.

$$\frac{\partial c_{\text{Li}^+}^{\text{EL}}}{\partial x} = -\frac{I}{FA} (1 - t_{\text{Li}^+}) \quad x = 0; \quad t \geq 0 \quad (34)$$

$$\frac{\partial c_{\text{Li}^+}^{\text{EL}}}{\partial x} = 0 \quad x = d; \quad t \geq 0 \quad (35)$$

$$c_{\text{Li}^+}^{\text{EL}} = c_{\text{Li}^+}^{\text{EL},0} \quad t = 0 \quad (36)$$

Solution of Equation (33) under the given boundary conditions yields the concentration profile of lithium ions in the electrolyte phase inside the composite electrode as^[47]

$$c_{\text{Li}^+}^{\text{EL}} = c_{\text{Li}^+}^{\text{EL},0} \left(1 - \alpha \frac{I}{FA} \right) - \frac{I}{FA d} \frac{1 - t_{\text{Li}^+}}{2\tilde{D}_{\text{Li}^+}^{\text{EL}}} (x^2 - 2L_{\text{EL}}x - 2dx) \quad (37)$$

Hereby, α is a parameter (unit m⁻¹) that depends on the electrode geometry as detailed by Newman et al.^[47] When the concentration is fully depleted at one of the battery electrodes, the limiting current density is reached, which is derived based on Equation (37) as follows.^[47] The limiting current is likely to differ between anode and cathode, $j_{\text{lim}}^{\text{a}}$ and $j_{\text{lim}}^{\text{c}}$ respectively, but for simplicity the limiting current density is only expressed as

$$j_{\text{lim}} = \frac{F \tilde{D}_{\text{Li}^+}^{\text{EL}} c_{\text{Li}^+}^{\text{EL},0}}{(1 - t_{\text{Li}^+}) L_{\text{EL}} \beta} \quad (38)$$

in the following. Thereby, L_{EL} is the thickness of the separator and β is a parameter that describes the electrode geometry.^[47] β accounts for the porosity and thickness of the electrode and will effectively lead to a reduced j_{lim} in the case that lithium transport pathways are tortuous. The most ideal electrode is a flat plate, for which β equals 0.5.^[47] Far higher values of β are reached in practical battery electrodes. For the assessment of the overpotential needed to drive the diffusion of lithium in the electrolyte phase, an alternate form of Nernst's equation can be used^[63]

$$\mu_{\text{Li}^+} = \mu_{\text{Li}^+}^0 + \frac{RT}{F} \ln \left(1 - \frac{j}{j_{\text{lim}}} \right) \quad (39)$$

The total overpotential to drive the diffusion of Li⁺ ions in the electrolyte would be the difference in the chemical potentials in the electrolyte between the anode and cathode surfaces. The individual overpotential at each electrode takes the following form. Again, for simplicity we avoid using anode- and cathode-specific indices ($\Delta\varphi_{\text{EL}}^{\text{a}}$ and $\Delta\varphi_{\text{EL}}^{\text{c}}$) and use

$$\Delta\varphi_{\text{EL}} = \mu_{\text{Li}^+} - \mu_{\text{Li}^+}^0 = \frac{RT}{F} \ln \left(1 - \frac{I}{j_{\text{lim}} A_{\text{O}}} \right) \quad (40)$$

as generalized expression instead. Hereby, A_{O} describes the cross-sectional cell area. Different limiting currents j_{lim} at each electrode can be expected because the transport in the electrolyte phase of porous electrodes strongly depends on the microstructure resulting in different ionic tortuosities.^[19] As can be seen in Equation (40), the overpotential increases drastically once the current approaches the limiting current. In the case $\frac{I}{A_{\text{O}}} \ll j_{\text{lim}}$, Equation (40) can be linearized resulting in

$$\Delta\varphi_{\text{EL}} \sim I \frac{T}{A_{\text{O}} \cdot j_{\text{lim}}} \quad (41)$$

thus showing an ohmic relation between current and overpotential for comparably small currents. We note that according to Equation (39), j_{lim} determines the temperature dependence of $\Delta\varphi_{\text{EL}}$ as $\tilde{D}_{\text{Li}^+}^{\text{EL}}$ typically shows an Arrhenius-type behavior.^[67] The limiting current caused by concentration polarization can become an issue especially in thick electrodes with high mass loading.^[19,42,68] Although the overpotentials to drive charge transfer and solid-state diffusion may be sufficiently low in such a case due to high interfacial areas A between electrode

and electrolyte, the overpotential to drive diffusion in the electrolyte does depend on the cross-sectional area A_{\varnothing} of the cell and may actually limit the cell performance in some cases.^[19,42] The limiting current densities can be lifted by optimizing ionic diffusion pathways in the porous electrodes, by increasing temperature, or using solvents with low viscosity and high Li^+ ion diffusion coefficients.^[19,69]

2.2.2. Migration in Solid Electrolytes

Other than in liquid electrolytes, in (inorganic) solid electrolytes the transference number of Li^+ ions can be considered as 1 and the concentration of Li^+ is substantially higher, thus, the electric field between the electrodes alone drives the ionic current.^[35] Therefore, the relation between ionic current and overpotential is simply ohmic according to

$$\Delta\varphi_{\text{EL}} = I \frac{L_{\text{EL}}}{A_{\varnothing}} \frac{1}{\sigma_{\text{SE}}} \quad (42)$$

with the ionic conductivity σ_{SE} , and there is no concentration polarization that will eventually lead to current limitations.^[35] However, the (effective) conductivities of typical solid electrolytes are comparably low^[70] and the associated overpotentials to the ionic transport can still be substantial, especially because of the tortuous conduction pathways inside composite electrodes.^[71] If the overpotential to drive ionic conduction through a composite electrode is higher than the overpotential to drive the charge transfer and solid-state diffusion, the lithiation or delithiation of the electrode will occur inhomogeneously.^[47] The ionically easily accessible parts of the electrode, that is, close to the solid electrolyte separator, are lithiated or delithiated first and the parts that are more distant from the separator, that is, close to the current collector, remain inactive until the reaction in the easily accessed parts is completed.^[47] Thus, a reaction zone progresses through the composite electrode during lithiation or delithiation.^[47,72] In the case of low conductivities, Equation (42) would be replaced by

$$\Delta\varphi_{\text{EL}} = I \frac{L_{\text{sep}}}{A_{\varnothing}} \frac{1}{\sigma_{\text{SE}}} + I^2 t_{\text{charge}} \frac{1}{q\sigma_{\text{SE}}} \quad (43)$$

where the pathway length for ionic transport L_{EL} is split up into one part covering the transport in the separator L_{sep} and another part describing the transport in the composite electrode and the expansion of the reaction zone.^[47,72] Hereby, t_{charge} is the charging time of the cell and q is the capacity density of the respective composite electrode. This would mean that when the cutoff potential for charging is reached some parts of the electrode have not been accessed by the reaction zone and remain inactive. This is especially important in thick electrodes.^[72] Therefore, high ionic conductivity is an important factor to achieve full active material utilization at high charging rates.^[71,73] High temperatures can significantly accelerate the ionic transport and improve the conductivity, which is a benefit of solid electrolytes compared to liquid electrolytes, as they can be operated at comparably high temperatures.^[68]

3. Anode

3.1. Limiting Processes/Parameters on the Anode Side

Regarding anodes, fast charging is limited by processes on the material, electrode, and cell level (see **Figure 3**). The limitations on these three levels are discussed in the following sections. We focus mainly on graphite and carbon materials, $\text{Li}_4\text{Ti}_5\text{O}_{12}$ (LTO), and silicon as most important anode materials yet and briefly consider the lithium metal anode.

3.1.1. Limitation of Fast Charging on the Material Level

An important limiting factor for fast charging is the transfer of Li^+ ions into the anode active material in the form of intercalation, insertion, alloying, or deposition as metal. The most relevant processes in the case of intercalation, insertion, and alloying include the transfer of Li^+ ions into the active material and their solid-state diffusion inside the active material, driven by the local electric field and by concentration gradients, respectively. These processes are hindered by energetic barriers as discussed in the following sections, whereas lower barriers and higher probabilities of overcoming them increase the fast-charging capability. The formed SEI also plays an important role as it modifies the charge-transfer steps.

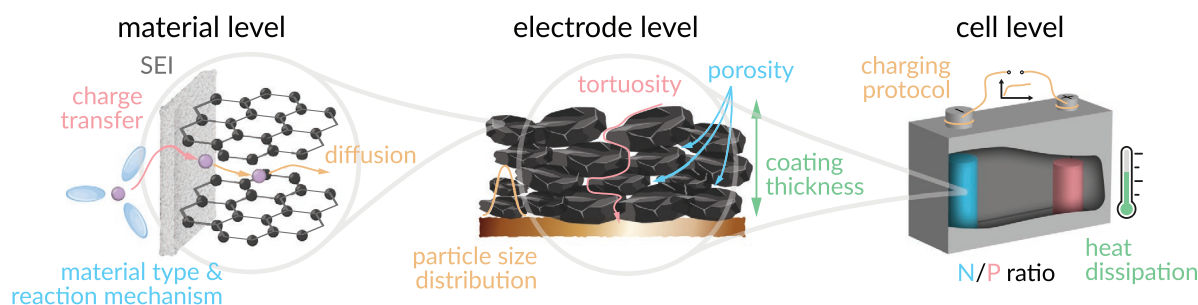


Figure 3. Overview of parameters relevant for fast-charging capability from material to cell level. On the material level, charge transfer from electrolyte to anode material, which depends on the type of material and the corresponding reaction mechanism, is relevant in addition to diffusivity within the material. The particle morphology, particle size distribution, tortuosity, porosity, and coating thickness all influence the fast-charging ability on the electrode level. Lastly, the ratio between the areal capacities of anode and cathode (N/P ratio), the charging protocol, and heat dissipation become relevant on the cell level.

Barriers for Migration of Li⁺ Ions from Electrolyte into Anode Active Materials: During fast charging, a high amount of Li⁺ ions per electrochemically active surface area and per time unit has to be transferred from the electrolyte into the active material particles. As detailed in Section 2.1.2, a charge-transfer barrier E_A is present, limiting this migration process. The charge-transfer barrier is related to an Li⁺ ion crossing the electrolyte|electrode interface including stripping-off the Li⁺ ion's solvation shell, transfer through the SEI layer, and acceptance of an electron provided by an external circuit from the cathode.^[34] This barrier is connected to the charge-transfer resistance^[34,74] and causes the charge-transfer overpotential $\Delta\phi_{CT}^a$, as shown in Equation (32). Due to its temperature dependence, the charge-transfer resistance is lower at higher temperatures (see Equation (31)).

For graphite, the activation barrier from the electrolyte into the active material is in the order of ≈ 0.6 eV as determined in most cases using LiClO₄ as conductive salt dissolved in dimethyl sulfoxide (DMSO), 1,2-dimethoxyethane (DME), ethylene carbonate (EC), dimethyl carbonate (DMC), EC:DMC, or EC:DEC (diethyl carbonate).^[75–77] Xu et al. obtained a quite close value of (0.54 ± 0.03) eV for intercalation into graphite for the more common LiPF₆ in EC:DMC.^[78] On the other hand, the energy barrier for the Li⁺ ion transfer into LTO was found to be only 0.33 eV (while using a similar calculation method). The difference was attributed to the absence of an SEI layer on the LTO surface.^[78] This lower barrier for LTO explains part of its improved fast-charging capability compared to graphite.

Yao et al. investigated the insertion barriers of Li⁺ ions through the graphene planes by density functional theory (DFT) calculations.^[79] The energy barrier for Li⁺ passing a C₆ ring of 10.2 eV is very high and therefore unlikely to be overcome.^[79] However, the barrier is decreased by different atomic defects, for example, the Stone–Wales defect, mono-vacancies, or di-vacancies reduce the energy barrier to 6.35, 8.86, and 2.36 eV, respectively.^[79] For LiC₆, dispersion-corrected DFT calculations also yielded high values in the order of 8 eV for Li⁺ moving through a C₆ ring.^[80] Therefore, intercalation proceeds for graphite mainly through the edge planes and not through the basal planes as shown in **Figure 4a**. However, irreversible capacity loss also happens mainly via these edge sites.^[81] Therefore, graphite materials with more edge sites and thus larger BET surface area usually show both a better fast-charging behavior and increased initial capacity losses.

A similar trend was observed for Li⁺ insertion into carbon nanotubes. The barrier for insertion into the nanotube through a wall (24.0 to 2.0 eV) is unfavorable compared to insertion through an open-end (≈ 0.3 eV) as shown in **Figure 4a**.^[82] This barrier decreases by one order of magnitude when the nanotube wall's ring size increases from a pentagon to an octagon.^[82] However, this barrier of 2.0 eV is still comparably high. Therefore, the pathway through the open end is favored.

Kaghazchi studied the intercalation barrier of Li⁺ via Si(100) and Si(111) surfaces by DFT calculations as a function of the surface density of adsorbed Li adatoms.^[83] The author obtained barriers in the range of (0.63–1.26) eV.^[83] The lowest barrier of 0.63 eV was found for intercalation of Li⁺ via the Si(100) surface, which was fully covered with Li adatoms.^[83] This value is similar to the range of diffusion barriers reported for Li atoms

in Si.^[84–88] For comparison, a significantly higher barrier of 0.97 eV was obtained for the Si(111) surface fully covered with Li adatoms; therefore it was concluded that the Li⁺ transfer proceeds most likely via the Si(100) surface, as depicted in **Figure 4a**.^[83]

The energetic barriers for Li⁺ transfer into Si nanowires were studied by DFT calculations as well. The diffusion barrier for Li⁺ on the surface of Si nanowires was reported to be in the range of (0.12–0.20) eV, which is low compared to the transfer from the surface to the inner of the wire (≈ 0.9 eV) (see **Figure 4b,c**).^[89]

By and large, charge transfer is often favored at specific crystallographic surfaces which—along with potential diffusion anisotropy within the bulk phase—is the basis for optimizing materials for fast charging by morphology control.

Solid-State Li⁺ Diffusion inside Active Materials: Once the Li⁺ ion is located inside an active material, the dominating limiting factor for fast charging is its solid-state diffusion inside the bulk phase, which highly influences the overpotential $\Delta\phi_{AM}^a$, as shown in Equations (16), (17).^[74–76] Next to lithium diffusion, electron transport mostly plays a less limiting, but not insignificant role for fast-charging applications. While it is not an issue for lithium metal and graphite with electronic conductivities of over 10^7 S cm⁻¹ and 10^4 S cm⁻¹,^[90,91] respectively, silicon ($<10^{-3}$ S cm⁻¹)^[92] and LTO ($<10^{-7}$ S cm⁻¹)^[93] suffer from low electronic conductivity, adversely affecting their fast-charging capability. Therefore, methods to increase the electronic conductivity by means of heat treatment or introduction of conductive agents, for instance, are actively investigated.^[92,94]

Li Diffusion in Lithium Metal: Diffusion within LMAs takes place via a monovacancy mechanism.^[95] With a self-diffusion coefficient of $(6–9) \times 10^{-11}$ cm² s⁻¹ and a diffusion barrier of ≈ 0.55 eV, this transport is slower than Li⁺ diffusion in SEs commonly paired with LMAs.^[90,96] During fast charging, high current densities at Li/SE anodes lead to accumulation of Li at the interface causing local mechanical stress,^[97] ultimately resulting in dendrite growth and short circuits. Therefore, the critical current density, which leads to cell failure, is reported to be below 1 mA cm⁻² for most SEs, far from the target of 12 mA cm⁻² defined previously.^[90] Recent reports from industry suggest much higher critical current densities for protected LMAs and Li/SE anodes, however, due to a lack of details we cannot comment on these results.

Li⁺ Diffusion in Graphite: First-principles calculations show that the Li⁺ diffusion barriers (ΔH_m in Equation (24)) between the graphene sheets of graphite are in the range of (0.2–0.5) eV.^[80,98,99] This range obtained from first-principles calculations is in accordance with experiments conducted in the range of (–40 to +40) °C, where an Arrhenius analysis yields a value of 0.363 eV.^[100] In contrast, the barrier for Li⁺ moving through graphene layers in graphite is in the order of (2–10) eV,^[79,80] close to the results for charge transfer, and therefore very unlikely compared to in-plane diffusion.

The Li⁺ diffusion barriers^[98] and chemical diffusion coefficients^[101] vary with the lithiation degree of graphite. For example, the diffusion barriers are 0.308 eV and 0.4 eV for Li_{0.2}C₆ and LiC₆, respectively.^[98] The increase of the diffusion barrier of Li⁺ in graphite with SOC is unfavorable for the fast-charging capability since it leads to a higher probability of Li metal deposition for high SOC.^[102–105]

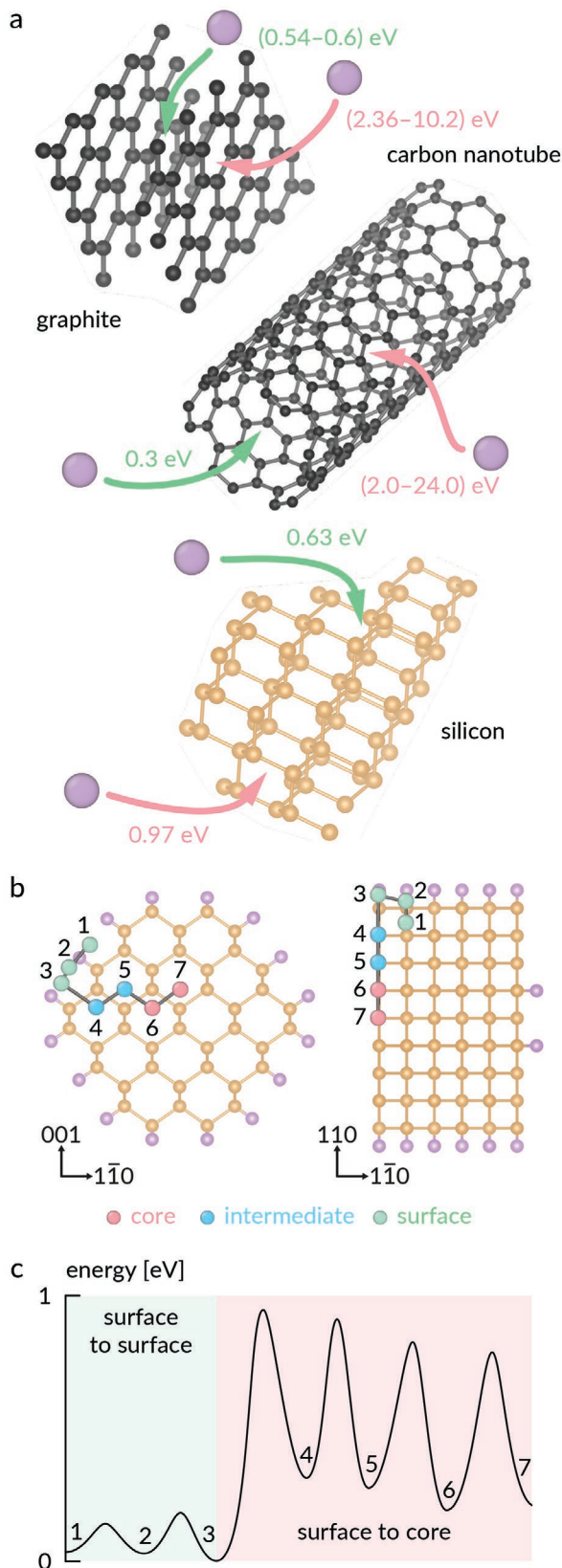


Figure 4. a) Preferred (green) and unfavored (red) diffusion pathways of lithium into graphite, carbon nanotubes, and silicon, as reported in

Cai et al. coated graphite particles with a 6.5 nm thick turbostratic carbon layer, which improves the initial Coulombic efficiency, the specific capacity, and the rate performance by creating additional active sites and improving the diffusion coefficient. At 3C, the capacity of the coated graphite particles is nearly doubled compared to the uncoated graphite particles and the cycle life is also improved.^[106]

Li⁺ Diffusion on Graphene: When graphene is the material of choice, Li⁺ is not intercalating, however, the diffusion barrier of Li⁺ on graphene ((0.247–0.376) eV) is still substantial and depends on the graphene sheet's curvature.^[107,108] For example, the diffusion barrier is lower on the concave side by ≈ 0.1 eV and higher on the convex side of a graphene sheet.^[108] The differences for adsorbed Li on both sides can therefore be in the order of 0.2 eV. Consequently, differences of one to two orders of magnitude can be expected for the diffusion coefficient.^[108]

Li Diffusion in Bulk Silicon: The energy barriers for the diffusion of a single Li atom in Si were obtained from first-principles calculations by different groups and are in the range of (0.47–0.6) eV.^[84–88] Chou et al. found that the diffusion barrier of Li atoms in Si is decreasing from 0.62 eV to 0.47 eV when an adjacent Li atom is present due to the Li–Li electrostatic repulsion.^[84] This electrostatic repulsion suggests that Li interstitials in Si tend to isolate themselves rather than clustering together.^[84] To the best of our knowledge, there are no barriers available for higher lithiation degrees of bulk Si.

Tritsaris et al. calculated the energy barrier for jumps of Li between tetrahedral interstitial sites of crystalline Si (0.55 eV).^[109] For amorphous Si, the same authors found energy barriers ranging from 0.1 eV to 2.4 eV for elemental hops of Li between equilibrium sites.^[109] In amorphous Si, not all diffusion pathways contribute equally in mediating the Li diffusion.^[109] The calculated long-range Li diffusion is comparable in crystalline and amorphous Si ($\approx 10^{-12}$ cm² s⁻¹).^[109] Ding et al. estimated a similar range of (10^{-13} to 10^{-12}) cm² s⁻¹ from electrochemical measurements (GITT, EIS, and cyclic voltammetry) for nano-Si.^[110] We like to note that these data should be considered with care as the conventional analysis of kinetic data only applies to single-phase materials.

Several attempts to increase the Si anode performance and overcome the existing challenges were reported. Different Si morphologies and nanostructures were examined in order to overcome the large volume expansion during the lithiation process, which eventually leads to the electrode fracture and pulverization of the active material and ease the diffusion of Li. Quiroga-González et al. presented a silicon microwire anode embedded at one end in a copper current collector. When comparing the microwire anode to other Si anode structures, higher areal capacities and charge density rates were achieved.^[111] A coral-like network of porous silicon nanowires interconnected by a thin carbon layer was synthesized

literature.^[75–78,82,83] For graphite, the activation barrier for intercalation through an edge plane is lower than through a basal plane. Intercalation into carbon nanotubes preferentially occurs through the open end compared to the walls. For silicon, the activation barrier is lower via the Si(100) surface than via the Si(111) surface. b) Diffusion pathway and c) corresponding barriers for Li⁺ in Si[110] nanowires. Data in (b, c) (redrawn) from ref. [89].

by Wang et al. and used for high-energy and high-power Li-ion batteries. The interconnected structure enables fast ion/electron diffusion along with a short ion diffusion path resulting from the porous Si nanowires. High specific capacities were presented at high charging rates of 7C, reaching over 500 charge–discharge cycles.^[112] Yu et al. showed the use of thin Si layers, which were previously reported as a successful solution for the volume expansion issue,^[113] on an elastomeric substrate in high-performance Li-ion batteries. The use of this multilayered structure resulted in a stable and high coulombic efficiency of up to 500 cycles.^[114] Manipulating the composition of the Si bulk can also improve the Si characteristics as displayed for heavily boron-doped Si anodes proving enhanced Li⁺ transport in the bulk and at the interface. Using this active material led to an increased rate performance even at high current rates (893 mA h g⁻¹ at 8C).^[115]

Silicon–carbon composites present an approach to overcome the drawbacks of sluggish electronic and ionic transport in pure silicon anodes. Thereby, the addition of carbon can improve the lithium diffusion coefficient by up to two orders of magnitude.^[116] This increases the fast-charging capability compared to pure silicon.^[117] Nevertheless, such composites are still hampered by low energy densities of the resulting full cells and high fabrication costs.^[118]

Li Diffusion in Silicene Sheets: Silicene, the Si analogue of graphene, was investigated theoretically via first-principles calculations by Tritsarlis et al.^[119] The authors found that the diffusion barrier for adsorbed Li on free-standing single-layer silicene (Li_xSi_{1-x}) sheets is 0.23 eV and 0.24 eV for $x = 0.11$ and $x = 0.47$, respectively.^[119] For double layer silicene, the diffusion barriers are 0.75 eV and 0.25 eV for $x = 0.06$ and $x = 0.41$, respectively,^[119] that is, the diffusion is enhanced for the higher Li content. The diffusion of Li through silicene double layers (0.56 eV) is favored over single layers (1.07 eV).^[119] In contrast to Si bulk material, lithiated silicene does most likely not suffer from irreversible structural changes, and the expected volume change is most likely in the order of <25%.^[119]

Li Diffusion in Silicon Nanowires: For single Li atoms inside Si nanowires, Zhang et al. found that the Li binding energy increases gradually with the nanowires' diameter until they reach the value for bulk Si (1.36 eV).^[89] For example, the Li binding energy at core sites of Si nanowires with the long axis along the [110] direction with (1.5, 2.0, and 2.5) nm diameter are (1.22, 1.34, and 1.35) eV, respectively.^[89]

Figure 4c shows the calculated barriers of Li diffusion into Si[110] nanowires of 1.5 nm diameter.^[89] The barrier for the surface-to-surface diffusion is the lowest (0.12–0.20) eV, followed by core-to-core diffusion (0.58 eV), however, the rate-determining step is the transition of Li into the Si nanowire (≈0.9 eV).^[89] This result is consistent with the experimentally observed core–shell phase distribution for Si nanowires.^[120]

Li Diffusion in Lithium Titanates: Tielens et al. calculated the energetic barrier for Li⁺ diffusion in Li_xTiO₂ for $x < 0.5$.^[121] Interestingly, the authors found that the diffusion barrier decreased with higher Li content from 1.31 to 0.67 eV.^[121] This means that the intercalation should be faster with increasing x in Li_xTiO₂, in contrast to the trend observed for Li_xC₆ (see Figure 5). We like to note that TiO₂ and Li₄Ti₅O₁₂ have very low electronic conductivity and the assumption that the chemical diffusion coefficient of

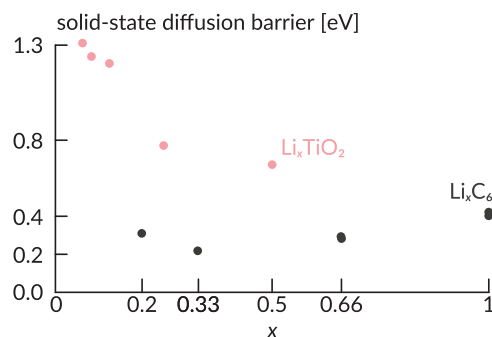


Figure 5. Comparison of activation energies of solid-state chemical diffusion coefficients for Li_xC₆^[98,99] and Li_xTiO₂.^[121]

Li can be replaced by that of Li⁺ is oversimplifying. Upon lithium insertion, the partial electronic conductivity increases, which also gives rise to a strong increase of \tilde{D}_{Li} .

The fast-charging capability of cells with LTO anodes^[122] is much better than with graphite, although the diffusion barriers are higher. This might be related to the general use of nano-sizing and nano-structuring of LTO materials^[123–126] leading to shorter solid-state diffusion paths. Recently, the low activation barriers in LTO were reported to originate from kinetic pathways formed by distorted face-sharing Li polyhedra at the two-phase boundaries between the stable end members Li₄Ti₅O₁₂ and Li₇Ti₅O₁₂. In the metastable intermediates, which are accessible at high rates and formed because of low interfacial energy in the material, the diffusion barrier was found to only be 0.216 eV (Li₅Ti₅O₁₂) compared to 0.343 eV and 0.455 eV in Li₄Ti₅O₁₂ and Li₇Ti₅O₁₂, respectively. This might thus be the actual reason for the improved fast-charging capability of LTO.^[127]

Li Diffusion in Bulk Tin: The diffusion barrier for a single Li atom in Sn as calculated by Chou et al. and Wang et al. is 0.39 eV.^[84,88] Similarly to Li diffusion in Si, the diffusion barrier is decreased to 0.33 eV for Sn if a second Li atom is present near the diffusing atom.^[84] This barrier reduction was found to be proportional to the Li–Li electrostatic repulsion.^[84]

A comparison of the Li diffusion barrier in Si and in Sn while using the same calculation method resulted in 0.62 eV and 0.39 eV, respectively.^[84] The lower barrier for Sn results from the higher flexibility of the lattice and the larger atomic size of Sn that allows for easier lattice expansion and therefore easier passage of Li atoms.^[84]

Li⁺ Diffusion in Niobium Tungsten Oxides: Lithium niobium tungsten oxides (Li_xNb₁₆W₅O₅₅ and Li_xNb₁₈W₁₆O₉₃) were reported as alternative anode materials for fast-charging applications by offering low diffusion barriers in the range (0.10–0.30) eV.^[128] Compared to LTO, they operate at similar potentials (on average 1.57 V vs Li⁺/Li) while offering significantly lower diffusion barriers without the need for nano-caling. Instead, they rely on an oxide superstructure enabling fast diffusion and stability.^[128]

Li⁺ Diffusion in Organic Anode Materials: Organic materials are discussed as possible resource-saving alternatives to state-of-the-art materials and have a potential for biodegradability.^[129] Different groups performed first-principles calculations on the Li⁺ diffusion in organic anode materials. Exemplary barriers are 0.12 eV and 0.21 eV for lithium terephthalate^[130] and di-lithium

terephthalate,^[131] respectively. These values are low compared to the value range of graphite,^[80,98,99] indicating a good fast-charging capability, however, the specific energies of organic anode materials investigated so far are very low.

SEI and Artificial SEI: The composition and structure of the SEI layer limit the charge transfer. The ideal SEI for fast-charging applications should be thin, homogeneous, long-term stable, and show high ionic and low electronic conductivity. All those characteristics can be obtained by forming an artificial SEI layer. When the SEI layer is formed during cycling, its properties are directly related, among others, to the electrolyte and anode material content.^[132] Most of these methods of in situ SEI alteration are based on electrolyte properties and will therefore be discussed in Section 5. Here, we will focus on how modification of the anode can improve SEI characteristics. Although many studies have been performed on electrolyte additives to modify the SEI layer properties,^[59] recent studies offer to conduct a pretreatment process using various techniques, which results in an artificial SEI layer possessing the desired properties.^[8,133]

A straightforward process presented by Wang et al. includes vigorous stirring of commercial graphite powder in aqueous solutions with different content of glucose ($w = (2.5\text{--}7.5)\%$) followed by a pyrolysis procedure. The samples coated with the glucose solution ($w = 5\%$) presented a high reversible capacity of $\approx 340 \text{ mA h g}^{-1}$ (at 60 mA g^{-1} for 45 cycles) alongside excellent rate capabilities.^[134] Another artificial SEI coating containing polyethylene glycol *tert*-octyl-phenyl ether (PEGPE) and polyallylamine (PAAM) was applied to different anode materials, including natural graphite (NG). The plateau associated with the SEI formation was not observed when comparing the treated and untreated NG active materials' cycling profiles. At high rates (10C), the treated NG presented an extremely high capacity of 336 mA h g^{-1} along with a retained capacity of 93% even after 100 cycles.^[135]

Moreover, chemical and thermal vapor deposition (CVD and TVD, respectively) are widely used as techniques to coat graphite particles with a homogeneous carbon-based artificial SEI layer resulting in a core-shell structure composite.^[133,136] For example, Yoshio and coworkers presented a TVD process of toluene at $1000 \text{ }^\circ\text{C}$. The carbon coating thickness was monitored by the feed time of the toluene vapor into the reaction tube. As the concentration of carbon coating on the graphite increases ($w = (0\text{--}17.6)\%$), the irreversible capacity loss obtained decreases while the coulombic efficiency increases.^[137]

Particle Size Distribution: The active material particle size distribution (PSD) affects the overall particle arrangement in the electrode microstructure while presenting varying Li solid-state diffusion lengths. The influence of the PSD on the high rate performance of the full cell was evaluated using various commercial graphite materials.^[138] Under fast-charging conditions, Li^+ ions arrive with a high flux at the anode material's surfaces, leading to lithiation gradients inside the particles, that is, the local lithiation degree is higher at the particle surfaces compared to the particle core.^[139] These lithiation gradients lead to stress evolution, for example, due to the Si particles' volume expansion,^[140] which can in turn lead to particle cracking.^[141] Larger particles are more prone to cracking^[142] due to the longer diffusion lengths. Furthermore, larger particles typically reach

lower charge capacities at high C-rates suggesting a limitation by slow solid-state Li^+ diffusion in graphite.^[143] However, a smaller mean particle size leads to higher specific surface areas and, therefore, to higher capacity losses during formation^[143] as well as to higher reaction rates with the electrolyte.^[144]

When similar flat lamellae-shaped graphites with different particle sizes ($(6\text{--}44 \text{ }\mu\text{m})$) were examined, a more facile and complete deintercalation process took place for the small-sized active material. In contrast, only partial lithiation occurred for the $44 \text{ }\mu\text{m}$ particles, confirming the considerations in section Single-Phase Intercalation Electrodes. During the high C-rate evaluations, not enough time is given for the Li^+ ions to intercalate into the graphite structure, directly leading to lower capacities.^[145]

Several computational studies addressed the influence of porosity and particle size on Li-ion battery performance and degradation. Röder and colleagues have presented the PSD impact (using the Weibull distribution) on the electrode capacity. Their numerical calculations, also confirmed by experimental work, demonstrated a decrease in the electrode capacity with larger mean radius. The higher internal resistance caused by longer diffusion pathways in larger particles can explain the results obtained, especially for high C-rates.^[146] Thus, in any case the mean particle size should satisfy the condition given in Equation (18).

Moreover, during cycling, the particles may crack due to degradation processes (e.g., in the case of Si), leading to reduced particle size alongside the particles' electrical disconnection. Therefore, although the diffusion pathway shortens due to the decrease in the mean particle size, the electrode performance drops considerably, especially for high discharge rates, due to the active material's disconnection.^[146]

Porosity of Particles: High diffusion resistance values alongside low rate capacities are only some of the difficulties caused by the long diffusion distances of Li^+ ions in graphite particles. One of the existing solutions to the long diffusion length is producing porous graphite active material that enables high charging rates.

An etching process using 1 mol L^{-1} potassium hydroxide solution followed by drying at $80 \text{ }^\circ\text{C}$ and an annealing process at $800 \text{ }^\circ\text{C}$ in nitrogen gas for two hours resulted in nanometer-scale pores.^[147] The specific capacities obtained by the etched graphite were higher than the pristine material, in particular for high current densities.^[147] A nickel-catalyzed steam gasification process was also proven to result in a porous graphite structure.^[148] The synthesized active material exhibited a longer cycling life at high charging rates (5C) in addition to the higher reversible capacity (at 35 mA g^{-1}).^[148]

3.1.2. Limitation of Fast Charging on Electrode Level

The need for high rates and increased energy densities led researchers to develop different anode electrode compositions and microstructures to address existing challenges. Although the study of the material itself led to significant improvements in the overall performance, the engineering approach must not be neglected. Controlling the electrode thickness, increasing the electrode's porosity, reducing its tortuosity, and decreasing the content of non-active additives (such as the

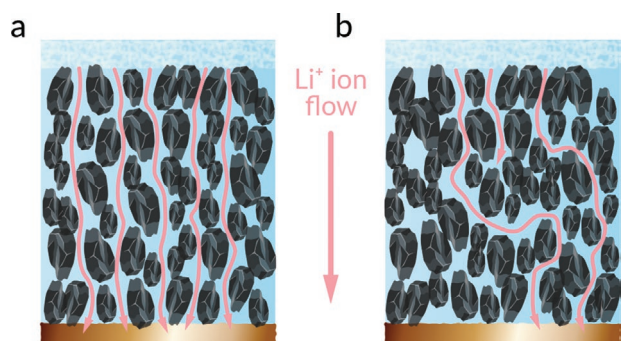


Figure 6. a) Efficient ionic pathways and b) dead-end pores alongside non-efficient pathways resulting in increased tortuosity.

binder and conductive carbon) have already presented promising results, even when using well-known anode materials such as graphite.

Effects of the Electrode Microstructure: Anode Tortuosity. The anode fabrication process begins with the preparation of a multi-component-containing slurry. Later, the mixture goes through the casting and calendaring processes, creating tortuous diffusion paths in the porous active material layer, in which the charge carriers are transported. Tortuosity can be defined as the ion transport path length due to the porous microstructure existing in the electrode.^[16,149] A direct ionic pathway (**Figure 6a**), therefore, has a tortuosity value of $\tau = 1$. Several reports correlated the electrode's porosity and tortuosity both by calculations alongside experimental work to reach an optimization in the electrode structure parameters.^[18] Also, impedance studies were found to quantify electrode tortuosity, allowing meaningful experimental results that support the numerical calculations.^[16,17] Although closely connected to porosity, tortuosity describes the effective ionic pathways, whereas porosity describes the fraction of voids. Therefore, highly porous electrodes do not necessarily have low tortuosity values, for example in the case of a high fraction of dead-end pores, as presented in **Figure 6b**.

When thick, highly loaded electrodes are used, the high rates are limited by the diffusion paths inside the electrode's microstructure.^[19,150–153] High tortuosity values are a significant limitation that directly influences the battery's ability to sustain high cycling rates alongside higher power densities. Reduction in the ion's path lengths in the electrodes will eventually result in faster and more efficient diffusion (reduction of the parameter β), increasing the limiting current density j_{lim} , which directly influences the electrolyte overpotential on the anode side $\Delta\phi_{EL}^a$, as detailed in Section 2.2.1. The slow migration rates related to high tortuosity values can lead to significant ohmic and concentration polarization, which eventually prevents utilizing the whole available active material. Eventually, the overpotential for ion transport due to the sluggish electrode kinetics of the anode can lead to capacity fade and lithium deposition on the electrode surface close to the separator.^[154,155]

Various studies focus on improving transport limitations by using three-dimensional electrode architectures where the controlled electrode particle shape and orientation results in preferential paths with low tortuosity for the Li^+ ions. It is crucial to compare structured and unstructured electrodes with the same

loadings to assess the effect of tortuosity correctly. Studies conducted using a mesoporous anatase microstructure, presenting uniform and connected pores, resulted in improved performance compared to the optimal result previously reported for anatase nanoparticles.^[156] Moreover, calculations performed for magnetically aligned graphite flakes (see **Figure 6a**) indicated a reduction in the out-of-plane tortuosity by a factor of nearly four.^[157] Additionally, the rate capability test presented three times higher specific charge, more defined potential plateau, and much lower overpotential when aligned graphite flakes were used.

A co-extrusion process followed by a sintering method resulting in controlled tortuosity while maintaining the electrode porosity and thickness was previously reported by Bae and coworkers.^[158] Alternative approaches, such as laser patterning, manage to manipulate the electrode structure after fabrication, creating an array of vertical channels serving as linear diffusion paths.^[159,160]

Anode Porosity. The porosity of the anode is crucial for proper electrode performance since the penetration of electrolyte into the electrode bulk is directly affected by the voids present between the active material particles. The control of porosity during electrode manufacturing is a compromise between electronic and ionic conductivity.^[161] While a higher porosity is favorable for the ionic conductivity, it also reduces the areal capacity for the same anode coating thickness. Anodes with higher porosity and the same areal capacity result in a thicker active material layer, leading to a lower energy density on cell level. For example, Colclasure et al. showed that the full cell volumetric energy density achieved for an electrode of 4 mA h cm^{-2} with 40% porosity is less than for a 3 mA h cm^{-2} anode with 30% porosity.^[19] Increasing the porosity to high levels is, therefore, not an effective strategy to improve the fast-charging capability.

The ongoing growth of the SEI layers on the anode surface^[162] is a well-known aging mechanism leading to clogging of the electrode pores^[163] and therefore reducing the porosity during battery life. A microkinetic Li-ion battery model predicted the aging characteristics resulting from the continuous clogging of electrode pores due to SEI formation (see **Figure 7**).^[164] A significant electrolyte overpotential is generated after ≈ 3000 cycles, enabling the deposition of lithium metal.^[164] The positive feedback caused by the lithium metal deposition and the decrease in porosity accelerates the aging process and can lead to a sudden drop in cell capacity.^[164]

Theoretical and experimental studies have previously discussed optimizing the electrode porosity, depending on the chemical composition of the electrodes. Zheng and coworkers have presented the connection between the electrode inactive components and its porosity, resulting in an optimum mass fraction (w) of 8% of inert material while calendaring the electrode to at least 30% porosity.^[20] The same group has also reported optimal performance while using a combination of PVDF ($w = 8\%$) with acetylene black ($w = 7\%$) while calendaring the electrodes to (30–40)% porosity.^[21] Another study presented a decrease in the first and second cycle capacity alongside higher irreversible capacity loss when increasing the graphite anode density from 0.9 g cm^{-3} (where optimal results were obtained) to 1.38 g cm^{-3} .^[165] Therefore, when deciding



Figure 7. Illustration of SEI growth and pore-clogging during cycling inducing polarization and therefore promoting Li metal deposition.

on the electrode porosity, facile Li^+ ion penetration alongside the inactive material's content and the rates applied should be considered.

Anode Coating Thickness: An effective way to increase the fast-charging capability, which is also applied in state-of-the-art commercial cells^[166,167] are thin anode coatings.^[19,138] However, in the case of low coating thicknesses, the active to inactive material ratio is unfavorable in terms of specific energies and low energy densities, resulting in increased costs.^[13]

One effective method to increase the volume ratio of active and inactive materials is increasing the electrode thickness.^[166] In commercial cells, the single-sided coating thicknesses are currently up to $\approx 100 \mu\text{m}$.^[166] However, various studies went to much higher values. Numerical models were created to study the relation between thickness and applied charging C-rate. The advantages of thick electrodes with respect to energy density were compromised by the internal cell polarization and low utilization of the active material resulting in a critical thickness.^[152,168]

Sivakkumar et al. studied Li/graphite half cell behavior at high current densities (up to 60C) while using different graphite anode thicknesses ((12–100) μm). Thinner electrode coatings presented superior performance while applying a C/10 intercalation rate alongside varying deintercalation currents (up to 60C). When the same rate, 20C, was used for the intercalation and deintercalation processes, the 100 μm thick coating presented a sharp drop resulting in only 2% gravimetric deintercalation capacity retention.^[138]

Gallagher and colleagues presented a correlation between the electrode loading and various parameters such as current density, electrolyte transport, and overall cell performance while using numerical calculations and experimental results.^[151] The analyses presented a significant drop in the areal capacity utilization due to salt depletion. On the other hand, when proper current densities, which allow for full access to the available capacity while avoiding lithium deposition, were chosen, stable cycling was achieved.^[151]

Effects of Anode Potential: Unfavorable deposition of lithium metal on the anode becomes thermodynamically possible if the anode potential becomes lower than 0 V versus Li^+/Li ,^[103,169–171] corresponding to an overpotential of (0.065–0.2) V in the case of graphite.^[171] This condition is more likely to be fulfilled in front of the anode surface (near the separator) due to higher Li^+ activity^[105] and less likely near the current collector due to depletion of Li^+ ions.^[153] For pouch cells, Li metal deposition on the anode surface leads to measurable thickness changes.^[172] Simulations taking the anode microstructure into account show that the lithium deposition condition is first fulfilled on the anode surface.^[170] Consistent with this, post-mortem analysis after cycling showed that lithium metal is mostly deposited

on the anode surface.^[173–175] The anode potential and therefore the tendency of lithium metal deposition is affected by electrolyte additives,^[176] anode active materials,^[177] the anode coating thickness,^[38] operating parameters such as temperature, C-rate, and SOC^[38,103–105,177] as well as the ratio of the areal capacities between anode and cathode (N/P ratio).^[19,178–181]

The N/P ratio is typically in the range of 1.1 to 1.2.^[19,178–182] N/P ratios < 1 lead to Li metal deposition, since the areal capacity of the cathode exceeds that of the anode. Mao et al. described the N/P ratio as a function of the C-rate for charging graphite/ $\text{LiNi}_{0.8}\text{Co}_{0.1}\text{Mn}_{0.1}\text{O}_2$ (NCM811) pouch cells.^[37] As an example, the authors found for their electrodes optimum N/P ratios of 1.15, 1.00, and 0.5 for C/10, 3C, and 4C, respectively.^[37]

The anode potential is further related to properties on the material level. For example, larger particles and higher barriers for Li migration into the active material and for solid-state diffusion within the active material show a higher tendency of lithium metal deposition due to stronger polarization effects. In contrast, high anode potentials as in the case of LTO materials avoid lithium metal deposition while decreasing the cell voltage and therefore the specific energy and energy density on cell level.

By preparing anodes with different ratios of graphite and hard carbon ((0–100)% hard carbon), Chen et al. found a significant improvement of capacity retention after 500 cycles with 4C and 6C for 50% graphite/hard carbon.^[183] The authors used industrially relevant areal densities (3 mA h cm^{-2}) and multi-layer pouch full cells. The improvement was attributed to enhanced homogeneity of the reaction within the anode and mitigation of Li plating.

For the special case of LMAs, lithium metal is deposited directly on lithium metal or a suitable current collector. Here, lithium plating is not an issue anymore, but a desired feature. In combination with SEs stable against lithium metal this opens the possibility of fast-charging capable SSBs. Bad contact between the two solid phases is still an issue, however, among others, which will be further detailed in Section 5.2.2. Along with the aforementioned limited vacancy diffusion leading to dendrite propagation this poses major challenges for fast charging of LMAs.^[90]

3.1.3. Degradation of Anode Induced by Fast Charging

The main degradation modes related to fast charging are i) Li deposition on the anode and subsequent reaction with electrolyte as well as the formation of “dead Li,” ii) increased reaction rates resulting from heating of the cell due to current flow, and iii) particle cracks.

In literature, the mechanism of lithium metal deposition is mostly investigated for graphite anodes,^[102,105,172–175,177,184,185] although it is also studied in Si/C composite anodes.^[186] The phenomenon of lithium metal deposition on anodes is highly critical since it can reduce safety by dendrite growth^[187] and exothermic reactions.^[175,188] On graphite anodes, lithium metal deposition is favored during charging at low temperatures,^[38,102,103,185] high charging C-rates,^[103,185] and high SOC, ^[103] as well as their combination.^[104,185] These effects can be counteracted by avoiding negative anode potentials, for example, by optimized charging protocols^[103–105] or by internal heating of cells during charging.^[189]

Additionally, cell heating due to current flow during charging can have significant influence on the anode potential. Tippmann et al. showed by simulations with and without a coupled thermal model (i.e., with and without heating due to the charging current) that the anode potential is shifted to higher values.^[103] Therefore, larger cells, which usually show a stronger heating due to current flow,^[166,182] are likely to show a lower tendency to lithium metal deposition compared to smaller cells.

In the case of fast charging at high ambient temperatures or strong cell heating due to high charging currents, different aging mechanisms come into play. High temperatures are known to suppress lithium deposition; however, SEI growth is favored at elevated temperatures.^[162]

The graphite laminated structure (interlayer spacing of 0.335 nm^[137]) enables Li⁺ intercalation. Simultaneously, solvent co-intercalation may occur, especially at high charging rates, causing volume expansion and exfoliation (≈10%) followed by structural degradation of graphite.^[190] When fast charging rates are applied, rapid Li⁺ intercalation is required. Due to the existing charge-transfer limitations, a large concentration gradient can be created, leading to an inhomogeneous stress distribution among the graphite particles. Cracks in the material and electrode microstructure, leading to isolation of graphite particles and even disconnection of the active material from the current collector, can occur. Graphite lattice rearrangement can cause further mechanical degradation and defects during the intercalation process.^[59]

When alloy metal host materials are being used as negative electrodes, severe volume expansion can be obtained. Winter and coworkers have shown that massive volume changes can be prevented by keeping a small particle size of the host material ((10–20) nm for Sn₂Fe and SnFe₃C intermetallic phases, for example^[191]).

3.2. Advantages and Disadvantages of Existing Materials Fulfilling Fast-Charging Capability

As discussed above, many obstacles can hinder the Li-ion battery's abilities when high C-rates are applied. Several studies have been conducted to improve Li⁺ ion migration inside the active material by various modifications performed on the active material itself as well as on the electrode level. **Table 1** summarizes numerous improvements of well-known anode Li-ion materials and their performance at high rates.

Figure 8a correlates the diffusion barriers in different anode active materials (Section Solid-State Li⁺ Diffusion Inside Active Materials) with the specific capacities on the material level. A nearly linear correlation is obtained for Si, Sn, graphene, graphite, and organic materials, thus materials with higher specific capacity often show worse fast-charging capability. On the other hand, lower C-rates already lead to higher absolute currents for high capacity materials.

LTO does not fit into the correlation in **Figure 8a** since it combines a low specific capacity with a high diffusion barrier. However, for LTO mostly nanoscale materials are utilized^[123–126,205] and therefore the shorter diffusion paths compensate the higher barriers. Furthermore, nanosized materials usually cause higher initial capacity losses due to higher surface area where SEI is formed. This is not the case for LTO due to its higher anode potential, which is inside the stability window of the electrolyte. Therefore, the higher surface area does not lead to a new SEI layer formation in each cycle. However, the higher anode potential contributes to the drawback of lower specific energy for LTO.

On the material level, the goal is to combine materials with higher specific capacities and energies alongside lower diffusion barriers, as well as lower charge-transfer barriers. **Figure 8a** suggests that these requirements seem to exclude each other; however, the exception of LTO shows that there is hope to find such materials.

Another approach is the use of smaller particles, for instance nanosized materials. The shorter diffusion paths of Li⁺ ions in nanoparticles enables improved solid-state diffusion and therefore a better utilization of the materials during fast-charging (see **Figure 8d**). However, this is limited by higher irreversible losses^[143] and increased tortuosity. Therefore, a further target for improved fast-charging capability is nanosized materials with high specific energy and energy density, however, without high irreversible losses.

Figure 8c shows a similar trend on the cell level for commercially available cells as **Figure 8a** for materials. In **Figure 8c**, cells with LTO anodes fit into the linear correlation together with graphite and Si/graphite since the smaller particle size of LTO is already included in the evaluation on cell level. The target on the cell level is reaching a higher specific energy while preserving the short charging time. The key is not only on the material level, however optimization on the electrode level is required as well.

On the electrode level, the increased specific energy and lower costs are usually achieved by thicker electrode coatings,^[13,19,166,167] however, this leads to lower utilization of the negative electrode and favors Li deposition as illustrated in **Figure 8e**. The aim is to construct electrodes with both higher loading and higher fast-charging capability and lower susceptibility to Li deposition. In **Figure 8b**, the effect of particle shape on tortuosity is shown.^[19] In this example, spherical and potato-shaped particles on material level lead to a lower and higher tortuosity on electrode level, respectively.^[19] Alternative approaches use aligned particles^[157] or holes on the anode coating to improve the tortuosity.^[159,160] It is, however, always critical to cross-check whether such approaches lead to a decrease in energy density, for example, by removing active material. In the case that active materials are removed in modified electrodes, they must be compared with untreated electrodes with the same loading.

Table 1. Several active materials and their modifications for fast-charging applications.

Active material	Material limitations	Material modifications for high-rate applications	Active material loading	Performance reported (number of cycles, capacity, current density)	Ref.
Graphite/graphene	Unstable SEI layer due to the expansion and contraction of the graphite leading to high ICL; sluggish intercalation kinetics and low lithiation voltage resulting in metallic lithium deposition	Mildly oxidized graphite resulting in extended <i>d</i> -spacing while conserving good electrical conductivity		No significant decrease in capacity from the value obtained at 0.1C up until 10C; the capacity value was maintained close to the $Q_{0.1C}$ up until 50C	[192]
		Magnetically aligned graphite	9.1 mg cm ⁻²	Higher capacities were obtained for the aligned material at C/2–2C; the specific charge capacity achieved was higher (by the factor of 1.6) than the reference material (at 1C for 50 cycles)	[157]
		Graphene-like graphite prepared by an oxidation process using KClO ₃ and HNO ₃ followed by a heating treatment	5 mg cm ⁻²	Capacity retention of 79% and 39% at 6C (100 cycles) for GLG and graphite, respectively	[193]
		3D interconnected porous nitrogen-doped graphene foam (NGF) with encapsulated Ge quantum dot@ nitrogen-doped graphene yolk-shell nanoarchitecture (Ge-QD@NG/NGF)	1.8 mg cm ⁻²	Over 800 mA h g ⁻¹ at 40C (200 cycles) alongside extended cycling capability (≈96% reversible capacity retention up to 1000 cycles)	[194]
		Hybrid anodes with a uniform mixture of graphite and hard carbon	≈3 mA h cm ⁻² anode areal capacity loading (depending on the graphite/hard carbon blend ratio)	Anodes containing <i>w</i> = 50% graphite retain 87% (4C) and 82% (6C) of their initial specific energy after 500 cycles	[183]
		Nanoscale turbostratic carbon-coated graphite	1.0 mA h cm ⁻² anode areal capacity loading	A significant improvement in initial Coulombic efficiency, specific capacity, and rate performance	[106]
Hard carbons	A lower density and initial coulombic efficiency in comparison to graphite; large irreversible capacity, low packing density, and hysteresis in the voltage profile	Polyacrylonitrile (PAN) hard carbon	5.2 mg cm ⁻²	The PAN hard carbon presents a charge capacity of 135.4 mA h g ⁻¹ at 3C (100 cycles), exceeding the graphite electrode's value (106.0 mA h g ⁻¹)	[195]
		Siloxane-grafted nano-SiO _{0.26} /hard-carbon composite	1.2 mg cm ⁻²	(916–750) mA h g ⁻¹ at 0.2C (100 cycles); ≈650 mA h g ⁻¹ at 10C (100 cycles)	[196]
Li	Fragile SEI layer leads to Li dendrite growth during cycling; the cyclability is possible for most Li anodes only under low current densities (<1 mA cm ⁻²)	Pretreatment of the Li anode surface using a thin silicon wafer ([20–30] μm), resulting in a thin, highly ionically conductive Li ₂ Si film		Specific capacity of ≈390 mA h g ⁻¹ at 2 mA cm ⁻² (150 cycles)	[197]
		An over-lithiation process of mesoporous AlF ₃ resulting in a nanocomposite of Li/Al ₄ Li ₉ -LiF (LAFN)		Specific capacities of (140, 131, 113, and ≈80) mA h g ⁻¹ at (0.2, 1, 4, and 10)C, respectively (≈10 cycles); long term cyclability at 1C resulted in ≈130 mA h g ⁻¹ (100 cycles)	[198]
Si	Electrode disintegration and high charge-transfer resistance due to the extreme volume change during cycling (>300%) alongside low electrical conductivity (≈10 ⁻⁴ S ⁻¹)	An edge-plane activated graphite with an-Si nanolayer (SEAG) prepared by nickel-catalyzed hydrogenation followed by a chemical vapor deposition (CVD) process using acetylene and silane gas		Less Li deposition after applying high charging currents avoiding the drastic capacity degradation	[199]

Table 1. Continued.

Active material	Material limitations	Material modifications for high-rate applications	Active material loading	Performance reported (number of cycles, capacity, current density)	Ref.
		A composite layer-by-layer silicon/reduced graphene oxide (Si/RGO) anode material with a post-laser-shock (LS) compression treatment	(0.1–1) mg cm ⁻²	≈1850 mA h g ⁻¹ at 6 A g ⁻¹ after 200 cycles; ≈1200 mA h g ⁻¹ at 15 A g ⁻¹ after 1000 cycles	[117]
LTO	Low electrical conductivity (≈(10 ⁻⁸ –10 ⁻¹³) S cm ⁻¹) and slow Li ⁺ ion diffusion (≈(10 ⁻⁸ –10 ⁻¹³) cm ² s ⁻¹)	LTO porous particles filled up with N-doped carbons	10 mg cm ⁻²	Better capacity retention in comparison to commercial LTO while applying 1C, 45 °C (300 cycles)	[200]
Conversion materials	Poor cycle stability due to large structural reorganization leading to massive volume changes; extremely high Coulombic inefficiencies and large irreversible capacity and voltage hysteresis between discharge and charge steps	α-Fe ₂ O ₃ hollow spheres with sheet-like sub-units		Reversible capacity of 710 mA h g ⁻¹ at 200 mA g ⁻¹ (100 cycles)	[201]
		Carbon-decorated Fe ₃ O ₄ nanowires		≈830 mA h g ⁻¹ at 0.1C (50 cycles); when higher charge rates were applied (5C), the carbon decorated Fe ₃ O ₄ nanowires delivered a high capacity of 600 mA h g ⁻¹	[202]
		CoO/graphene nanocomposite: ultrafine CoO nanocrystals densely attached to the graphene nanosheets		≈1018 mA h g ⁻¹ at 200 mA g ⁻¹ (520 cycles); the synthesized material presents good rate capability—at high rates (1600 mA g ⁻¹), a favorable specific capacity was obtained (531.2 mA h g ⁻¹)	[203]
Organic materials	Low capacity of the conducting polymer, low electronic conductivity, and dissolution of conjugated carbonyl compounds	2D covalent organic framework (COF) based on covalently connected polyporphyrin with 4-thiophenephenyl groups (TThPP)	0.2 mg cm ⁻²	Good rate capability resulted in (666, 519, 384, 271, and 195) mA h g ⁻¹ when (0.2, 0.5, 1, 2, and 4) A g ⁻¹ rates were applied; cycling performance evaluations resulted in ≈400 mA h g ⁻¹ at 1 A g ⁻¹ (200 cycles)	[204]

3.3. Requirements on Material and Electrode Level

As deduced from theoretical considerations in Section 2 and corroborated with experimental data in the current Section 3, improved anode materials with high fast-charging capability should ideally show the following properties:

- i) low energetic barriers for Li⁺ transfer into the material;
- ii) low energy barriers for Li solid-state diffusion inside the active material. According to Equation (18), this directly results in
- iii) small particle size with rather narrow PSD, for example, nanoparticles, while sustaining processability and low irreversible losses.

Furthermore, high long-term stability in contact to the electrolyte and in a wide temperature range is required. In addition, high energy density and specific energy are needed, while safety must be sufficiently high.

Improved negative electrodes with high fast-charging capability should ideally show the following properties:

- i) a tortuosity value near one, which is difficult since the preferred small particles adversely affect the tortuosity;

- ii) an optimized porosity regarding electronic and ionic conductivity of the electrode layer;
- iii) an electrode expansion as small as possible.

Combined, these properties can result in a very low or even negligible tendency of lithium metal deposition, that is, in anode potentials above 0 V versus Li⁺/Li. However, the anode potential should not be too high in order to retain high specific energies. Furthermore, without changing the properties above, the areal capacity must be high enough, that is, by high electrode loading to increase the ratio of active to inactive material and therefore lower costs.

On cell level, fast-charging capability needs to be improved regarding cell heating due to current flow and charging strategies: i) At low ambient temperatures, cell heating is desired to improve migration and diffusion kinetics and to hinder Li deposition on the anode. Examples are cell designs with internal heating.^[155,189,206] ii) At high ambient temperatures, cell heating should be hindered by cell designs for improved heat dissipation. iii) Charging strategies to prevent Li deposition by preventing negative anode potentials versus Li⁺/Li.

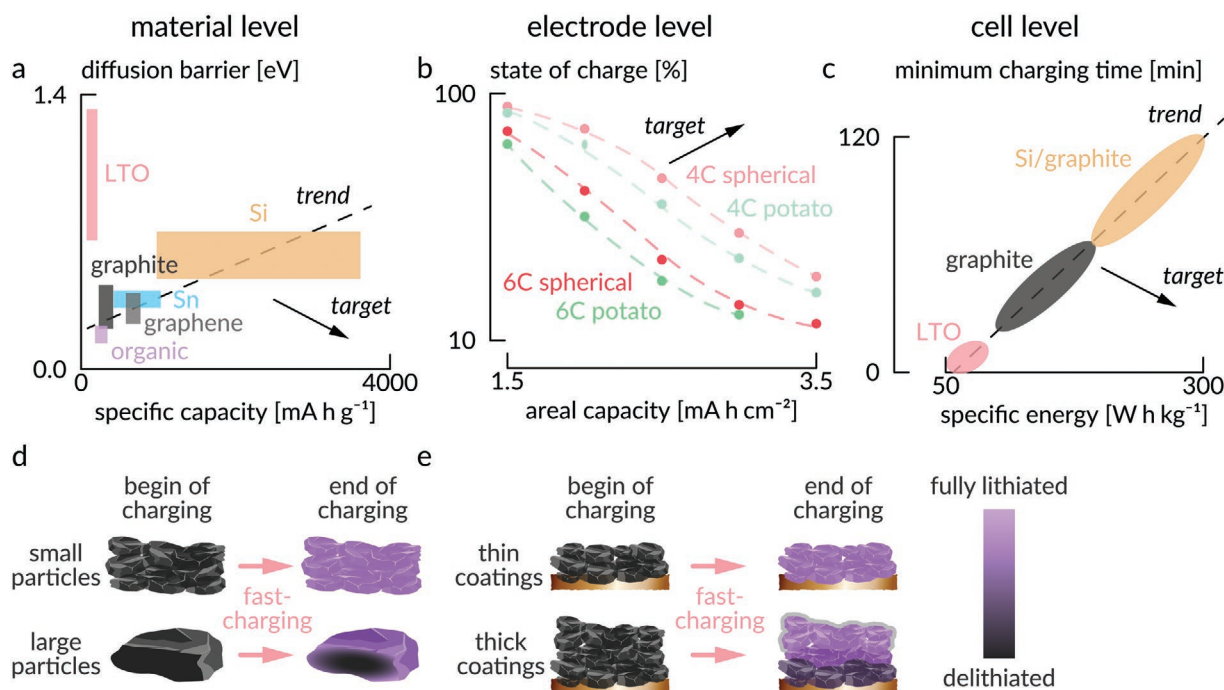


Figure 8. General trends for fast-charging capability from material to cell level: a) Solid-state diffusion barriers of Li in different anode active materials as a function of specific capacity on the material level. b) Calculation of charged capacity after 4C and 6C CC charging to 4.2 V as a function of anode loading. Spherical (lower electrode tortuosity) and potato-shaped (higher electrode tortuosity) particles were used. Data (redrawn) from ref. [19]. c) Minimum charging time (C-rate⁻¹) as specified in data sheets from commercial cells for LTO (Toshiba SCiB cells), graphite, and Si/graphite composite anodes as a function of specific energy on cell level. Illustration of material utilization for d) small/large active material particles and e) thin/thick anode coatings.

4. Cathode

In this section, the kinetic aspects associated with Li⁺ transport in/at the cathode are reviewed and rated according to their relevance for fast charging. A simple way to obtain insights into the kinetics of battery electrodes, thus their fast-charging capability during operation is to monitor the voltage or potential.^[2,22,77,207] For a battery cell, the overvoltages and voltage hysteresis, that is, the voltage/potential difference between the obtained charge and

discharge curves, reveals the overall internal resistance of the cell as exemplarily shown in **Figure 9a**.^[58,208] Moreover, with the support of a reference electrode,^[209] the individual contribution of both electrodes, cathode and anode, on the overall internal resistance can be distinguished via the respective electrode potentials (overpotentials and/or potential hysteresis $\Delta\phi^c$ and $\Delta\phi^a$).^[210,211,212] Simple electrochemical techniques allow for a systematic investigation of kinetic aspects for various cathode active materials as exemplarily shown in **Figure 9b**.^[34,213] Typically, cathodes contribute

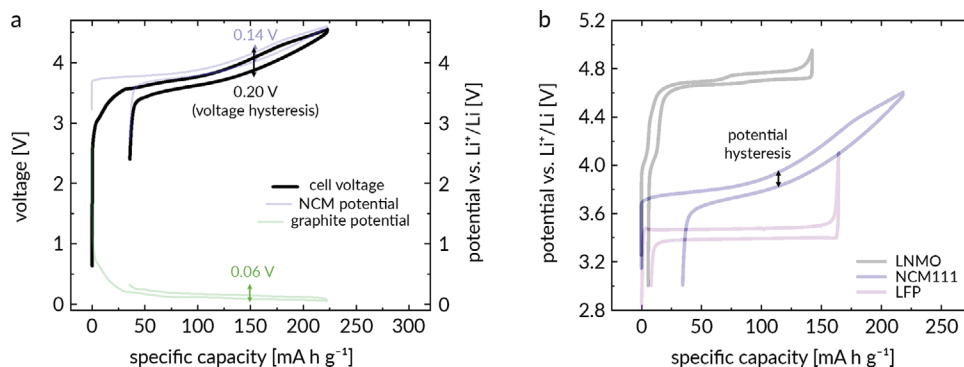


Figure 9. a) Initial charge/discharge cycle of an NCM||graphite full cell setup including a reference electrode for monitoring the potential behavior of individual electrodes. The voltage hysteresis (here: $\Delta\phi = 0.20$ V) as an indication for overall internal cell resistance is the sum of the potential hysteresis of both, the cathode (here: $\Delta\phi^c = 0.14$ V) and anode (here: $\Delta\phi^a = 0.06$ V). Data (redrawn) from refs. [210,214]. b) The overall kinetic aspects of a single electrode, for example, a cathode with varied CAMs can consequently be simply indicated by monitoring the cathode potential during operation. Data (redrawn) from refs. [215–217].

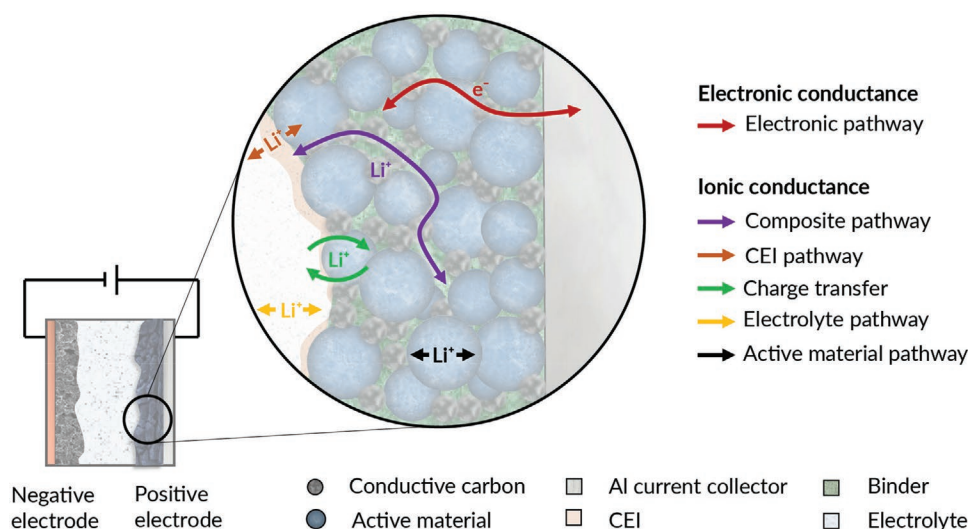


Figure 10. Schematic illustration of various Li^+ and e^- pathways, which can impact the internal resistance. Relevance and implication of the individual contributions to the overall internal resistance and fast charge capability are discussed in the main text. Redrawn from ref. [22].

most to the internal cell resistance as also seen in the example of Figure 9a, where the voltage hysteresis amounts to 0.14 V for the NCM cathode contrary to 0.06 V for the graphite anode.

The cathode as a particle-type composite electrode includes inactive ingredients, that is, a binder for mechanical robustness/structural integrity as well as conductive carbon for improved electronic conductance and electrolyte uptake.^[218] Consequently, the complex nature of the cathode, both on the material level and on the composite electrode level, involves several processes and charge pathways, which contribute to the cathode's internal resistance as shown in Figure 10.^[22]

4.1. Limitation of Fast Charging on the Material Level

4.1.1. Influences of the Crystal Structure

Insight into relevant factors controlling the internal resistance, which were already deduced fundamentally in Section 2.1.1, can also be obtained from in situ monitoring of kinetics during the

charge process, that is, through changes in overpotentials. The charge profiles of $\text{LiNi}_{1/3}\text{Co}_{1/3}\text{Mn}_{1/3}\text{O}_2$ (NCM111) as an exemplary CAM for various specific charge currents are depicted in Figure 11a (compare also Figure 2a). The accompanied increase in overpotentials $\Delta\phi_{\text{AM}}^{\text{c}}$ is not constant, but rather SOC dependent with a minimum at a specific charge capacity of $\approx 140 \text{ mA h g}^{-1}$, corresponding to an Li^+ extraction ratio of $\approx 50\%$ and to step II in Figure 2. At this SOC, the maximal c -parameter (proportional to the Li^+ interlayer distance) of NCM111 is observed, as shown in Figure 11b. This implies a direct relation with the development of overpotentials in the entire cathode. In other words, the kinetic aspect and internal resistance overwhelmingly depend on the used CAM and changes associated with the CAM. In line with this, changes of solely the CAMs, for example, LiFePO_4 (LFP), NCM111, or $\text{LiNi}_{0.5}\text{Mn}_{1.5}\text{O}_4$ (LNMO), lead to significant changes of the cathodes' overpotential as shown in Figure 9b, while the other aspects obviously play only a minor role.

The SOC dependence of the overpotential $\Delta\phi_{\text{AM}}^{\text{c}}$ can be related to the crystal structure of state-of-the-art CAMs, that is, layered oxides (example: NCM111), which is depicted in Figure 12,

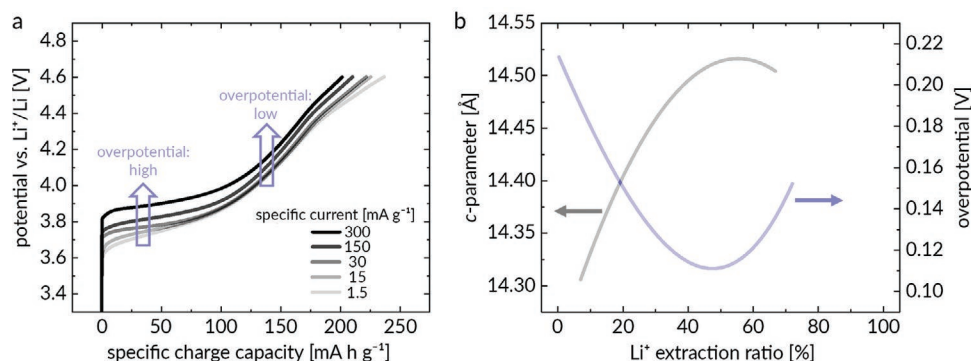


Figure 11. a) Initial charge curves of NCM111 for varied specific charge currents demonstrating SOC dependence of the overpotential $\Delta\phi_{\text{AM}}^{\text{c}}$. Adapted with permission.^[22] Copyright 2016, IOP Publishing. b) The overpotential behavior can be related with the c -parameter of the NCM111 structure. At approximately 50% Li^+ extraction ratio, the maximum c -parameter and lowest overpotential (=best kinetics) is observed, which can be attributed to the widest Li^+ interlayer distance, thus to maximized Li^+ mobility. Hence, the cathode overpotentials can predominantly be assigned to the Li^+ pathway within the active material. Data (redrawn) from ref. [22].

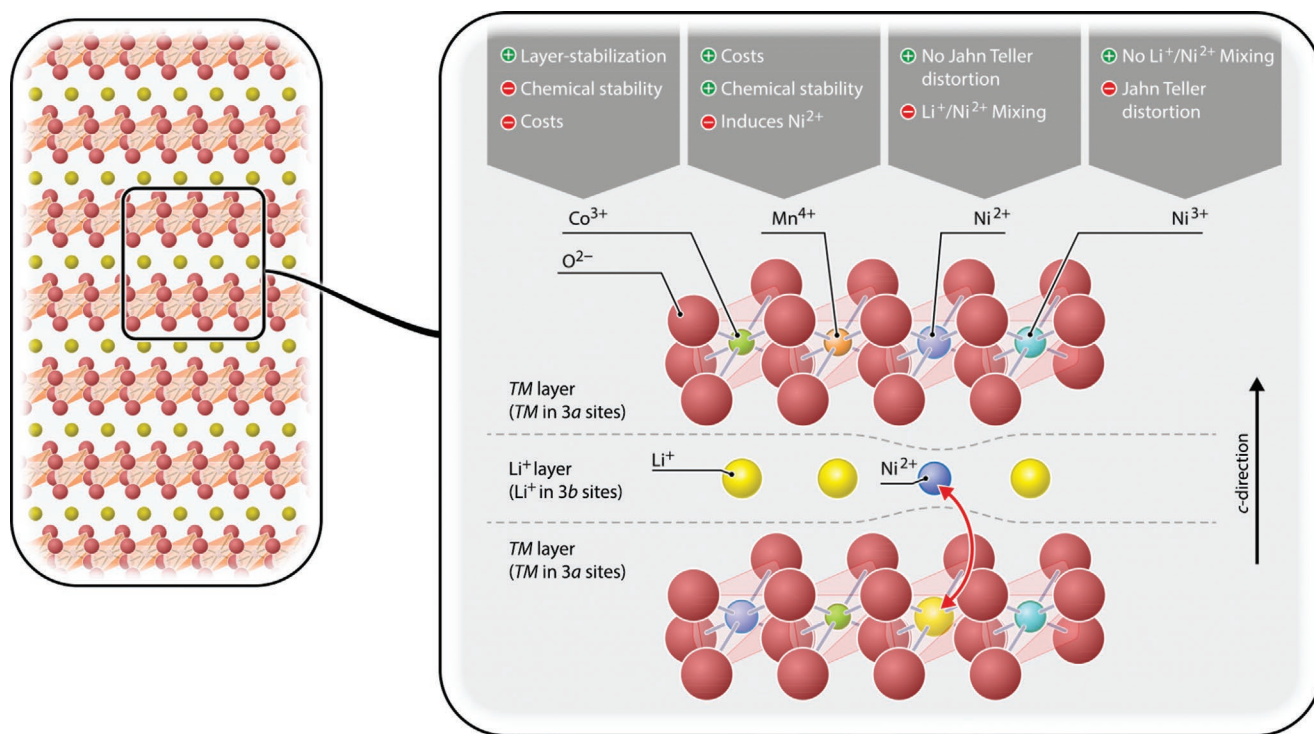


Figure 12. Crystal structure of the state-of-the-art CAM, that is, layered oxides like NCM. Each transition metal contribution has pros and cons rendering compromises necessary. Particularly the Li⁺/Ni²⁺ mixing effect is relevant for fast charge as it dictates cathode kinetics via decreasing the chemical diffusion coefficient within the CAM as a rate-limiting aspect. Adapted with permission.^[215] Copyright 2017, John Wiley and Sons.

where the functionality of each transition metal is included. While the transition metals reside in the 3a layer, the Li⁺ resides in the 3b layer (“Li⁺ layer”), which provides the slab space for the 2D Li⁺ pathway.^[219] The changes in Coulombic interactions during charge within the crystal are intertwined with changes in the c-axis, thus the Li⁺ interlayer distances, which consequently affect Li⁺ mobility and in turn the SOC dependent overpotential.^[22–26] In addition, a phase transformation, which occurs depending on the SOC in NCM, has to be considered, as demonstrated in detail in section Phase-Transformation and Conversion-Type Electrodes. Thereby, the dependence of the cathode overpotential $\Delta\phi_{AM}^c$ on the SOC—and thus also the presence of the different phases H2 and H3—is shown in Figure 2c,d. Obviously, these parameters, which affect the Li⁺ mobility within the CAM, are the key parameters for the internal resistance, thus for the CAM’s fast-charging capability.^[22]

The related Li⁺ chemical diffusion coefficient (\tilde{D}_{Li^+}) is a crucial indicator for the evaluation of CAMs for fast-charging applications.^[22] For example, layered sulfide-based CAMs with high \tilde{D}_{Li^+} , for example, LiTiS₂ ($\tilde{D}_{Li^+} = 10^{-8} \text{ cm}^2 \text{ s}^{-1}$), also reveal superior rate performance.^[220] The same relation can be also observed for layered oxides, where LCO reveals the highest \tilde{D}_{Li^+} ($\tilde{D}_{Li^+} = 10^{-9} \text{ cm}^2 \text{ s}^{-1}$) and best rate performance among this structure type of CAMs.^[22,23] For NCM811, \tilde{D}_{Li^+} can reach $10^{-9} \text{ cm}^2 \text{ s}^{-1}$ at 50% SOC, while it is decreased for higher and lower lithiation degrees.^[221] The Li⁺ chemical diffusion coefficient can be improved, for example, by introducing concentration gradients of Ni, Mn, or Co in the NCM or NCA particles. For gradients of Ni and Co in NCM523 (LiNi_{0.5}Co_{0.2}Mn_{0.3}O₂), \tilde{D}_{Li^+} was increased by one order of magnitude.^[222,223]

Recently, single-crystalline CAMs have been actively investigated since they can offer improved cycling stability compared to polycrystal-based secondary particles.^[221,224,225] The increased particle size in the case of single crystals leads to significantly longer diffusion paths within the primary particles, however, decreasing the fast-charging capability of single crystals initially. During the lifetime of the battery cell, polycrystalline particles decompose faster, though, resulting in faster kinetics for single crystals after prolonged cycling.^[225]

4.1.2. Surface Modification of Cathode Active Materials

In addition to the research on NCM cathode materials, a whole range of studies have attempted to meet the demand for fast-charging cathode materials either by modification of already-reported cathodes^[223,226–234] or by the synthesis of new cathode materials.^[235–238] The most common technique for modifying conventional cathode materials for fast-charging applications is through surface modifications. By changing the surface environment, researchers were able to enhance the Li⁺ ion (charge) transfer during cycling and to get higher capacities during operation at high rates.^[223,226–234]

LCO, one of the most commonly used cathode materials in rechargeable batteries used for portable electronics, has been the subject of such surface modification. Yasuhara et al., following previous research by Teranishi et al., were able to significantly improve the cyclability and high-rate chargeability of LCO cathode thin films by supporting them with ferroelectric BaTiO₃ nanodots.^[226,227] The decoration of the cathode material surface

with BaTiO₃ nanodots, which have a thickness of less than 3 nm, diameter of 35 nm, and less than 5% coverage, creates what the authors refer to as a “triple-phase interface” (TPI) (cathode–nanodots–electrolyte). This interface presumably enhances the Li⁺ intercalation/deintercalation in its vicinity due to the formation of an “electric field concentration” by the high dielectric constant material BaTiO₃. Using this approach, the authors were able to obtain impressive capacity retention of more than 90% of the first cycle after 800 cycles at 5C. In a subsequent study, the group was able to determine a similar permittivity of the dielectric layer and the electrolyte as the underlying reason for improved charge transfer.^[239] Analyzing bare LCO, LCO decorated with TiO₂, and LCO decorated with BaTiO₃, all resulting in different permittivity of the dielectric surface layer, in combination with electrolytes based on DMC (low permittivity) and EC:DEC (high permittivity), the authors found a correlation between the capacity retention at high charging rates (10C) and the dielectric constant of the dielectric layer. For DMC, the bare LCO surface exhibiting the lowest permittivity showed improved capacity retention. In the case of EC:DEC, the behavior was reversed, with BaTiO₃ (high dielectric constant) resulting in the highest capacity retention. This was explained with improved adsorption and desolvation on the dielectric layer compared to the bare LCO. For similar permittivity of dielectric and solvent, desolvation of Li⁺ preferentially occurs at the dielectric surface, followed by diffusion to the TPI and transfer to the electrode. Thereby, even cycling at 50C was enabled.^[239]

Another recent attempt at modifying the surface of LCO cathode material was reported by Wang et al.^[228] In this study, the authors coated the LCO cathode material with Li_{1.6}Mg_{1.6}Sn_{2.8}O₈ showing a double-layer structure, which has similar oxygen packing to that of LCO and is inactive in the voltage window of the cathode. The Li_{1.6}Mg_{1.6}Sn_{2.8}O₈ coating was formed in situ on the surface of cathode particles using the reaction between SnO₂ and Mg-doped LCO. The coating improved the stability of the cathode surface by serving as a protective layer and increased the electronic conductivity by oxidizing some of the Co³⁺ in the pristine LCO and formation of mixing valence of Co³⁺/Co⁴⁺. The coated LCO exhibited better capacity retention than its uncoated counterpart under high-rate cycling and retained a capacity of 175 mA h g⁻¹ at 10C (upper cutoff potential 4.5 V).

One frequently used cathode material that has been subjected to various surface modifications for the purpose of achieving superior rate performance is spinel-structured LNMO. MgF₂, ZrO₂, SiO₂, and V₂O₅ coatings have been proven to be beneficial for the rate capability and cycling stability of LNMO.^[229–232] Wu et al. showed by analyzing dQ/dV plots that MgF₂ coating of LNMO reduces the electrode polarization. This phenomenon, in their opinion, may explain the observed facilitation of ion transfer through the cathode–electrolyte interface. Their calculations of the apparent chemical diffusion coefficient agree with their dQ/dV analysis and suggested that the coated cathode has better kinetic properties than the uncoated one.

4.1.3. Effects of Morphology

Morphology or “dimension” modification is another common approach to improve the high-rate performance of well-known

cathode materials. For example, LiV₃O₈ cathode material has shown better high-rate capabilities with the morphology of nanowires and nanorods compared to the conventional nanoparticle cathode structure.^[233,234] Xu et al. synthesized LiV₃O₈ nanorods with a diameter of (0.5–1.0) μm and a length of (4–8) μm using the nonionic triblock surfactant Pluronic-F127 as a structure directing agent. The nanorod structure of the particles of the cathode assisted in having faster kinetics of Li⁺ ion transfer that result in a better rate performance and cycling stability compared to particles with the nanoparticles structure. Thanks to that, the LiV₃O₈ nanorods exhibited a capacity of 138.4 mA h g⁻¹ at high current density of 6.4 A g⁻¹ (≈21C). Also, common NCM cathode material can be improved for better operation at high rates when using a nanorod structure.^[223] Noh et al. prepared NCM with a full concentration gradient of Ni and Co within the rod-shaped particles, while the Mn concentration was kept constant throughout. Thus, the Li⁺ chemical diffusion coefficient could be increased by one order of magnitude compared to conventional NCM523, improving the discharge capacity from 136 to 155 mA h g⁻¹ at 5C. Similar experiments were performed on NCA.^[222] Introducing concentration gradients of Ni and Mn in the material also led to rod-shaped primary particles, improving the reversible capacity and capacity retention.

4.1.4. Development of New Cathode Active Materials

Another recent strategy to obtain Li-ion batteries that are suitable for fast-charging is the development of novel organic cathode materials, with the advantages of being transition metal free and mechanically flexible.^[235] In a recent study, Otteny et al. demonstrated that factors such as the polymer structure, the amount of π-interactions between redox-active groups, and the morphology of the composite electrode have a significant impact on the rate capability and cycling performances of phenothiazine-based polymers.^[236] Their study shows that directly linked poly(3-norbornylphenothiazine) cathode material, with a redox potential of 3.5 V versus Li⁺/Li, had good cycling stability and rate capability. It reached a maximum specific capacity of 64 mA h g⁻¹ after 850 cycles at 100C rate, and retained 73% (47 mA h g⁻¹) of this capacity after 10 000 cycles, which is 55% of the theoretical value. The same group reported a cross-linked phenoxazine poly(vinylene) as cathode active material. This organic CAM has a high discharge potential of 3.52 V versus Li⁺/Li.^[237] After 10 000 cycles at 100C rate, a capacity of 70 mA h g⁻¹ was still obtained (74% of the first discharge capacity at 100C and 58% of the theoretical value).

Conductive metal-organic frameworks (MOFs) with redox metal centers are another class of materials that have been considered as potential cathode materials and might be suitable for fast-charging capabilities.^[235] Gu et al. investigated the MOF Cu₃(2,3,6,7,10,11-hexahydroxytriphenylene)₂ as a cathode material for Li-ion batteries.^[238] This MOF, with the Cu²⁺/Cu⁺ redox center responsible for the Li⁺ ion accommodation between the layers, has intrinsically high electrical conductivity and exhibits an open porous layered framework that makes it efficient for Li⁺ ion transfer during cycling at high rates. At a rate of 20C, the MOF cathode had a capacity of 85 mA h g⁻¹ after 500 cycles with capacity retention of 85%.

4.2. Limitation of Fast Charging on Electrode Level

While e^- transport proceeds mainly through the CAM and the conductive carbon toward/from the Al current collector,^[240] Li^+ transport pathways are more complex and proceed through the bulk electrolyte, the electrolyte-soaked composite electrode, the CEI, and CAM including intertwined charge-transfer processes as shown in Figure 10.^[22] The rating of each aspect according to its relevance and significance for the total internal resistance, thus for the fast-charging capability, is discussed as follows.^[22]

A relevant contribution of the e^- pathway to the cell resistance can rather be excluded.^[22,23,241] The intrinsic electronic conductivity of common layered oxide based CAMs like NCM is between (10^{-3} and 10^{-5}) $S\ cm^{-1}$, which depends on the SOC under normal operation and composition of the transition metals.^[23,242] After the addition of already small concentrations ($w = 1\%$) of conductive agent, for example, conductive carbon, the electronic conductivity of the cathode composite increases up to $10^{-1}\ S\ cm^{-1}$, which is two orders of magnitude higher than the ionic conductivity of common organic solvent based electrolytes, thus sufficiently high.^[21,22,243,244] The relevance of the electrolyte conductivity on internal resistance and fast charge aspects will be discussed in Section 5.^[22] An insightful additional proof for the negligible kinetic limitation due to electronic conductivity is the well-known example of the addition of Co to $LiNiO_2$, thus the formation of $LiNi_{0.8}Co_{0.2}O_2$.^[23] Even though the electronic conductivity of the resulting material decreases by an order of magnitude, the rate performance increases and demonstrates that other factors are relevant for fast charging, which will be discussed in the next sections.^[23,245]

According to literature, the impact of the cathode composite characteristics (e.g., porosity, mass fraction of inactive materials, mass loading, etc.) on the Li^+ transport is not as important as it is for anodes.^[21,22] The porosity as a crucial parameter for the density of Li^+ pathways within composite electrodes is minimized via calendaring for reasons of improved mechanical and energy density aspects.^[246]

Despite calendaring, rate performance is only affected for porosity values below 20%, and this only if combined with high CAM loading $> 30\ mg\ cm^{-2}$ (roughly corresponding to $> 5\ mA\ h\ cm^{-2}$). This combination of electrode properties is, however, far from application.^[21,212,247] Moreover, the inactive materials can theoretically have an impact on Li^+ transport and be kinetically problematic, but only below a conductive carbon to binder ratio of 0.6:1 and at inactive material mass loadings greater than 5% (relative to the active material amount), which is both not the case in present LIBs.^[243]

Finally, aspects related to Li^+ transport within a CAM, for example, material, particle size, particle morphology, etc., should also be of particular focus for fast charging. It is speculated that the crystal structure and associated Li^+ diffusion may be stressed in the course of fast charging via inhomogeneous delithiation and accompanied phase changes.^[248] These inhomogeneities can lead to secondary and primary particle cracking with an undesired raise of CAM surface, that is, electrolyte contact, which can affect the internal resistance and the fast-charging behavior,^[249] as will be discussed in Section 5. Crack formation increases with the SOC, the Ni content, and, just like for anodes,^[142] the size of the secondary particles.^[250]

It should be also noted that fast charging may also have a beneficial effect on cathode stability as it counteracts undesired crystal-intrinsic decomposition by a shorter time for the thermodynamic-driven phase changes of layered oxides at higher SOC. As shown in Figure 13a for NCM111, when charged to equal SOC (e.g., an 85% Li^+ extraction ratio), the specific capacity losses are lower after faster charge. A similar relation can be deduced for the charge/discharge cycling performance of NCM111, as shown in Figure 13b. The CAM obviously remains more stable during faster charge than during slower charge and this considerably affects the subsequent cycling performance, when again, equal charge conditions are used. As shown in Figure 13b, the specific charge current variation in the initial three cycles has a significant impact on subsequent cycle life under high-voltage conditions.^[251]

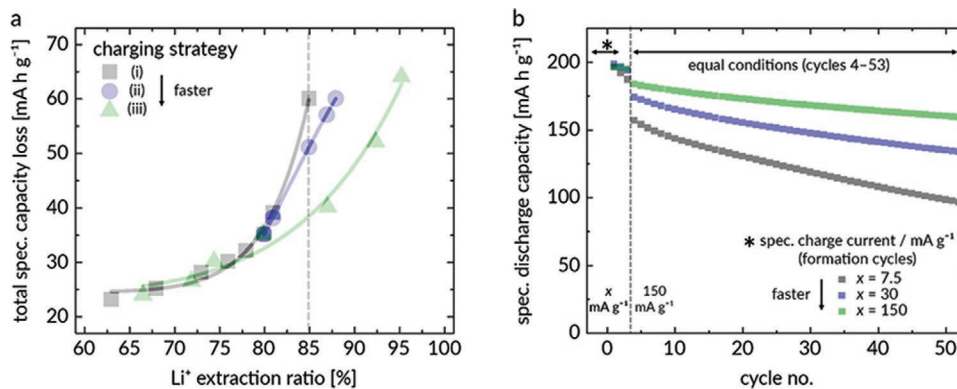


Figure 13. a) Specific capacity losses of the initial charge/discharge cycle versus the Li^+ extraction ratio of NCM111. The faster the charge, the lower the specific capacity loss. Adapted with permission.^[22] Copyright 2016, IOP Publishing. b) Specific discharge capacities as a function of cycle number of NCM111, with three formation cycles followed by charge/discharge cycling at $150\ mA\ g^{-1}$ ($\approx 1C$). The variation of the specific charge current only in the formation cycles has a significant influence on the subsequent cycling performed under equal conditions, that is, fast charge during formation leads to better performance. Adapted with permission.^[251] Copyright 2017, Elsevier.

5. Electrolyte

5.1. Liquid Electrolytes

Among the different electrolyte systems currently under consideration for LIBs, liquid organic solvent based electrolytes show a most favorable combination of cost and performance properties.^[252] The (total) ionic conductivities of state-of-the-art liquid electrolytes, that is, 1.0 mol L⁻¹ LiPF₆ in a solvent mixture based on EC and linear carbonates like DMC, DEC, and/or ethyl methyl carbonate (EMC) reach values of up to 10⁻² S cm⁻¹ at room temperature (RT).^[253] While t_{Li^+} typically is only between 0.2 and 0.4,^[253] resulting in an Li⁺ conductivity of less than half of the total conductivity, these values are more than sufficient for LIB application at RT and below. Even decreasing the concentration down to 0.2 mol L⁻¹ LiPF₆, the ionic conductivity is still 3 mS cm⁻¹.^[244] As shown in **Figure 14a** for NCM111, no changes in charge/discharge behavior can be deduced for different salt concentrations, also at faster charge conditions. The charge profiles remain similar, that is, without additional overpotentials at lower salt concentration, which demonstrates that not the bulk ionic conductivity of the electrolyte within the separator but rather other cell parameters are rate-determining, as discussed in Sections 3 and 4.

However, at the anode side, transport in the electrolyte is considered the rate-limiting step, as already overpotentials < 100 mV induce lithium plating. Such overpotentials are easily achieved if the current density approaches j_{lim} . Gallagher et al. observed cell failure of NCM622/graphite full cells due to lithium plating at currents > 1C for approximately the targeted capacity of 3.3 mA h cm⁻² and an N/P ratio of around 1.2 (**Figure 15a**).^[151] Based on Equation (38), we calculated j_{lim} for such cells, assuming an ion transference number of 0.4, lithium-ion concentration of 1 mol L⁻¹, separator—and thus electrolyte—thickness of 30 μm and diffusion coefficients in the range (1–5) × 10⁻⁶ cm² s⁻¹, which represents the typical range for diffusion coefficients of concentrated lithium electrolytes.

If the porosity is between 30% and 40% (typical values), β would be 5–10 for realistic electrodes.^[47] Therefore, according to **Figure 15b**, the target current density of 12 mA cm⁻² (4C) would be around the limiting current. We note that according to Equation (40) the overpotential is quite substantial even below the limiting current. Therefore, although 4C charging would be possible, the high overpotential would result in lithium plating at the anode.

The reason behind this is that although high currents are possible, the reaction becomes confined at those parts of the electrodes that are easily accessed by the electrolyte (i.e., close to the separator). The lithium-ion concentration in the electrolyte of those electrode regions, which are hardly accessed by the electrolyte (i.e., close to the current collector) is depleted.^[152] This confinement of the reaction leads to a substantial local potential drop. Therefore, growth of lithium dendrites is mostly observed originating from the tip of the graphite electrode. Hence, we assume that lithium plating as a result of reaction confinement in the anode is the rate-limiting step in practical battery full cells. A strategy to overcome such issue would, for example, involve a higher lithium diffusion coefficient (or also lithium-ion transference number) as this lifts the limiting current density significantly. Such issue can also be circumvented by increasing the temperature during cell charging. Another possibility is the application of a porous layer in contact to the electrode, of which the surface is functionalized with groups exhibiting high Li⁺ affinity. Thus, the concentration of Li⁺ within the pores is increased, reducing concentration polarization in the electrolyte. Additionally, electrokinetic effects, such as electroosmosis and surface conduction, enhance Li⁺ transport within the pores, significantly increasing the limiting current density, which enables cycling at higher rates.^[254]

Besides ionic conduction in the bulk, the electrolyte may impact the internal resistance of the cell also in other ways, in particular via charge-transfer processes at the interfaces as detailed in Section 2.1.2. It is known from the anode side that the intercalation of Li⁺ into, for example, graphite during the

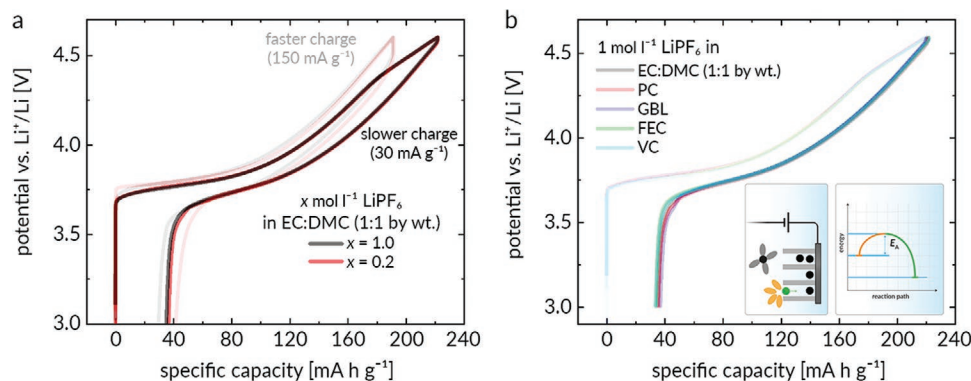


Figure 14. a) Initial charge/discharge cycle of NCM111 at different specific currents using an electrolyte with a conventional Li salt concentration (1.0 mol L⁻¹), and a decreased Li salt concentration (0.2 mol L⁻¹), thus decreased ionic conductivity. The charge profile is similar for both Li salt concentrations, even for elevated specific currents, which points to a rather insignificant impact of the electrolyte bulk ionic conductivity on internal cell resistances. b) Initial charge/discharge cycle of an NCM111 electrode using LiPF₆ in various solvents and solvent mixtures. A possible solvent impact on the charge performance, that is, delithiation kinetics, cannot be noticed. The impact of the cation desolvation process on performance, at least for the used cathodes, appears also negligible as the discharge curves behave similar. Still, any effect of kinetically hindered desolvation should not be disregarded during charge of anodes. Adapted with permission.^[22] Copyright 2016, IOP Publishing.

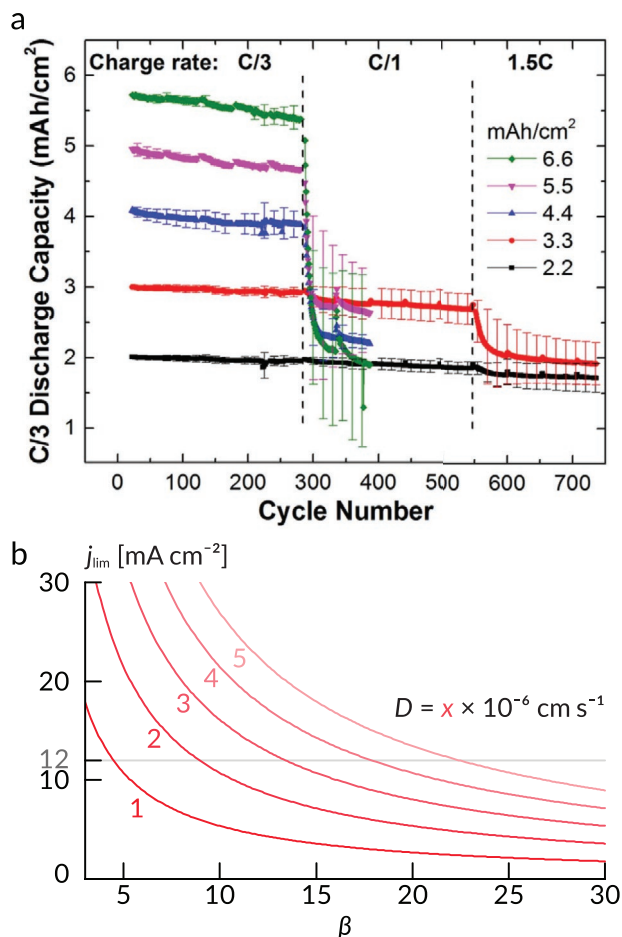


Figure 15. a) Capacity of NCM622/graphite full cells with different loading of active material (N/P ratio of around 1.2). Upon increasing charge rate, cells with high loading fail as a result of lithium plating. Reproduced under the terms of the CC BY-NC-ND 4.0 license.^[151] Copyright 2016, The Authors. Published by IOP Publishing, Ltd. b) Diffusion-limited current density j_{lim} as a function of the electrode structure (parameter β) and with different chemical diffusion coefficients calculated from Equation (38) based on the experimental parameters of the cells shown in (a).

charge process requires Li^+ desolvation from the solvent shell, which is regarded as a rate-determining process during charge (see Section Barriers for Migration of Li^+ Ions from Electrolyte into Anode Active Materials).^[78,255] In the typically used carbonate solvent based electrolyte mixtures, naturally the highly polar EC is the preferable solvating solvent component. Moreover, given its large activation energy (E_A) values, the Li^+ desolvation process is also assumed to contribute to internal resistances of the cathode, though in this case in the discharge process.^[75,77,256] These conclusions are drawn from theoretical considerations.^[257] It is claimed, that the kinetics of Li^+ desolvation sensitively depends on the coordination strength of Li^+ with the respective solvent molecules constituting the solvent shell.^[258]

To check this claim under practical experimental conditions, LiPF_6 dissolved in various solvents including γ -butyrolactone (GBL), propylene carbonate (PC), fluoroethylene carbonate (FEC), and vinylene carbonate (VC) was investigated with respect to overpotentials on the cathode side.^[22] The discharge curves display similar shapes for all electrolytes as shown in

Figure 14b. In addition, also any solvation effects during charge on the kinetics can also be excluded on cell level as also the charge profile behaves similar for all investigated solvents.^[22] The salt, however, can have an influence on charge transfer as a recent study indicates.^[259] Thereby, the addition of lithium bis(trifluoromethanesulfonyl imide) (LiTFSI) to LiPF_6 in DMC electrolyte increased the cathode exchange current density by about two orders of magnitude. Thus, the charge-transfer resistance was decreased to 6% of its value without LiTFSI . Using molecular dynamics simulations, the TFSI^- anions were found to preferentially solvate Li^+ , which—combined with the lower binding energy to the Li^+ ion—enables faster interface kinetics.^[259] Thus, different conducting salts next to (or in combination with) conventional LiPF_6 are worth investigating.

Finally, the impact of the electrolyte at electrode|electrolyte interfaces in LIB cells will be discussed.^[22,260] On graphite-based anodes, the electrolyte electrochemically decomposes and forms a protective layer, the SEI.^[261] Its chemical composition and thickness significantly contribute to the internal resistances, which thus can be significantly tailored via reasonable electrolyte formulation, for example, via electrolyte additives.^[246,262] For graphite anodes with LiPF_6 in a mixture of EC, EMC, and methyl propionate (MP), the addition of lithium bis(fluorosulfonyl)imide (LiFSI) reduced the charge-transfer resistance and activation barrier of the SEI compared to the pure solvent mixture, for example.^[263] Another method is changing the solvent. A recent study used 1,4-dioxane, which is only weakly solvating while still retaining sufficient solubility for the LiFSI conducting salt. Thereby, ion pairs prevail even at low salt concentration leading to a mainly inorganic SEI, which offers fast interfacial charge transfer and high stability, improving the fast-charging capability.^[264]

In contrast, the CEI, particularly on commonly used layered oxide based cathodes (e.g., NCM, NCA, LCO)^[265] considerably differs from the SEI. Organic carbonate-based electrolytes are more oxidatively stable than commonly believed^[215,216,251,265–269] However, the CEI composition and behavior on the cathode is affected by the so-called “native” cathode surface, which exists prior to application in form of Li_2CO_3 and/or LiOH .^[216,217,253,266–270] Alteration of the CEI can already proceed after simple electrolyte contact, particularly at elevated temperatures, thus in a chemical manner, in addition to CEI formation by electrochemical oxidation of instable electrolyte components.^[271,272] As mentioned in Section 4, Li^+ transport within the CAM is the rate-limiting step in/at the cathode. Nevertheless, the impact of the CEI on performance can get significant during cycle and calendar life in the course of aging and can be tailored via the electrolyte.^[272]

5.2. Inorganic Solid-State Electrolytes

Solid electrolytes behave quite different compared to liquid electrolytes when it comes to fast charging. As typical polymer electrolytes show relatively low lithium-ion conductivity, they are hardly suited for fast-charging applications and we focus on inorganic solid electrolytes (ISEs) in this section. Typically, ISEs exhibit single-ion conduction, due to the rigidity of the anion polyhedron framework. Thus, lithium transference numbers are almost equal to unity, assuming electronic charge

transport can be neglected. Although the ionic conductivity of most ISEs is lower than the total ionic conductivity of liquid electrolytes (10 mS cm^{-1}), their single ion conducting character makes them competitive. The conductivity of a specific charge carrier is obtained by the product of the respective transference number and the total conductivity. Assuming a transference number of $t_{\text{Li}} = 0.4$, the lithium-ion conductivity of liquid electrolytes amounts to about 4 mS cm^{-1} . This value has already been achieved and even surpassed by several ISEs, such as $\text{Li}_{9.54}\text{Si}_{1.74}\text{P}_{1.44}\text{S}_{11.7}\text{Cl}_{0.3}$,^[68] $\text{Li}_{6.6}\text{P}_{0.4}\text{Ge}_{0.6}\text{S}_5\text{I}$,^[273] and $\text{Li}_{6.6}\text{Si}_{0.6}\text{Sb}_{0.4}\text{S}_5\text{I}$.^[274] Complementary to a higher single-ion conductivity, no concentration polarization effects are observed in inorganic solid electrolytes (compare Section 2.2.2). At high current densities, which are a necessity to enable fast charging, the contribution of the overpotential $\Delta\varphi_{\text{EL}}$ that originates in the motion of ions in the solid-state electrolyte follows Ohms law, that is, Equation (42).

Superionic solid electrolytes show no anion migration and typically have very high charge carrier concentrations, which leads to a deviation from the Nernst–Einstein equation. The migration of the lithium ions takes place simultaneously throughout the whole material. This can also be described in terms of cooperative transport processes.^[275] Inorganic solid electrolytes are either ceramics, glasses, or glass-ceramics, which makes them much more stable at higher temperatures than liquid electrolytes based on carbonates and other organic solvents. This is a key advantage, as higher operating temperatures can be achieved.

The ionic motion in solid electrolytes is based on the migration of lithium ions through empty lattice sites (vacancies) or interstitial sites. In ceramic solid electrolytes, these lattice sites are usually either tetrahedrally or octahedrally coordinated. For this migration, an activation energy has to be provided, to overcome the binding energies of the stable ground state. Consequently, the ionic conductivity follows an Arrhenius-like behavior, resulting in an increased ionic conductivity at higher temperatures. Fast charging of Li-based solid-state batteries can thus be accelerated by an increased temperature during charging. Typically, Joule heating already increases the temperature within an LIB if high current densities are provided.^[276] To avoid uncontrolled decomposition and evaporation of the liquid electrolyte, advanced cooling systems have to be employed, decreasing the specific energy and power density. These cooling systems might be omitted in solid-state systems, because the increasing temperature may not only be not harmful, but it may further accelerate the charging, due to increased ionic conductivity of the solid electrolyte. Overpotentials originating from the solid electrolyte itself can, therefore, easily be reduced to a bare minimum. Kato et al. reported by using a superionic conductor that SSB cells could be cycled at temperatures as high as $100 \text{ }^\circ\text{C}$ repeatedly, as is depicted in **Figure 16**. Additionally, discharge rates of up to 1500C (discharging in 2.4 s) were demonstrated.^[68] Although the experiments were conducted at $100 \text{ }^\circ\text{C}$ and only showed the high discharge capability, they also demonstrated that extremely high current densities (1 A cm^{-2}) are enabled by ISEs.

Additionally, solid electrolytes do not suffer from low temperature phase transitions, which might result in the solidification

of liquid electrolytes. Choi et al. could show that even at the deep freezing conditions of $-30 \text{ }^\circ\text{C}$, thiophosphate-based solid electrolytes can provide sufficient ionic conductivity to operate an SSB cell.^[277]

5.2.1. Solid Electrolytes in Composite Cathodes

On the cathode side, the charge-transfer resistance between, for example, NCM and SEs is a problem, since it is increased compared to LEs by one order of magnitude.^[48] This is a result of irreversible degradation reactions at the interface between CAM and SE (CEI formation).^[48,278] Another disadvantage of solid electrolytes is their rigidity, resulting in decreased contact between active materials and solid electrolytes. While liquid electrolytes can easily infiltrate the porous composite cathodes, particularly ISEs do not exhibit a “wetting” behavior of the CAM surface.^[48] This makes, for instance, processing quite challenging, as good interfacial contact is a necessity to reduce interfacial overpotentials. Not only the charge-transfer resistance will be influenced, but also the diffusion within the cathode active material itself becomes limiting, as extraction of lithium ions can only take place at a few contact points. This behavior most likely becomes even worse over the course of cycling. Cracking of the active material can be caused by electro-chemo-mechanical stresses.^[279] Reasons can be gradients in lattice parameters due to different Li-ion concentrations in the bulk and at the surface of the cathode active materials. While a liquid electrolyte can penetrate the newly formed cracks and, thus, further decrease ionic diffusion lengths, a solid electrolyte cannot do the same.^[221] It may hence be necessary to inhibit cracking of the cathode active material, for instance by transitioning from secondary particles to single crystals, especially when aiming for high Ni compounds. Another factor influencing the fast-charging behavior of solid-state composite cathodes is the microstructure of the cathode. As mentioned above, a liquid electrolyte can easily penetrate pores of the cathodes. Here, the viscosity of the liquid as well as the wetting angle of the solid–liquid interface are important material properties. While these material properties may, within certain boundaries, be used in solid polymer electrolyte systems, they do not apply to ISE systems. Here, good mixing of the powders is essential to achieve sufficient charge transport pathways.

In an ideal microstructure, both, ionic and electronic pathways, are percolating throughout the whole composite cathode. This means that tortuosity factors, which correlate volume fractions and bulk conductivities of the participating components to the effective total conductivity, are as low as possible. Numerous studies have targeted the microstructure of solid-state composite cathodes.^[280] Kaiser et al. used electrochemical as well as tomographic methods to investigate the ionic charge transport within thiophosphate-based composite cathodes. They found that composition of the composite cathode plays a central role for total ionic conductivities and will thus strongly influence the fast-charging behavior of SSBs.^[281,282] Recently, Shi et al. determined that the ratio between ISE particle size and CAM particle size is crucial for an improved rate performance.^[283] In general, it

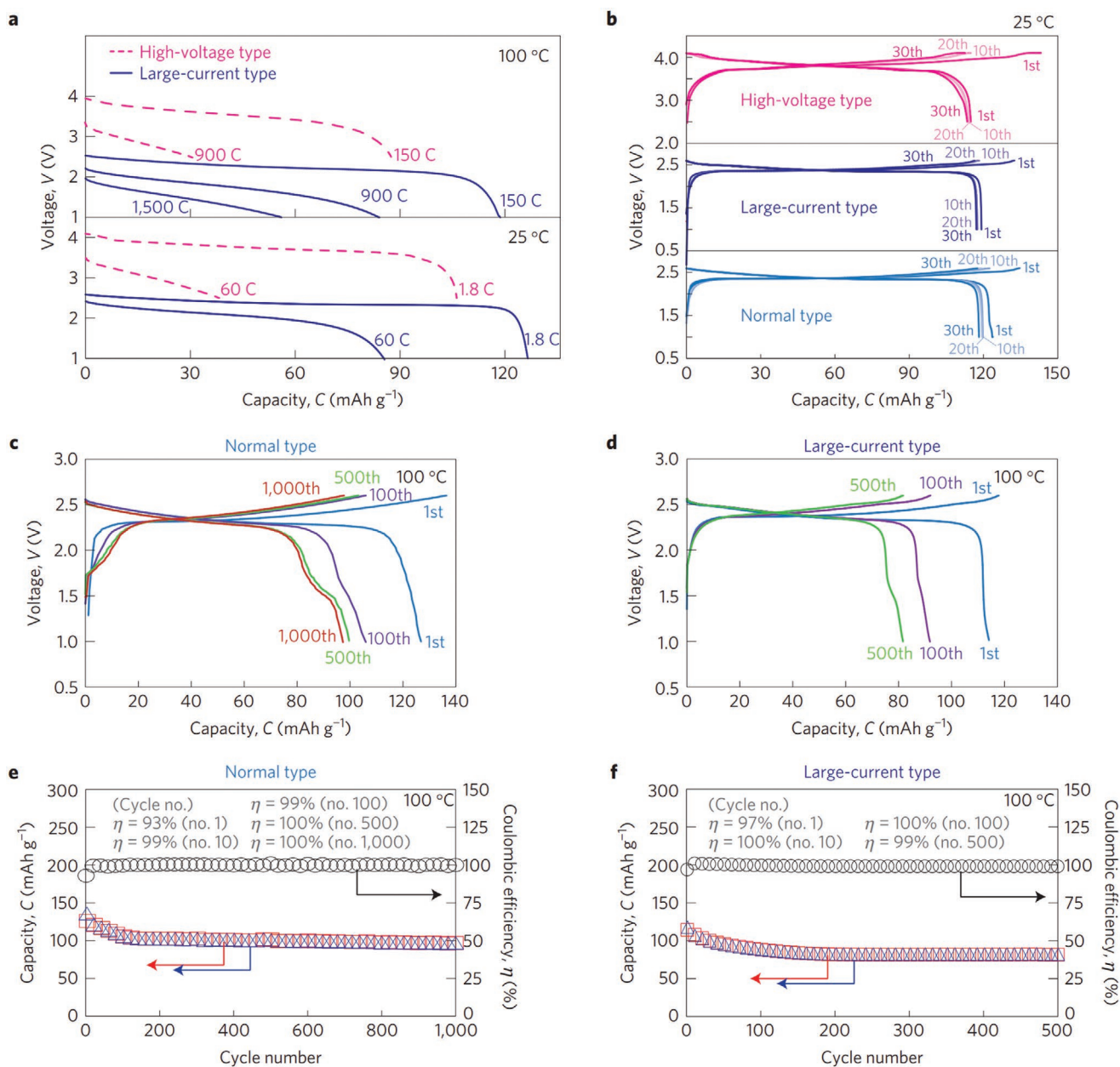


Figure 16. Solid-state battery performance at 100 °C. The high temperature increases the ionic conductivity without increasing safety hazards. C-rates of 1500C have been demonstrated, enabled by a superior temperature stability at 100 °C (discharge in 2.4 s). a) Comparison of discharge curves at (25 and 100) °C. b) Charge and discharge curves at 0.1C and 25 °C. Charge and discharge curves at 18C and 100 °C for c) normal-type and d) large current type cells. Development of Coulombic efficiency (black) as well as discharge (red) and charge (blue) capacity at 100 °C as a function of cycle number for e) normal-type and f) large current type cells, respectively. Reproduced with permission.^[68] Copyright 2016, Springer Nature.

can be assumed that the ionic tortuosity of SE-based composite cathodes is higher than in LE-based ones.^[16,282,284] As a consequence, the ionic conductivity of the solid electrolyte needs to be higher than that of the liquid electrolyte. **Figure 17** displays that ionic conductivities of more than 10 mS cm⁻¹ are necessary for fast charging a simulated solid-state cathode with a tortuosity of $\tau = 2$ and an active material content of $\varphi = 70\%$.^[71]

Clearly, high ionic conductivities of more than 10 mS cm⁻¹ are necessary in order to achieve high rates (>4C) and

simultaneously high energy densities, meaning thick cathodes and high-power densities, meaning low overpotentials. Recently, Minnmann et al. reported high tortuosity factors for both ionic and electronic conduction in thiophosphate/NCM based cathode composites, demonstrating that the effective ionic conductivity in cathode composites can be much lower than the bulk electrolyte conductivity.^[70] It is, therefore, crucial to improve the tortuosity of solid-state cathodes as well as to increase the (bulk) ionic conductivity.

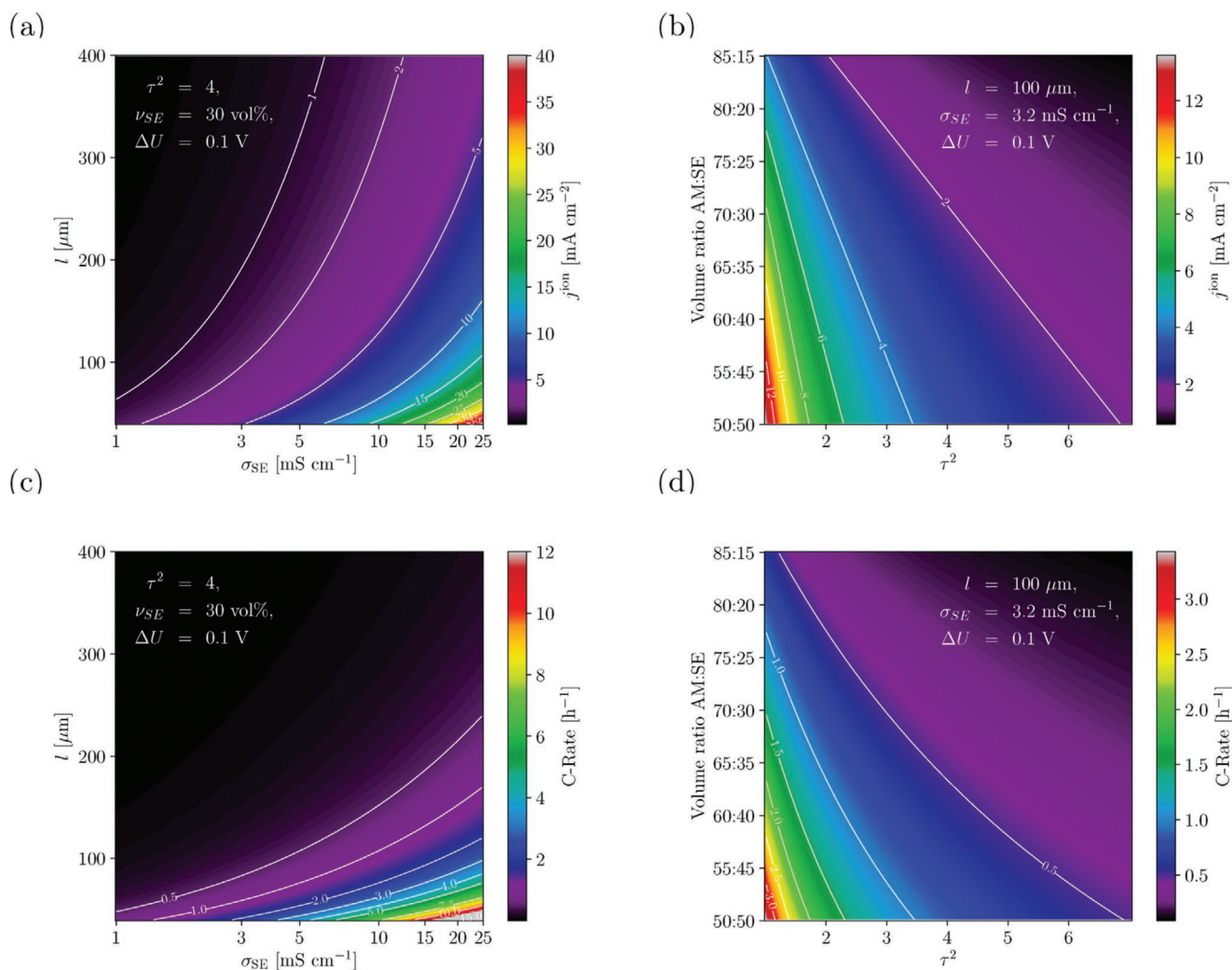


Figure 17. Simulated areas of fast-charging capability for thiophosphate-based composite cathodes with a,c) varying thickness and ISE conductivity as well as b,d) CAM volume fractions and tortuosity factors. The colors represent the area of a certain current density (a, b) and C-rate (c, d), respectively. For the fast-charging capability, a maximum allowed overpotential of 100 mV is assumed. Reproduced with permission.^[7] Copyright 2020, American Chemical Society.

5.2.2. Contact between Solid Electrolytes and Anodes

Fast charging requires the implementation of an anode material with low charge-transfer resistance and, ideally, no diffusion limitation. Typically, LMAs are considered as the most desired concept, as they provide the highest energy and power density that can be achieved. Recently, Krauskopf et al. could demonstrate that the interfacial charge-transfer resistance between an LMA and the solid electrolyte $\text{Li}_{6.25}\text{Al}_{0.25}\text{La}_3\text{Zr}_2\text{O}_{12}$ (LLZO) is negligible.^[285] This would make LMAs also favorable for fast charging, as the charge-transfer overpotentials will be minimal and no incorporation into a host material is necessary. However, LMAs have several other issues that need to be overcome. Contrary to a liquid electrolyte, it is necessary to provide and maintain a good mechanical contact between the solid electrolyte and the LMA. It is evident that decreasing contact area will increase the area specific resistance (ASR) of the cell ultimately influencing the overpotential. Because ISEs are typically (sintered) powders, a certain roughness toward the LMA will

always remain. It is, thus, essential to achieve a good uniform contact by plastic deformation of either the ISE, the LMA, or both. Additionally, stack pressure becomes important in order to remain a good contact upon lithium removal and plating. However, Doux et al. reported that high stack pressures could also lead to mechanical failure of the cell, since lithium can creep through the solid electrolyte.^[286] The influence of stack pressure is not fully resolved yet and is still discussed. Influential factors, such as solid electrolyte morphology, mechanical properties, and thickness of the employed lithium metal anode have to be considered.

Fast charging means cathodic load. Hence, lithium is removed from the cathode and plated at the anode side. Ideally, this process produces a homogeneous and even surface. However, high current densities, which are a feature of fast charging, often result in inhomogeneous Li deposition and dendrite formation takes place. ISEs have the advantage to provide a “mechanical resistance” to dendrite growth, making Young’s modulus, fracture toughness, and shear modulus

important parameters. Recently, porous solid electrolytes were reported to show increased dendrite resistance by drastic reduction of the current density, which was caused by an increased contact area between lithium and ISE.^[287] Krauskopf et al. have published a detailed review on the physicochemical concept of lithium metal anodes, in which all major concepts are being discussed.^[90]

6. Limitation and Improvement of Fast Charging on Cell Level

Limited heat dissipation and conventional CC–CV charging hinders fast-charging applications on the cell level. The operating temperature strongly affects the energy, capacity, reliability, and durability of the batteries. High temperatures accelerate capacity degradation and shorten battery life.^[162,288] Various studies presented the (25–40) °C range as optimum temperature to achieve the best LIB performance.^[38,177,289] When high rates are required, efficient thermal management systems (TMS) are essential due to the massive heat produced, especially at high ambient temperatures.

Ye and coworkers performed numerical modeling predicting the temperature reached by a battery undergoing a charging process at 10C when thermal contact resistance is taken into consideration. When a liquid cold plate cooling system is applied in the simulation, the maximum battery temperature may reach 64.6, 38.2 °C higher than the case without thermal contact resistance.^[290] The transfer of Li⁺ ions across the activation energy barrier at the electrode interface results in a loss in the kinetic energy contributing to (30–40)% of the heat losses under practical operation conditions.^[291]

So far, three different categories of TMSs were studied, including air cooling, liquid cooling, and phase change materials (PCMs) cooling systems.^[292] Recently, advanced systems were developed in order to overcome the increasing need for high battery operation rates. Silica liquid cooling plates (SLCP) attached to both sides of a Li-ion battery were tested as a heat dissipation system for high-current systems. A various number of channels were investigated while applying different discharge C-rates. It was concluded that an increased number of channels manages to keep the maximum temperature inside the cell below 39.1 °C (Discharge rate of 3C and liquid flow rate of 0.1 m s⁻¹).^[293]

Furthermore, an innovative fast-charging Li-ion battery pack that combines both liquid cooling and PCM cooling has presented promising simulation results. The temperature of an 8C charging process was maintained at a maximum value below 40 °C. In this case, the PCM heat adsorption accounts for less than 10%, while the liquid cooling takes 80% of the general heat.^[294]

The extended charging time required for the Li-ion battery nowadays compromises their popularity in the automotive industry worldwide. A typical charging process is conducted using a constant current (CC) step followed by a constant voltage (CV) one.^[295] Lithium metal deposition on the anode surface is prone to occur when increasing the current applied during the fast-charging process due to the significant polarization formed on the electrode|electrolyte interface.^[7] Although

the time required to reach the cut-off voltage decreases while increasing the applied current, more time will be necessary to obtain the desired current value during the CV phase. Therefore, the charging time is not significantly reduced.^[296]

Innovative charging procedures such as pulsed or tapered current techniques were studied to decrease the concentration polarization.^[296–299] By doing so, better utilization of the active material along with shorter charging time and increased cell life can be achieved. Different charging models considering the ion concentration on the electrode surface alongside the degradation processes taking place during cycling have reduced the charging time by (60–70)% compared to the classical CC–CV charging technique.^[105,295,297]

Lu et al. presented a charging method that takes into consideration the stress induced in electrode particles by diffusion, which later on may result in mechanical failure and a considerable effect on the battery's electrochemical performance. An exponential current (EC) method where the charging process initiates in a maximum current density, followed by an exponential continuous decrease, avoiding any sudden changes, was found to prevent stress undulation in addition to acceleration of the charging process. Due to the direct connection between the stress evolution and the heat generated in the cell this method could also improve the battery's thermal performance.^[300]

The impact of different pulse charging protocols was evaluated in various studies while considering the electrolyte polarization, stress evolution, heat generation, and the battery cycle life.^[299,301] Most studies presented an improved battery performance, higher cycling number, and slower battery aging and degradation process than the conventional CC–CV charging method. Therefore, the charging protocol can significantly affect the overall battery performance, especially when a short charging period is required.

7. Conclusions

In this review, we focus on the issues hindering fast charging of today's LIBs from a physicochemical and materials' point of view. Complemented by an overview of studies analyzing different cells regarding their fast-charging ability, a detailed picture of the requirements for fast-charging enabling materials is drawn. Fast Li ion diffusivity in the active materials is identified as one of the major factors needed for fast charging. Improved anode materials should offer low barriers for migration into them as well as for diffusion within the material itself. Thus, lithium plating—a major obstacle observed on graphite anodes—can be reduced as well. Once diffusion is not fast enough, particle size becomes an important factor in enabling fast charging, partially able to counteract low lithium diffusivity. For active materials with strong diffusion anisotropy, like, for example, the layered compounds, the particle morphology becomes another important factor, and particle morphology control may lead to faster charging rates on the material level. This leads to the electrode level, where a particular microstructure with low tortuosity factors and optimized porosity balancing both, electronic and ionic conductivity, is needed.

For the cathode, a slightly different behavior is observed. While the characteristics of the cathode composite do have

a certain impact on the electrode's fast-charging ability, for application-relevant cathode composites their influence is small. Instead, the characteristics of the CAM itself were identified to greatly affect cathode overpotentials, in line with the varying Li^+ chemical diffusion coefficients and crystal structures of different CAMs. In addition, phase changes depending on SOC have to be considered, since state-of-the-art layered oxides like NCM undergo a phase transition with changing lithiation degree, for example.

Transport within the bulk liquid electrolyte was found to play a less important role in determining a given battery cell's fast-charging ability. Its ionic conductivity is high enough to not slow down lithium transport nearly as much as the electrodes. At those, specifically at the anode side, transport in the liquid electrolyte becomes rate-limiting, though. For typical electrode properties, the current density targeted for fast-charging applications is close to the limiting current density. This causes a high overpotential leading to lithium plating at the anode. In addition, the compatibility of the electrolyte with active materials is of interest, as degradation occurs on both, the anode and the cathode side, leading to SEI and CEI formation, respectively. Thereby, the SEI properties can be tuned by the electrolyte composition, allowing for optimization regarding low charge-transfer resistances. For solid electrolytes, the limited ionic conductivity—resulting from high tortuosity and contact issues—does become an issue, though. Therefore, also the microstructure of the cathode composite gets increasingly important when applying solid instead of liquid electrolytes. The increased thermal stability of SEs allows for operation at increased temperature, however, which greatly improves diffusion coefficients and reaction kinetics, mitigating the disadvantages of reduced ionic conductivity.

Yet, operation at higher temperatures does demand more intricate designs on cell level, which is shortly outlined in the final part of this review. Thermal management systems have to be applied for optimum heat dissipation to reduce degradation and elongate the battery lifetime. In addition, improvements to the charging protocol should be considered, since pulsed charging and stepwise reduction of the charging current was shown to exhibit benefits over the traditional CC–CV method, not only resulting in better performance but also reduced degradation.

We hope that, with the collected suggestions for improvements in fast-charging materials and the depicted comparison of advantages and disadvantages of existing materials, this review will spark new exciting research in this crucial field, possibly leading to widespread adoption of electric vehicles in the future.

Acknowledgements

The authors thank Joachim Sann (JLU) for fruitful discussions and Raimund Koerver (BMW AG), Dominik Weber (Volkswagen AG), and Andreas Fischer (BASF SE) for critical comments on the manuscript. Financial support is highly appreciated and acknowledged from the following entities and foundations: the German Federal Ministry for Education and Research (BMBF) within GIBS 4 bi-national workshop, ELONGATE (03XP0248), FestBatt (03XP0180), LiMetalFreeSSiBAT (03XP0141), and by the Federal Ministry for Economic Affairs and Energy (BMWi) within the Structur.e (03ETE018E) project, the Israeli Ministry of

Science and Technology (MOST), the Planning & Budgeting Committee/Israel Council for Higher Education (CHE), and Fuel Choice Initiative (Prime Minister Office) within the framework of "Israel National Research Center for Electrochemical Propulsion" (INREP 2) and by the Grand Technion Energy Program (GTEP).

Open access funding enabled and organized by Projekt DEAL.

Conflict of Interest

The authors declare no conflict of interest.

Keywords

cell degradation, fast-charging batteries, lithium chemical diffusion, lithium plating, lithium-ion batteries

Received: April 8, 2021

Revised: May 28, 2021

Published online: July 19, 2021

- [1] a) J. M. Tarascon, M. Armand, *Nature* **2001**, 414, 359; b) A. Yoshino, K. Sanechika, T. Nakajima (Asahi Kasei Corp), US 4668595, **1986**.
- [2] J. B. Goodenough, K.-S. Park, *J. Am. Chem. Soc.* **2013**, 135, 1167.
- [3] A. Eftekhari, *ACS Sustainable Chem. Eng.* **2019**, 7, 3684.
- [4] a) J. Janek, W. G. Zeier, *Nat. Energy* **2016**, 1, 16141; b) A. Manthiram, X. Yu, S. Wang, *Nat. Rev. Mater.* **2017**, 2, 16103.
- [5] H. J. Gores, J. Barthel, S. Zugmann, D. Moosbauer, M. Amereller, R. Hartl, A. Maurer, in *Handbook of Battery Materials* (Eds: C. Daniel, J. O. Besenhard), Wiley-VCH, Weinheim, Germany **2011**, pp. 525–626.
- [6] A. Adam, J. Wandt, E. Knobbe, G. Bauer, A. Kwade, *J. Electrochem. Soc.* **2020**, 167, 130503.
- [7] A. Tomaszewska, Z. Chu, X. Feng, S. O'Kane, X. Liu, J. Chen, C. Ji, E. Endler, R. Li, L. Liu, Y. Li, S. Zheng, S. Vetterlein, M. Gao, J. Du, M. Parkes, M. Ouyang, M. Marinescu, G. Offer, B. Wu, *eTransportation* **2019**, 1, 100011.
- [8] Y. Liu, Y. Zhu, Y. Cui, *Nat. Energy* **2019**, 4, 540.
- [9] P. Entwistle, B. Schaper, *Porsche Taycans use IONITY High-Power Charging Stations on International Media Ride and Drive Event, 2019*, http://ionity.eu/_Resources/Persistent/cffc5959e6c98afcbca7d0abe575502911a3b26c/20190911_IONITY_Posche_Taycan_EN.pdf (accessed: March 2021).
- [10] L. Ulrich, *IEEE Spectrum* **2020**, 57, 30.
- [11] C. Kim, A. Lennon, World Premiere of the Porsche Taycan: The Sports Car for a Sustainable Future. PR No. 73/19, **2019**, http://press.porsche.com/prod/presse_pag/PressResources.nsf/Content?ReadForm&languageversionid=1021391 (accessed: March 2021).
- [12] a) M. Holland, Supercharger V3. Shocking Power & Smart Strategy By Tesla (Charts!), cleantechnica.com/2019/03/08/supercharger-v3-shocking-power-smart-strategy-by-tesla-charts/ (accessed: November 2020); b) M. Holland, Tesla Model 3 On SuperCharger V3. Adds 50% Range In Under 12 Minutes! (Charts!), cleantechnica.com/2019/06/24/tesla-model-3-on-supercharger-v3-adds-50-range-in-under-12-minutes-charts/ (accessed: November 2020).
- [13] S. Ahmed, I. Bloom, A. N. Jansen, T. Tanim, E. J. Dufek, A. Pesaran, A. Burnham, R. B. Carlson, F. Dias, K. Hardy, M. Keyser, C. Kreuzer, A. Markel, A. Meintz, C. Michelbacher, M. Mohanpurkar, P. A. Nelson, D. C. Robertson, D. Scofield, M. Shirk, T. Stephens, R. Vijayagopal, J. Zhang, *J. Power Sources* **2017**, 367, 250.
- [14] K. Du, H. Xie, G. Hu, Z. Peng, Y. Cao, F. Yu, *ACS Appl. Mater. Interfaces* **2016**, 8, 17713.

- [15] a) J. Li, A. R. Cameron, H. Li, S. Glazier, D. Xiong, M. Chatzidakis, J. Allen, G. A. Botton, J. R. Dahn, *J. Electrochem. Soc.* **2017**, *164*, A1534; b) J. E. Harlow, X. Ma, J. Li, E. Logan, Y. Liu, N. Zhang, L. Ma, S. L. Glazier, M. M. E. Cormier, M. Genovese, S. Buteau, A. Cameron, J. E. Stark, J. R. Dahn, *J. Electrochem. Soc.* **2019**, *166*, A3031; c) Y. Liu, J. Harlow, J. Dahn, *J. Electrochem. Soc.* **2020**, *167*, 020512.
- [16] J. Landesfeind, J. Hattendorff, A. Ehrl, W. A. Wall, H. A. Gasteiger, *J. Electrochem. Soc.* **2016**, *163*, A1373.
- [17] S. Malifarge, B. Delobel, C. Delacourt, *J. Electrochem. Soc.* **2017**, *164*, E3329.
- [18] I. V. Thorat, D. E. Stephenson, N. A. Zacharias, K. Zaghbi, J. N. Harb, D. R. Wheeler, *J. Power Sources* **2009**, *188*, 592.
- [19] A. M. Colclasure, A. R. Dunlop, S. E. Trask, B. J. Polzin, A. N. Jansen, K. Smith, *J. Electrochem. Soc.* **2019**, *166*, A1412.
- [20] H. Zheng, G. Liu, X. Song, P. Ridgway, S. Xun, V. S. Battaglia, *J. Power Sources* **2010**, *157*, A1060.
- [21] H. Zheng, L. Tan, G. Liu, X. Song, V. S. Battaglia, *J. Power Sources* **2012**, *208*, 52.
- [22] J. Kasnatscheew, U. Rodehorst, B. Streipert, S. Wiemers-Meyer, R. Jakelski, R. Wagner, I. C. Laskovic, M. Winter, *J. Electrochem. Soc.* **2016**, *163*, A2943.
- [23] M. S. Whittingham, *Chem. Rev.* **2004**, *104*, 4271.
- [24] B. L. Ellis, K. T. Lee, L. F. Nazar, *Chem. Mater.* **2010**, *22*, 691.
- [25] J. K. Ngala, N. A. Chernova, M. Ma, M. Mamak, P. Y. Zavalij, M. S. Whittingham, *J. Mater. Chem.* **2004**, *14*, 214.
- [26] J.-M. Kim, H.-T. Chung, *Electrochim. Acta* **2004**, *49*, 937.
- [27] A. Kraysberg, Y. Ein-Eli, *J. Solid State Electrochem.* **2017**, *21*, 1907.
- [28] F. Wu, G. Yushin, *Energy Environ. Sci.* **2017**, *10*, 435.
- [29] L. Li, R. Jacobs, P. Gao, L. Gan, F. Wang, D. Morgan, S. Jin, *J. Am. Chem. Soc.* **2016**, *138*, 2838.
- [30] T. P. Heins, N. Harms, L.-S. Schramm, U. Schröder, *Energy Technol.* **2016**, *4*, 1509.
- [31] C.-F. Chen, P. P. Mukherjee, *Phys. Chem. Chem. Phys.* **2015**, *17*, 9812.
- [32] A. Tokranov, R. Kumar, C. Li, S. Minne, X. Xiao, B. W. Sheldon, *Adv. Energy Mater.* **2016**, *6*, 1502302.
- [33] L. M. Riegger, R. Schlem, J. Sann, W. G. Zeier, J. Janek, *Angew. Chem., Int. Ed.* **2021**, *60*, 6718.
- [34] T. R. Jow, M. B. Marx, J. L. Allen, *J. Electrochem. Soc.* **2012**, *159*, A604.
- [35] W. Weppner, R. A. Huggins, *Annu. Rev. Mater. Sci.* **1978**, *8*, 269.
- [36] a) T. Waldmann, B.-I. Hogg, M. Wohlfahrt-Mehrens, *J. Power Sources* **2018**, *384*, 107; b) V. Kabra, M. Parmananda, C. Fear, F. L. E. Usseglio-Viretta, A. Colclasure, K. Smith, P. P. Mukherjee, *ACS Appl. Mater. Interfaces* **2020**, *12*, 55795; c) M.-T. F. Rodrigues, K. Kalaga, S. E. Trask, D. W. Dees, I. A. Shkrob, D. P. Abraham, *J. Electrochem. Soc.* **2019**, *166*, A996.
- [37] C. Mao, R. E. Ruther, J. Li, Z. Du, I. Belharouak, *Electrochem. Commun.* **2018**, *97*, 37.
- [38] X.-G. Yang, C.-Y. Wang, *J. Power Sources* **2018**, *402*, 489.
- [39] a) S. S. Zhang, *J. Energy Chem.* **2020**, *41*, 135; b) R. Jung, M. Metzger, F. Maglia, C. Stinner, H. A. Gasteiger, *J. Electrochem. Soc.* **2017**, *164*, A1361; c) D. Streich, C. Erk, A. Guéguen, P. Müller, F.-F. Chesneau, E. J. Berg, *J. Phys. Chem. C* **2017**, *121*, 13481; d) B. Strehle, K. Kleiner, R. Jung, F. Chesneau, M. Mendez, H. A. Gasteiger, M. Piana, *J. Electrochem. Soc.* **2017**, *164*, A400.
- [40] R. Usiskin, J. Maier, *Adv. Energy Mater.* **2021**, *11*, 2001455.
- [41] R. Amin, Y.-M. Chiang, *J. Electrochem. Soc.* **2016**, *163*, A1512.
- [42] C. Heubner, M. Schneider, A. Michaelis, *Adv. Energy Mater.* **2020**, *10*, 1902523.
- [43] R. E. Usiskin, J. Maier, *Phys. Chem. Chem. Phys.* **2018**, *20*, 16449.
- [44] W. Weppner, R. A. Huggins, *J. Electrochem. Soc.* **1977**, *124*, 1569.
- [45] C. J. Wen, B. A. Boukamp, R. A. Huggins, W. Weppner, *J. Electrochem. Soc.* **1979**, *126*, 2258.
- [46] A. Honders, J. M. der Kinderen, A. H. van Heeren, J. H. W. de Wit, G. H. J. Broers, *Solid State Ionics* **1985**, *15*, 265.
- [47] M. Doyle, J. Newman, *J. Appl. Electrochem.* **1997**, *27*, 846.
- [48] R. Ruess, S. Schweidler, H. Hemmelmann, G. Conforto, A. Bielefeld, D. A. Weber, J. Sann, M. T. Elm, J. Janek, *J. Electrochem. Soc.* **2020**, *167*, 100532.
- [49] a) S. Cui, Y. Wei, T. Liu, W. Deng, Z. Hu, Y. Su, H. Li, M. Li, H. Guo, Y. Duan, W. Wang, M. Rao, J. Zheng, X. Wang, F. Pan, *Adv. Energy Mater.* **2016**, *6*, 1501309; b) A. van der Ven, G. Ceder, *J. Power Sources* **2001**, *97-98*, 529; c) M. D. Levi, D. Aurbach, *J. Phys. Chem. B* **1997**, *101*, 4641; d) M. D. Levi, E. Markevich, D. Aurbach, *J. Phys. Chem. B* **2005**, *109*, 7420.
- [50] J. C. Bachman, S. Muy, A. Grimaud, H.-H. Chang, N. Pour, S. F. Lux, O. Paschos, F. Maglia, S. Lupart, P. Lamp, L. Giordano, Y. Shao-Horn, *Chem. Rev.* **2016**, *116*, 140.
- [51] S. P. Culver, R. Koerver, T. Krauskopf, W. G. Zeier, *Chem. Mater.* **2018**, *30*, 4179.
- [52] R. J. D. Tilley, *Defects in Solids*, Wiley, Hoboken, NJ **2008**.
- [53] a) B. E. Francisco, C. R. Stoldt, J.-C. M'Peko, *Chem. Mater.* **2014**, *26*, 4741; b) H. Sato, in *Topics in Applied Physics* (Ed: S. Geller), Vol. 21, Springer, Berlin, Heidelberg **1977**, pp. 3–39.
- [54] M. D. Levi, E. Markevich, D. Aurbach, *Electrochim. Acta* **2005**, *51*, 98.
- [55] A. Funabiki, M. Inaba, T. Abe, Z. Ogumi, *J. Electrochem. Soc.* **1999**, *146*, 2443.
- [56] Y. Zhu, C. Wang, *J. Phys. Chem. C* **2010**, *114*, 2830.
- [57] L. de Biasi, B. Schwarz, T. Brezesinski, P. Hartmann, J. Janek, H. Ehrenberg, *Adv. Mater.* **2019**, *31*, 1900985.
- [58] W. Dreyer, J. Jamnik, C. Gohlke, R. Huth, J. Moskon, M. Gaberscek, *Nat. Mater.* **2010**, *9*, 448.
- [59] W. Cai, Y.-X. Yao, G.-L. Zhu, C. Yan, L.-L. Jiang, C. He, J.-Q. Huang, Q. Zhang, *Chem. Soc. Rev.* **2020**, *49*, 3806.
- [60] P. L. Taberna, S. Mitra, P. Poizot, P. Simon, J.-M. Tarascon, *Nat. Mater.* **2006**, *5*, 567.
- [61] M. Schönleber, C. Uhlmann, P. Braun, A. Weber, E. Ivers-Tiffée, *Electrochim. Acta* **2017**, *243*, 250.
- [62] a) A. M. Colclasure, R. J. Kee, *Electrochim. Acta* **2010**, *55*, 8960; b) T. F. Fuller, M. Doyle, J. Newman, *J. Electrochem. Soc.* **1994**, *141*, 1.
- [63] A. J. Bard, L. R. Faulkner, *Electrochemical Methods: Fundamentals and Applications*, 2nd ed., Wiley, New York **2000**.
- [64] a) C. Li, H. P. Zhang, L. J. Fu, H. Liu, Y. P. Wu, E. Rahm, R. Holze, H. Q. Wu, *Electrochim. Acta* **2006**, *51*, 3872; b) P. Guan, L. Zhou, Z. Yu, Y. Sun, Y. Liu, F. Wu, Y. Jiang, D. Chu, *J. Energy Chem.* **2020**, *43*, 220; c) T. Nakamura, K. Amezawa, J. Kulisch, W. G. Zeier, J. Janek, *ACS Appl. Mater. Interfaces* **2019**, *11*, 19968.
- [65] Y. Li, Y. Qi, *Energy Environ. Sci.* **2019**, *12*, 1286.
- [66] D. Liu, C. Zhang, G. Zhou, W. Lv, G. Ling, L. Zhi, Q.-H. Yang, *Adv. Sci.* **2018**, *5*, 1700270.
- [67] J. Landesfeind, H. A. Gasteiger, *J. Electrochem. Soc.* **2019**, *166*, A3079.
- [68] Y. Kato, S. Hori, T. Saito, K. Suzuki, M. Hirayama, A. Mitsui, M. Yonemura, H. Iba, R. Kanno, *Nat. Energy* **2016**, *1*, 16030.
- [69] a) A. M. Colclasure, T. R. Tanim, A. N. Jansen, S. E. Trask, A. R. Dunlop, B. J. Polzin, I. Bloom, D. Robertson, L. Flores, M. Evans, E. J. Dufek, K. Smith, *Electrochim. Acta* **2020**, *337*, 135854; b) W. Mai, F. L. Usseglio-Viretta, A. M. Colclasure, K. Smith, *Electrochim. Acta* **2020**, *341*, 136013; c) F. Usseglio-Viretta, W. Mai, A. M. Colclasure, M. Doeff, E. Yi, K. Smith, *Electrochim. Acta* **2020**, *342*, 136034.
- [70] P. Minnmann, L. Quillman, S. Burkhardt, F. H. Richter, J. Janek, *J. Electrochem. Soc.* **2021**, *168*, 040537.
- [71] A. Bielefeld, D. A. Weber, J. Janek, *ACS Appl. Mater. Interfaces* **2020**, *12*, 12821.
- [72] Y. Kato, S. Shiotani, K. Morita, K. Suzuki, M. Hirayama, R. Kanno, *J. Phys. Chem. Lett.* **2018**, *9*, 607.
- [73] A. Bielefeld, D. A. Weber, J. Janek, *J. Phys. Chem. C* **2019**, *123*, 1626.
- [74] Z. Ogumi, *Electrochemistry* **2010**, *78*, 319.
- [75] Y. Yamada, Y. Iriyama, T. Abe, Z. Ogumi, *Langmuir* **2009**, *25*, 12766.

- [76] Z. Ogumi, T. Abe, T. Fukutsuka, S. Yamate, Y. Iriyama, *J. Power Sources* **2004**, 127, 72.
- [77] T. Abe, H. Fukuda, Y. Iriyama, Z. Ogumi, *J. Electrochem. Soc.* **2004**, 151, A1120.
- [78] K. Xu, A. von Cresce, U. Lee, *Langmuir* **2010**, 26, 11538.
- [79] F. Yao, F. Güneş, H. Q. Ta, S. M. Lee, S. J. Chae, K. Y. Sheem, C. S. Cojocar, S. S. Xie, Y. H. Lee, *J. Am. Chem. Soc.* **2012**, 134, 8646.
- [80] S. Thinius, M. M. Islam, P. Heitjans, T. Bredow, *J. Phys. Chem. C* **2014**, 118, 2273.
- [81] K. Zaghib, G. Nadeau, K. Kinoshita, *J. Electrochem. Soc.* **2000**, 147, 2110.
- [82] T. Kar, J. Pattanayak, S. Scheiner, *J. Phys. Chem. A* **2001**, 105, 10397.
- [83] P. Kaghazchi, *Appl. Phys. Lett.* **2013**, 102, 093901.
- [84] C.-Y. Chou, H. Kim, G. S. Hwang, *J. Phys. Chem. C* **2011**, 115, 20018.
- [85] H. Kim, K. E. Kweon, C.-Y. Chou, J. G. Ekerdt, G. S. Hwang, *J. Phys. Chem. C* **2010**, 114, 17942.
- [86] O. I. Malý, T. L. Tan, S. Manzhos, *Appl. Phys. Express* **2013**, 6, 027301.
- [87] W. Wan, Q. Zhang, Y. Cui, E. Wang, *J. Phys.: Condens. Matter* **2010**, 22, 415501.
- [88] Z. Wang, Q. Su, H. Deng, W. He, J. Lin, Y. Q. Fu, *J. Mater. Chem. A* **2014**, 2, 13976.
- [89] Q. Zhang, W. Zhang, W. Wan, Y. Cui, E. Wang, *Nano Lett.* **2010**, 10, 3243.
- [90] T. Krauskopf, F. H. Richter, W. G. Zeier, J. Janek, *Chem. Rev.* **2020**, 120, 7745.
- [91] a) J. Asenbauer, T. Eisenmann, M. Kuenzel, A. Kazzazi, Z. Chen, D. Bresser, *Sustainable Energy Fuels* **2020**, 4, 5387; b) I. L. Spain, A. R. Ubbelohde, D. A. Young, *Philos. Trans. R. Soc. London* **1967**, 262, 345.
- [92] S. Suh, H. Choi, K. Eom, H.-J. Kim, *J. Alloys Compd.* **2020**, 827, 154102.
- [93] X. Zeng, M. Li, D. Abd El-Hady, W. Alshitari, A. S. Al-Bogami, J. Lu, K. Amine, *Adv. Energy Mater.* **2019**, 9, 1900161.
- [94] J. Wolfenstine, U. Lee, J. L. Allen, *J. Power Sources* **2006**, 154, 287.
- [95] P. Heitjans, A. Korblein, H. Ackermann, D. Dubbers, F. Fujara, H.-J. Stockmann, *J. Phys. F: Met. Phys.* **1985**, 15, 41.
- [96] M. Wang, J. B. Wolfenstine, J. Sakamoto, *Electrochim. Acta* **2019**, 296, 842.
- [97] A. Masias, N. Felten, R. Garcia-Mendez, J. Wolfenstine, J. Sakamoto, *J. Mater. Sci.* **2019**, 54, 2585.
- [98] K. Persson, V. A. Sethuraman, L. J. Hardwick, Y. Hinuma, Y. S. Meng, A. van der Ven, V. Srinivasan, R. Kostecki, G. Ceder, *J. Phys. Chem. Lett.* **2010**, 1, 1176.
- [99] K. Persson, Y. Hinuma, Y. S. Meng, A. van der Ven, G. Ceder, *Phys. Rev. B* **2010**, 82, 125416.
- [100] T. L. Kulova, A. M. Skundin, E. A. Nizhnikovskii, A. V. Fesenko, *Russ. J. Electrochem.* **2006**, 42, 259.
- [101] A. Funabiki, M. Inaba, Z. Ogumi, S. Yuasa, J. Otsuji, A. Tasaka, *J. Electrochem. Soc.* **1998**, 145, 172.
- [102] H. Lin, D. Chua, M. Salomon, H.-C. Shiao, M. Hendrickson, E. Plichta, S. Slane, *J. Electrochem. Soc.* **2001**, 4, A71.
- [103] S. Tippmann, D. Walper, L. Balboa, B. Spier, W. G. Bessler, *J. Power Sources* **2014**, 252, 305.
- [104] T. Waldmann, B.-I. Hogg, M. Kasper, S. Grolleau, C. G. Couceiro, K. Trad, B. P. Matadi, M. Wohlfahrt-Mehrens, *J. Electrochem. Soc.* **2016**, 163, A1232.
- [105] B.-I. Hogg, T. Waldmann, M. Wohlfahrt-Mehrens, *J. Electrochem. Soc.* **2020**, 167, 090525.
- [106] W. Cai, C. Yan, Y.-X. Yao, L. Xu, R. Xu, L.-L. Jiang, J.-Q. Huang, Q. Zhang, *Small Struct.* **2020**, 1, 2000010.
- [107] C. Uthaisar, V. Barone, *Nano Lett.* **2010**, 10, 2838.
- [108] Y. W. Koh, S. Manzhos, *MRS Commun.* **2013**, 3, 171.
- [109] G. A. Tritsarlis, K. Zhao, O. U. Okeke, E. Kaxiras, *J. Phys. Chem. C* **2012**, 116, 22212.
- [110] N. Ding, J. Xu, Y. X. Yao, G. Wegner, X. Fang, C. H. Chen, I. Lieberwirth, *Solid State Ionics* **2009**, 180, 222.
- [111] E. Quiroga-González, J. Carstensen, H. Föll, *Energies* **2013**, 6, 5145.
- [112] B. Wang, J. Ryu, S. Choi, X. Zhang, D. Pribat, X. Li, L. Zhi, S. Park, R. S. Ruoff, *ACS Nano* **2019**, 13, 2307.
- [113] T. Takamura, S. Ohara, M. Uehara, J. Suzuki, K. Sekine, *J. Power Sources* **2004**, 129, 96.
- [114] C. Yu, X. Li, T. Ma, J. Rong, R. Zhang, J. Shaffer, Y. An, Q. Liu, B. Wei, H. Jiang, *Adv. Energy Mater.* **2012**, 2, 68.
- [115] X. Han, Z. Zhang, H. Chen, L. Luo, Q. Zhang, J. Chen, S. Chen, Y. Yang, *J. Mater. Chem. A* **2021**, 9, 3628.
- [116] D. A. Lozhkina, A. M. Rumyantsev, E. V. Astrova, *Semiconductors* **2020**, 54, 383.
- [117] B. Deng, R. Xu, X. Wang, L. An, K. Zhao, G. J. Cheng, *Energy Storage Mater.* **2019**, 22, 450.
- [118] X. Shen, Z. Tian, R. Fan, L. e Shao, D. Zhang, G. Cao, L. Kou, Y. Bai, *J. Energy Chem.* **2018**, 27, 1067.
- [119] G. A. Tritsarlis, E. Kaxiras, S. Meng, E. Wang, *Nano Lett.* **2013**, 13, 2258.
- [120] C. K. Chan, H. Peng, G. Liu, K. McIlwrath, X. F. Zhang, R. A. Huggins, Y. Cui, *Nat. Nanotechnol.* **2008**, 3, 31.
- [121] F. Tielens, M. Calatayud, A. Beltrán, C. Minot, J. Andrés, *J. Electroanal. Chem.* **2005**, 581, 216.
- [122] TOSHIBA, SCiB Rechargeable battery, www.scib.jp (accessed: December 2020).
- [123] S.-T. Myung, J. Kim, Y.-K. Sun, in *Batteries. Present and Future Energy Storage Challenges* (Eds: S. Passerini, D. Bresser, A. Moretti), Wiley-VCH, Weinheim, Germany **2020**, p. 196.
- [124] A. Ghicov, M. Yamamoto, P. Schmuki, *Angew. Chem., Int. Ed.* **2008**, 47, 7934.
- [125] M. Fehse, S. Cavaliere, P. E. Lippens, I. Savych, A. Iadecola, L. Monconduit, D. J. Jones, J. Rozière, F. Fischer, C. Tessier, L. Stievano, *J. Phys. Chem. C* **2013**, 117, 13827.
- [126] M. Pfanzelt, P. Kubiak, M. Fleischhammer, M. Wohlfahrt-Mehrens, *J. Power Sources* **2011**, 196, 6815.
- [127] W. Zhang, D.-H. Seo, T. Chen, L. Wu, M. Topsakal, Y. Zhu, D. Lu, G. Ceder, *Science* **2020**, 367, 1030.
- [128] K. J. Griffith, K. M. Wiaderek, G. Cibin, L. E. Marbella, C. P. Grey, *Nature* **2018**, 559, 556.
- [129] L. Picard, T. Gutel, in *Batteries. Present and Future Energy Storage Challenges* (Eds: S. Passerini, D. Bresser, A. Moretti), Wiley-VCH, Weinheim, Germany **2020**, p. 783.
- [130] Q. Zhao, C. Guo, Y. Lu, L. Liu, J. Liang, J. Chen, *Ind. Eng. Chem. Res.* **2016**, 55, 5795.
- [131] Y. Y. Zhang, Y. Y. Sun, S. X. Du, H.-J. Gao, S. B. Zhang, *Appl. Phys. Lett.* **2012**, 100, 091905.
- [132] S. T. Taleghani, B. Marcos, K. Zaghib, G. Lantagne, *J. Electrochem. Soc.* **2017**, 164, E3179.
- [133] H. Li, H. Zhou, *Chem. Commun.* **2012**, 48, 1201.
- [134] C. Wang, H. Zhao, J. Wang, J. Wang, P. Lv, *Ionics* **2013**, 19, 221.
- [135] F.-S. Li, Y.-S. Wu, J. Chou, M. Winter, N.-L. Wu, *Adv. Mater.* **2015**, 27, 130.
- [136] H. Wang, M. Yoshio, T. Abe, Z. Ogumi, *J. Electrochem. Soc.* **2002**, 149, A499.
- [137] M. Yoshio, H. Wang, K. Fukuda, Y. Hara, Y. Adachi, *J. Electrochem. Soc.* **2000**, 147, 1245.
- [138] S. R. Sivakumar, J. Y. Nerkar, A. G. Pandolfo, *Electrochim. Acta* **2010**, 55, 3330.
- [139] X.-G. Yang, S. Ge, T. Liu, Y. Leng, C.-Y. Wang, *J. Power Sources* **2018**, 395, 251.
- [140] a) A. Sarkar, P. Shrotriya, A. Chandra, *J. Electrochem. Soc.* **2017**, 164, E3606; b) S. Kalnaus, K. Rhodes, C. Daniel, *J. Power Sources* **2011**, 196, 8116.

- [141] X. H. Liu, L. Zhong, S. Huang, S. X. Mao, T. Zhu, J. Y. Huang, *ACS Nano* **2012**, *6*, 1522.
- [142] M. Zhu, J. Park, A. M. Sastry, *J. Electrochem. Soc.* **2012**, *159*, A492.
- [143] K. Zaghbi, X. Song, A. Guerfi, R. Kostecki, K. Kinoshita, *J. Power Sources* **2003**, *124*, 505.
- [144] D. D. MacNeil, D. Larcher, J. R. Dahn, *J. Electrochem. Soc.* **1999**, *146*, 3596.
- [145] T. D. Tran, J. H. Feikert, R. W. Pekala, K. Kinoshita, *J. Appl. Electrochem.* **1996**, *26*, 1161.
- [146] F. Röder, S. Sonntag, D. Schröder, U. Krewer, *Energy Technol.* **2016**, *4*, 1588.
- [147] J. Kim, S. M. Nithya Jeghan, G. Lee, *Microporous Mesoporous Mater.* **2020**, *305*, 110325.
- [148] T. Deng, X. Zhou, *J. Solid State Electrochem.* **2016**, *20*, 2613.
- [149] M. Ebner, V. Wood, *J. Electrochem. Soc.* **2015**, *162*, A3064.
- [150] M. Singh, J. Kaiser, H. Hahn, *J. Electrochem. Soc.* **2015**, *162*, A1196.
- [151] K. G. Gallagher, S. E. Trask, C. Bauer, T. Woehrle, S. F. Lux, M. Tschuch, P. Lamp, B. J. Polzin, S. Ha, B. Long, Q. Wu, W. Lu, D. W. Dees, A. N. Jansen, *J. Electrochem. Soc.* **2016**, *163*, A138.
- [152] T. Danner, M. Singh, S. Hein, J. Kaiser, H. Hahn, A. Latz, *J. Power Sources* **2016**, *334*, 191.
- [153] L. S. Kremer, A. Hoffmann, T. Danner, S. Hein, B. Prifling, D. Westhoff, C. Dreer, A. Latz, V. Schmidt, M. Wohlfahrt-Mehrens, *Energy Technol.* **2020**, *8*, 1900167.
- [154] W. Huang, P. M. Attia, H. Wang, S. E. Renfrew, N. Jin, S. Das, Z. Zhang, D. T. Boyle, Y. Li, M. Z. Bazant, B. D. McCloskey, W. C. Chueh, Y. Cui, *Nano Lett.* **2019**, *19*, 5140.
- [155] C.-Y. Wang, T. Xu, S. Ge, G. Zhang, X.-G. Yang, Y. Ji, *J. Electrochem. Soc.* **2016**, *163*, A1944.
- [156] Y. Ren, L. J. Hardwick, P. G. Bruce, *Angew. Chem., Int. Ed.* **2010**, *49*, 2570.
- [157] J. Billaud, F. Bouville, T. Magrini, C. Villevieille, A. R. Studart, *Nat. Energy* **2016**, *1*, 16097.
- [158] C.-J. Bae, C. K. Erdonmez, J. W. Halloran, Y.-M. Chiang, *Adv. Mater.* **2013**, *25*, 1254.
- [159] K.-H. Chen, M. J. Namkoong, V. Goel, C. Yang, S. Kazemiabnavi, S. M. Mortuza, E. Kazyak, J. Mazumder, K. Thornton, J. Sakamoto, N. P. Dasgupta, *J. Power Sources* **2020**, *471*, 228475.
- [160] L. Kraft, J. B. Hagedorn, A. Frank, A. Rheinfeld, A. Jossen, *J. Electrochem. Soc.* **2020**, *167*, 013506.
- [161] Y.-H. Chen, C.-W. Wang, X. Zhang, A. M. Sastry, *J. Power Sources* **2010**, *195*, 2851.
- [162] M. Broussely, S. Herreyre, P. Biensan, P. Kasztejna, K. Nechev, R. Staniewicz, *J. Power Sources* **2001**, *97*, 13.
- [163] J. Vetter, P. Novák, M. R. Wagner, C. Veit, K.-C. Möller, J. O. Besenhard, M. Winter, M. Wohlfahrt-Mehrens, C. Vogler, A. Hammouche, *J. Power Sources* **2005**, *147*, 269.
- [164] X.-G. Yang, Y. Leng, G. Zhang, S. Ge, C.-Y. Wang, *J. Power Sources* **2017**, *360*, 28.
- [165] J. Shim, K. A. Striebel, *J. Power Sources* **2003**, *119*, 934.
- [166] J. B. Quinn, T. Waldmann, K. Richter, M. Kasper, M. Wohlfahrt-Mehrens, *J. Electrochem. Soc.* **2018**, *165*, A3284.
- [167] M. J. Lain, J. Brandon, E. Kendrick, *Batteries* **2019**, *5*, 64.
- [168] Z. Du, D. L. Wood, C. Daniel, S. Kalnaus, J. Li, *J. Appl. Electrochem.* **2017**, *47*, 405.
- [169] P. Arora, M. Doyle, R. E. White, *J. Electrochem. Soc.* **1999**, *146*, 3543.
- [170] S. Hein, A. Latz, *Electrochim. Acta* **2016**, *201*, 354.
- [171] N. Legrand, B. Knosp, P. Desprez, F. Lapique, S. Raël, *J. Power Sources* **2014**, *245*, 208.
- [172] B. Bitzer, A. Gruhle, *J. Power Sources* **2014**, *262*, 297.
- [173] N. Ghanbari, T. Waldmann, M. Kasper, P. Axmann, M. Wohlfahrt-Mehrens, *J. Phys. Chem. C* **2016**, *120*, 22225.
- [174] N. Ghanbari, T. Waldmann, M. Kasper, P. Axmann, M. Wohlfahrt-Mehrens, *ECS Electrochem. Lett.* **2015**, *4*, A100.
- [175] T. Waldmann, J. B. Quinn, K. Richter, M. Kasper, A. Tost, A. Klein, M. Wohlfahrt-Mehrens, *J. Electrochem. Soc.* **2017**, *164*, A3154.
- [176] Q. Q. Liu, R. Petibon, C. Y. Du, J. R. Dahn, *J. Electrochem. Soc.* **2017**, *164*, A1173.
- [177] T. Waldmann, M. Wilka, M. Kasper, M. Fleischhammer, M. Wohlfahrt-Mehrens, *J. Power Sources* **2014**, *262*, 129.
- [178] P. Arora, R. E. White, M. Doyle, *J. Electrochem. Soc.* **1998**, *145*, 3647.
- [179] S. Liu, L. Xiong, C. He, *J. Power Sources* **2014**, *261*, 285.
- [180] C.-S. Kim, K. M. Jeong, K. Kim, C.-W. Yi, *Electrochim. Acta* **2015**, *155*, 431.
- [181] S. Krueger, R. Kloepsch, J. Li, S. Nowak, S. Passerini, M. Winter, *J. Electrochem. Soc.* **2013**, *160*, A542.
- [182] T. Waldmann, R.-G. Scurtu, K. Richter, M. Wohlfahrt-Mehrens, *J. Power Sources* **2020**, *472*, 228614.
- [183] K.-H. Chen, V. Goel, M. J. Namkoong, M. Wied, S. Müller, V. Wood, J. Sakamoto, K. Thornton, N. P. Dasgupta, *Adv. Energy Mater.* **2021**, *11*, 2003336.
- [184] a) D. Anseán, M. Dubarry, A. Devie, B. Y. Liaw, V. M. García, J. C. Viera, M. González, *J. Power Sources* **2017**, *356*, 36; b) T. C. Bach, S. F. Schuster, E. Fleder, J. Müller, M. J. Brand, H. Lormann, A. Jossen, G. Sextl, *J. Energy Storage* **2016**, *5*, 212; c) C. Birkenmaier, B. Bitzer, M. Harzheim, A. Hintennach, T. Schleid, *J. Electrochem. Soc.* **2015**, *162*, A2646; d) M. Ecker, P. Shafiei Sabet, D. U. Sauer, *Appl. Energy* **2017**, *206*, 934; e) C. von Lüders, V. Zinth, S. V. Erhard, P. J. Osswald, M. Hofmann, R. Gilles, A. Jossen, *J. Power Sources* **2017**, *342*, 17; f) V. Zinth, C. von Lüders, M. Hofmann, J. Hattendorff, I. Buchberger, S. Erhard, J. Rebelo-Kornmeier, A. Jossen, R. Gilles, *J. Power Sources* **2014**, *271*, 152.
- [185] J. C. Burns, D. A. Stevens, J. R. Dahn, *J. Electrochem. Soc.* **2015**, *162*, A959.
- [186] K. Richter, T. Waldmann, N. Paul, N. Jobst, R.-G. Scurtu, M. Hofmann, R. Gilles, M. Wohlfahrt-Mehrens, *ChemSusChem* **2020**, *13*, 529.
- [187] Z. Li, J. Huang, B. Yann Liaw, V. Metzler, J. Zhang, *J. Power Sources* **2014**, *254*, 168.
- [188] a) M. Fleischhammer, T. Waldmann, G. Bisle, B.-I. Hogg, M. Wohlfahrt-Mehrens, *J. Power Sources* **2015**, *274*, 432; b) T. Waldmann, M. Wohlfahrt-Mehrens, *Electrochim. Acta* **2017**, *230*, 454.
- [189] X.-G. Yang, T. Liu, Y. Gao, S. Ge, Y. Leng, D. Wang, C.-Y. Wang, *Joule* **2019**, *3*, 3002.
- [190] J. L. Tirado, *Mater. Sci. Eng., R* **2003**, *40*, 103.
- [191] M. Winter, J. O. Besenhard, *Electrochim. Acta* **1999**, *45*, 31.
- [192] T.-H. Kim, E. K. Jeon, Y. Ko, B. Y. Jang, B.-S. Kim, H.-K. Song, *J. Mater. Chem. A* **2014**, *2*, 7600.
- [193] Q. Cheng, Y. Okamoto, N. Tamura, M. Tsuji, S. Maruyama, Y. Matsuo, *Sci. Rep.* **2017**, *7*, 14782.
- [194] R. Mo, D. Rooney, K. Sun, H. Y. Yang, *Nat. Commun.* **2017**, *8*, 13949.
- [195] X. Rao, Y. Lou, J. Chen, H. Lu, B. Cheng, W. Wang, H. Fang, H. Li, S. Zhong, *Front. Energy Res.* **2020**, *8*, 652.
- [196] H.-J. Kim, J.-S. Kim, S.-W. Song, *J. Solid State Chem.* **2019**, *270*, 479.
- [197] T. Xu, P. Gao, P. Li, K. Xia, N. Han, J. Deng, Y. Li, J. Lu, *Adv. Energy Mater.* **2020**, *10*, 1902343.
- [198] H. Wang, D. Lin, Y. Liu, Y. Li, Y. Cui, *Sci. Adv.* **2017**, *3*, 1701301.
- [199] N. Kim, S. Chae, J. Ma, M. Ko, J. Cho, *Nat. Commun.* **2017**, *8*, 812.
- [200] J.-C. Daigle, Y. Asakawa, M. Beaupré, V. Gariépy, R. Vieillette, D. Laul, M. Trudeau, K. Zaghbi, *Sci. Rep.* **2019**, *9*, 16871.
- [201] B. Wang, J. S. Chen, H. B. Wu, Z. Wang, X. W. Lou, *J. Am. Chem. Soc.* **2011**, *133*, 17146.
- [202] T. Muraliganth, A. Vadivel Murugan, A. Manthiram, *Chem. Commun.* **2009**, *45*, 7360.
- [203] Y. Sun, X. Hu, W. Luo, Y. Huang, *J. Phys. Chem. C* **2012**, *116*, 20794.
- [204] H. Yang, S. Zhang, L. Han, Z. Zhang, Z. Xue, J. Gao, Y. Li, C. Huang, Y. Yi, H. Liu, Y. Li, *ACS Appl. Mater. Interfaces* **2016**, *8*, 5366.

- [205] J. Haetge, P. Hartmann, K. Brezesinski, J. Janek, T. Brezesinski, *Chem. Mater.* **2011**, *23*, 4384.
- [206] a) X.-G. Yang, G. Zhang, S. Ge, C.-Y. Wang, *Proc. Natl. Acad. Sci. USA* **2018**, *115*, 7266; b) H. Ruan, J. Jiang, B. Sun, X. Su, X. He, K. Zhao, *Appl. Energy* **2019**, *256*, 113797; c) J. Zhang, H. Ge, Z. Li, Z. Ding, *J. Power Sources* **2015**, *273*, 1030.
- [207] a) J. B. Goodenough, Y. Kim, *J. Power Sources* **2011**, *196*, 6688; b) J. B. Goodenough, Y. Kim, *Chem. Mater.* **2010**, *22*, 587; c) B. Kang, G. Ceder, *Nature* **2009**, *458*, 190; d) P. Gao, G. Yang, H. Liu, L. Wang, H. Zhou, *Solid State Ionics* **2012**, *207*, 50; e) J. Kasnatscheew, M. Börner, B. Streipert, P. Meister, R. Wagner, I. Cekic Laskovic, M. Winter, *J. Power Sources* **2017**, *362*, 278; f) G. Homann, P. Meister, L. Stolz, J. P. Brinkmann, J. Kulisch, T. Adermann, M. Winter, J. Kasnatscheew, *ACS Appl. Energy Mater.* **2020**, *3*, 3162.
- [208] K. Mizushima, P. C. Jones, P. J. Wiseman, J. B. Goodenough, *Mater. Res. Bull.* **1980**, *15*, 783.
- [209] R. Nölle, K. Beltrop, F. Holtstiege, J. Kasnatscheew, T. Placke, M. Winter, *Mater. Today* **2020**, *32*, 131.
- [210] J. Kasnatscheew, T. Placke, B. Streipert, S. Rothermel, R. Wagner, P. Meister, I. C. Laskovic, M. Winter, *J. Electrochem. Soc.* **2017**, *164*, A2479.
- [211] a) Y. Watanabe, S. Kinoshita, S. Wada, K. Hoshino, H. Morimoto, S. Tobishima, *J. Power Sources* **2008**, *179*, 770; b) A. V. Churikov, *Electrochim. Acta* **2001**, *46*, 2415; c) P. Novák, D. Goers, L. Hardwick, M. Holzapfel, W. Scheifele, J. Ufheil, A. Würsig, *J. Power Sources* **2005**, *146*, 15; d) P. Novák, J.-C. Panitz, F. Joho, M. Lanz, R. Imhof, M. Coluccia, *J. Power Sources* **2000**, *90*, 52; e) C.-H. Chen, F. Brosa Planella, K. O'Regan, D. Gastol, W. D. Widanage, E. Kendrick, *J. Electrochem. Soc.* **2020**, *167*, 080534.
- [212] K. Amine, J. Liu, I. Belharouak, S.-H. Kang, I. Bloom, D. Vissers, G. Henriksen, *J. Power Sources* **2005**, *146*, 111.
- [213] a) J. Kasnatscheew, S. Röser, M. Börner, M. Winter, *ACS Appl. Energy Mater.* **2019**, *2*, 7733; b) S. J. An, J. Li, C. Daniel, S. Kalnaus, D. L. Wood, *J. Electrochem. Soc.* **2017**, *164*, A1755; c) Y. Sun, C. Ouyang, Z. Wang, X. Huang, L. Chen, *J. Electrochem. Soc.* **2004**, *151*, A504; d) K. Kang, Y. S. Meng, J. Bréger, C. P. Grey, G. Ceder, *Science* **2006**, *311*, 977; e) D. Aurbach, *J. Power Sources* **2003**, *119*, 497.
- [214] J. Kasnatscheew, M. Evertz, B. Streipert, R. Wagner, R. Klöpsch, B. Vortmann, H. Hahn, S. Nowak, M. Amereller, A.-C. Gentschev, P. Lamp, M. Winter, *Phys. Chem. Chem. Phys.* **2016**, *18*, 3956.
- [215] J. Kasnatscheew, M. Evertz, R. Kloepsch, B. Streipert, R. Wagner, I. Cekic Laskovic, M. Winter, *Energy Technol.* **2017**, *5*, 1670.
- [216] J. Kasnatscheew, B. Streipert, S. Röser, R. Wagner, I. Cekic Laskovic, M. Winter, *Phys. Chem. Chem. Phys.* **2017**, *19*, 16078.
- [217] B. Streipert, L. Stolz, G. Homann, P. Janßen, I. Cekic-Laskovic, M. Winter, *J. Kasnatscheew, ChemSusChem* **2020**, *13*, 5301.
- [218] a) X. Qi, B. Blizanac, A. DuPasquier, M. Oljaca, J. Li, M. Winter, *Carbon* **2013**, *64*, 334; b) S. F. Lux, F. Schappacher, A. Balducci, S. Passerini, M. Winter, *J. Electrochem. Soc.* **2010**, *157*, A320.
- [219] a) Y. Wei, J. Zheng, S. Cui, X. Song, Y. Su, W. Deng, Z. Wu, X. Wang, W. Wang, M. Rao, Y. Lin, C. Wang, K. Amine, F. Pan, *J. Am. Chem. Soc.* **2015**, *137*, 8364; b) A. Kraysberg, Y. Ein-Eli, *Adv. Energy Mater.* **2012**, *2*, 922.
- [220] J. B. Goodenough, K. Mizushima, US 4302518, **1980**.
- [221] E. Trevisanello, R. Ruess, G. Conforto, F. H. Richter, J. Janek, *Adv. Energy Mater.* **2021**, *11*, 2003400.
- [222] B.-B. Lim, S.-T. Myung, C. S. Yoon, Y.-K. Sun, *ACS Energy Lett.* **2016**, *1*, 283.
- [223] H.-J. Noh, Z. Chen, C. S. Yoon, J. Lu, K. Amine, Y.-K. Sun, *Chem. Mater.* **2013**, *25*, 2109.
- [224] S. Lee, Y. Cho, H.-K. Song, K. T. Lee, J. Cho, *Angew. Chem., Int. Ed.* **2012**, *51*, 8748.
- [225] S. Klein, P. Bärman, O. Fromm, K. Borzutzki, J. Reiter, Q. Fan, M. Winter, T. Placke, J. Kasnatscheew, *J. Mater. Chem. A* **2021**, *9*, 7546.
- [226] S. Yasuhara, S. Yasui, T. Teranishi, K. Chajima, Y. Yoshikawa, Y. Majima, T. Taniyama, M. Itoh, *Nano Lett.* **2019**, *19*, 1688.
- [227] T. Teranishi, Y. Yoshikawa, R. Sakuma, H. Hashimoto, H. Hayashi, A. Kishimoto, T. Fujii, *Appl. Phys. Lett.* **2014**, *105*, 143904.
- [228] M. Wang, X. Feng, H. Xiang, Y. Feng, C. Qin, P. Yan, Y. Yu, *Small Methods* **2019**, *3*, 1900355.
- [229] Q. Wu, X. Zhang, S. Sun, N. Wan, D. u Pan, Y. Bai, H. Zhu, Y.-S. Hu, S. Dai, *Nanoscale* **2015**, *7*, 15609.
- [230] U. Nisar, R. Amin, R. Essehli, R. A. Shakoor, R. Kahraman, D. K. Kim, M. A. Khaleel, I. Belharouak, *J. Power Sources* **2018**, *396*, 774.
- [231] U. Nisar, S. A. J. A. Al-Hail, R. K. Petla, R. A. Shakoor, R. Essehli, R. Kahraman, S. Y. AlQaradawi, D. K. Kim, I. Belharouak, M. R. Amin, *ACS Appl. Energy Mater.* **2019**, *2*, 7263.
- [232] J.-J. Pan, B. Chen, Y. Xie, N. Ren, T.-F. Yi, *Mater. Lett.* **2019**, *253*, 136.
- [233] Z. Chen, F. Xu, S. Cao, Z. Li, H. Yang, X. Ai, Y. Cao, *Small* **2017**, *13*, 1603148.
- [234] X. Xu, Y.-Z. Luo, L.-Q. Mai, Y.-L. Zhao, Q.-Y. An, L. Xu, F. Hu, L. Zhang, Q.-J. Zhang, *NPG Asia Mater* **2012**, *4*, e20.
- [235] Y. Lu, J. Chen, *Nat. Rev. Chem.* **2020**, *4*, 127.
- [236] F. Otteny, G. Studer, M. Kolek, P. Bieker, M. Winter, B. Esser, *ChemSusChem* **2020**, *13*, 2232.
- [237] F. Otteny, V. Perner, D. Wassy, M. Kolek, P. Bieker, M. Winter, B. Esser, *ACS Sustainable Chem. Eng.* **2020**, *8*, 238.
- [238] S. Gu, Z. Bai, S. Majumder, B. Huang, G. Chen, *J. Power Sources* **2019**, *429*, 22.
- [239] T. Teranishi, K. Kozai, S. Yasuhara, S. Yasui, N. Ishida, K. Ishida, M. Nakayama, A. Kishimoto, *J. Power Sources* **2021**, *494*, 229710.
- [240] E. Krämer, T. Schedlbauer, B. Hoffmann, L. Terborg, S. Nowak, H. J. Gores, S. Passerini, M. Winter, *J. Electrochem. Soc.* **2013**, *160*, A356.
- [241] a) N. Imanishi, M. Fujiyoshi, Y. Takeda, O. Yamamoto, M. Tabuchi, *Solid State Ionics* **1999**, *118*, 121; b) S. Lévassieur, M. Ménétrier, E. Suard, C. Delmas, *Solid State Ionics* **2000**, *128*, 11.
- [242] F. Croce, F. Nobili, A. Deplata, W. Lada, R. Tossici, A. D'Epifanio, B. Scrosati, R. Marassi, *Electrochem. Commun.* **1999**, *1*, 605.
- [243] G. Liu, H. Zheng, S. Kim, Y. Deng, A. M. Minor, X. Song, V. S. Battaglia, *J. Electrochem. Soc.* **2008**, *155*, A887.
- [244] A. Nyman, M. Behm, G. Lindbergh, *Electrochim. Acta* **2008**, *53*, 6356.
- [245] I. Saadouné, C. Delmas, *J. Mater. Chem.* **1996**, *6*, 193.
- [246] S. Klein, K. Borzutzki, P. Schneider, O. Fromm, J. Reiter, Q. Fan, T. Placke, M. Winter, J. Kasnatscheew, *Chem. Mater.* **2020**, *32*, 6279.
- [247] X. Liu, G. Zhu, K. Yang, J. Wang, *J. Power Sources* **2007**, *174*, 1126.
- [248] a) L. Zou, W. Zhao, Z. Liu, H. Jia, J. Zheng, G. Wang, Y. Yang, J.-G. Zhang, C. Wang, *ACS Energy Lett.* **2018**, *3*, 2433; b) S. Hwang, E. Jo, K. Y. Chung, K. S. Hwang, S. M. Kim, W. Chang, *J. Phys. Chem. Lett.* **2017**, *8*, 5758.
- [249] a) H. Liu, M. Wolf, K. Karki, Y.-S. Yu, E. A. Stach, J. Cabana, K. W. Chapman, P. J. Chupas, *Nano Lett.* **2017**, *17*, 3452; b) J.-M. Lim, T. Hwang, D. Kim, M.-S. Park, K. Cho, M. Cho, *Sci. Rep.* **2017**, *7*, 39669; c) D. J. Miller, C. Proff, J. G. Wen, D. P. Abraham, J. Bareño, *Adv. Energy Mater.* **2013**, *3*, 1098; d) E.-J. Lee, Z. Chen, H.-J. Noh, S. C. Nam, S. Kang, D. H. Kim, K. Amine, Y.-K. Sun, *Nano Lett.* **2014**, *14*, 4873.
- [250] a) H.-H. Ryu, K.-J. Park, C. S. Yoon, Y.-K. Sun, *Chem. Mater.* **2018**, *30*, 1155; b) W. Li, H. Y. Asl, Q. Xie, A. Manthiram, *J. Am. Chem. Soc.* **2019**, *141*, 5097; c) A. O. Kondrakov, A. Schmidt, J. Xu, H. Geßwein, R. Mönig, P. Hartmann, H. Sommer, T. Brezesinski, J. Janek, *J. Phys. Chem. C* **2017**, *121*, 3286; d) Y. Mao, X. Wang, S. Xia, K. Zhang, C. Wei, S. Bak, Z. Shadique, X. Liu, Y. Yang, R. Xu, P. Pianetta, S. Ermon, E. Stavitski, K. Zhao, Z. Xu, F. Lin, X.-Q. Yang, E. Hu, Y. Liu, *Adv. Funct. Mater.* **2019**, *29*, 1900247; e) S. Xia, L. Mu, Z. Xu, J. Wang, C. Wei, L. Liu, P. Pianetta, K. Zhao, X. Yu, F. Lin, Y. Liu, *Nano Energy* **2018**, *53*, 753.

- [251] J. Kasnatscheew, M. Evertz, B. Streipert, R. Wagner, S. Nowak, I. Cekic Laskovic, M. Winter, *J. Power Sources* **2017**, 359, 458.
- [252] M. Winter, B. Barnett, K. Xu, *Chem. Rev.* **2018**, 118, 11433.
- [253] K. Xu, *Chem. Rev.* **2004**, 104, 4303.
- [254] a) G. Li, Z. Liu, Q. Huang, Y. Gao, M. Regula, D. Wang, L.-Q. Chen, D. Wang, *Nat. Energy* **2018**, 3, 1076; b) G. Li, Z. Liu, D. Wang, X. He, S. Liu, Y. Gao, A. AlZahrani, S. H. Kim, L.-Q. Chen, D. Wang, *Adv. Energy Mater.* **2019**, 9, 1900704; c) G. Li, *Adv. Energy Mater.* **2021**, 11, 2002891.
- [255] K. Xu, A. von Cresce, *J. Mater. Chem.* **2011**, 21, 9849.
- [256] a) T. Abe, F. Sagane, M. Ohtsuka, Y. Iriyama, Z. Ogumi, *Electrochim. Acta* **2005**, 152, A2151; b) Y. Yamada, F. Sagane, Y. Iriyama, T. Abe, Z. Ogumi, *J. Phys. Chem. C* **2009**, 113, 14528; c) T. Doi, Y. Iriyama, T. Abe, Z. Ogumi, *Anal. Chem.* **2005**, 77, 1696; d) I. Yamada, T. Abe, Y. Iriyama, Z. Ogumi, *Electrochem. Commun.* **2003**, 5, 502; e) I. Yamada, Y. Iriyama, T. Abe, Z. Ogumi, *J. Power Sources* **2007**, 172, 933.
- [257] a) S. Yanase, T. Oi, *J. Nucl. Sci. Technol.* **2002**, 39, 1060; b) T. Fukushima, Y. Matsuda, H. Hashimoto, R. Arakawa, *J. Phys. Chem. A* **2001**, 4, A127.
- [258] Y. Matsuda, T. Fukushima, H. Hashimoto, R. Arakawa, *J. Power Sources* **2002**, 149, A1045.
- [259] B. Wen, Z. Deng, P.-C. Tsai, Z. W. Lebens-Higgins, L. F. J. Piper, S. P. Ong, Y.-M. Chiang, *Nat. Energy* **2020**, 5, 578.
- [260] a) J. Kasnatscheew, R. Wagner, M. Winter, I. Cekic-Laskovic, in *Topics in Current Chemistry Collections* (Ed: M. Korth), Springer, Cham **2018**, pp. 23–51; b) G. Homann, L. Stolz, K. Neuhaus, M. Winter, J. Kasnatscheew, *Adv. Funct. Mater.* **2020**, 30, 2006289; c) G. Homann, L. Stolz, M. Winter, J. Kasnatscheew, *iScience* **2020**, 23, 101225; d) G. Homann, L. Stolz, J. Nair, I. C. Laskovic, M. Winter, J. Kasnatscheew, *Sci. Rep.* **2020**, 10, 4390.
- [261] a) A. M. Andersson, K. Edström, *J. Electrochem. Soc.* **2001**, 148, A1100; b) *Lithium-ion Batteries. Solid-electrolyte Interphase* (Eds: P. B. Balbuena, Y. Wang), World Scientific, Singapore **2004**; c) H. Buqa, R. I. R. Blyth, P. Golob, B. Evers, I. Schneider, M. V. Santis Alvarez, F. Hofer, F. P. Netzer, M. G. Ramsey, M. Winter, J. O. Besenhard, *Ionics* **2000**, 6, 172; d) S. S. Zhang, *J. Power Sources* **2006**, 162, 1379; e) S. Zhang, M. S. Ding, K. Xu, J. Allen, T. R. Jow, *J. Electrochem. Soc.* **2001**, 4, A206; f) J. Kasnatscheew, R. W. Schmitz, R. Wagner, M. Winter, R. Schmitz, *J. Electrochem. Soc.* **2013**, 160, A1369; g) R. W. Schmitz, P. Murmann, R. Schmitz, R. Müller, L. Krämer, J. Kasnatscheew, P. Isken, P. Niehoff, S. Nowak, G.-V. Rösenthaler, N. Ignatiev, P. Sartori, S. Passerini, M. Kunze, A. Lex-Balducci, C. Schreiner, I. Cekic-Laskovic, M. Winter, *Prog. Solid State Chem.* **2014**, 42, 65; h) T. Dagger, J. Kasnatscheew, B. Vortmann-Westhoven, T. Schwieters, S. Nowak, M. Winter, F. M. Schappacher, *J. Power Sources* **2018**, 396, 519.
- [262] a) P. Niehoff, S. Passerini, M. Winter, *Langmuir* **2013**, 29, 5806; b) L. J. Fu, H. Liu, C. Li, Y. P. Wu, E. Rahm, R. Holze, H. Q. Wu, *Solid State Sci.* **2006**, 8, 113; c) V. Eshkenazi, E. Peled, L. Burstein, D. Golodnitsky, *Solid State Ionics* **2004**, 170, 83.
- [263] a) T. R. Jow, S. A. Delp, J. L. Allen, J.-P. Jones, M. C. Smart, *J. Electrochem. Soc.* **2018**, 165, A361; b) J.-P. Jones, M. C. Smart, F. C. Krause, B. V. Ratnakumar, E. J. Brandon, *ECS Trans.* **2017**, 75, 1.
- [264] Y.-X. Yao, X. Chen, C. Yan, X.-Q. Zhang, W.-L. Cai, J.-Q. Huang, Q. Zhang, *Angew. Chem., Int. Ed.* **2021**, 60, 4090.
- [265] R. Schmich, R. Wagner, G. Hörpel, T. Placke, M. Winter, *Nat. Energy* **2018**, 3, 267.
- [266] J. Kasnatscheew, M. Evertz, B. Streipert, R. Wagner, S. Nowak, I. Cekic Laskovic, M. Winter, *J. Phys. Chem. C* **2017**, 121, 1521.
- [267] D. Aurbach, M. D. Levi, E. Levi, H. Teller, B. Markovsky, G. Salitra, U. Heider, L. Heider, *J. Electrochem. Soc.* **1998**, 145, 3024.
- [268] Y. Park, S. H. Shin, H. Hwang, S. M. Lee, S. P. Kim, H. C. Choi, Y. M. Jung, *J. Mol. Struct.* **2014**, 1069, 157.
- [269] Y. Park, S. H. Shin, S. M. Lee, S. P. Kim, H. C. Choi, Y. M. Jung, *J. Mol. Struct.* **2014**, 1069, 183.
- [270] M. Balasubramanian, H. S. Lee, X. Sun, X. Q. Yang, A. R. Moodenbaugh, J. McBreen, D. A. Fischer, Z. Fu, *J. Electrochem. Soc.* **2002**, 5, A22.
- [271] a) F. Lin, I. M. Markus, D. Nordlund, T.-C. Weng, M. D. Asta, H. L. Xin, M. M. Doeff, *Nat. Commun.* **2014**, 5, 3529; b) Y. Matsuo, R. Kostecki, F. McLarnon, *J. Electrochem. Soc.* **2001**, 148, A687; c) S. Röser, A. Lerchen, L. Ibing, X. Cao, J. Kasnatscheew, F. Glorius, M. Winter, R. Wagner, *Chem. Mater.* **2017**, 29, 7733.
- [272] P. Janssen, J. Kasnatscheew, B. Streipert, C. Wendt, P. Murmann, M. Ponomarenko, O. Stubbmann-Kazakova, G.-V. Rösenthaler, M. Winter, I. Cekic-Laskovic, *J. Electrochem. Soc.* **2018**, 165, A3525.
- [273] M. A. Kraft, S. Ohno, T. Zinkevich, R. Koerver, S. P. Culver, T. Fuchs, A. Senyshyn, S. Indris, B. J. Morgan, W. G. Zeier, *J. Am. Chem. Soc.* **2018**, 140, 16330.
- [274] L. Zhou, A. Assoud, Q. Zhang, X. Wu, L. F. Nazar, *J. Am. Chem. Soc.* **2019**, 141, 19002.
- [275] A. Marcolongo, N. Marzari, *Phys. Rev. Mater.* **2017**, 1, 025402.
- [276] R. Srinivasan, A. Carson Baisden, B. G. Carkhuff, M. H. Butler, *J. Power Sources* **2014**, 262, 93.
- [277] S. Choi, M. Jeon, B.-K. Kim, B.-I. Sang, H. Kim, *Chem. Commun.* **2018**, 54, 14116.
- [278] a) R. Koerver, I. Aygün, T. Leichtweiß, C. Dietrich, W. Zhang, J. O. Binder, P. Hartmann, W. G. Zeier, J. Janek, *Chem. Mater.* **2017**, 29, 5574; b) S.-K. Jung, H. Gwon, S.-S. Lee, H. Kim, J. C. Lee, J. G. Chung, S. Y. Park, Y. Aihara, D. Im, *J. Mater. Chem. A* **2019**, 7, 22967.
- [279] R. Koerver, W. Zhang, L. de Biasi, S. Schweidler, A. O. Kondrakov, S. Kolling, T. Brezesinski, P. Hartmann, W. G. Zeier, J. Janek, *Energy Environ. Sci.* **2018**, 11, 2142.
- [280] M. Falco, S. Ferrari, G. B. Appetecchi, C. Gerbaldi, *Mol. Syst. Des. Eng.* **2019**, 4, 850.
- [281] D. Hlushkou, A. E. Reising, N. Kaiser, S. Spannenberger, S. Schlabach, Y. Kato, B. Roling, U. Tallarek, *J. Power Sources* **2018**, 396, 363.
- [282] N. Kaiser, S. Spannenberger, M. Schmitt, M. Cronau, Y. Kato, B. Roling, *J. Power Sources* **2018**, 396, 175.
- [283] T. Shi, Q. Tu, Y. Tian, Y. Xiao, L. J. Miara, O. Kononova, G. Ceder, *Adv. Energy Mater.* **2019**, 2, 1902881.
- [284] a) S. Choi, M. Jeon, J. Ahn, W. D. Jung, S. M. Choi, J.-S. Kim, J. Lim, Y.-J. Jang, H.-G. Jung, J.-H. Lee, B.-I. Sang, H. Kim, *ACS Appl. Mater. Interfaces* **2018**, 10, 23740; b) T. Asano, S. Yubuchi, A. Sakuda, A. Hayashi, M. Tatsumisago, *J. Electrochem. Soc.* **2017**, 164, A3960; c) J. Landesfeind, A. Eldiven, H. A. Gasteiger, *J. Electrochem. Soc.* **2018**, 165, A1122.
- [285] T. Krauskopf, B. Mogwitz, H. Hartmann, D. K. Singh, W. G. Zeier, J. Janek, *Adv. Energy Mater.* **2020**, 10, 2000945.
- [286] J.-M. Doux, H. Nguyen, D. H. S. Tan, A. Banerjee, X. Wang, E. A. Wu, C. Jo, H. Yang, Y. S. Meng, *Adv. Energy Mater.* **2020**, 10, 1903253.
- [287] C. Yang, L. Zhang, B. Liu, S. Xu, T. Hamann, D. McOwen, J. Dai, W. Luo, Y. Gong, E. D. Wachsman, L. Hu, *Proc. Natl. Acad. Sci. U. S. A.* **2018**, 115, 3770.
- [288] Y. Ye, L. H. Saw, Y. Shi, A. A. O. Tay, *Appl. Therm. Eng.* **2015**, 86, 281.
- [289] Y. Ye, Y. Shi, A. A. O. Tay, *J. Power Sources* **2012**, 217, 509.
- [290] Y. Ye, L. H. Saw, Y. Shi, K. Somasundaram, A. A. O. Tay, *Electrochim. Acta* **2014**, 134, 327.
- [291] M. Keyser, A. Pesaran, Q. Li, S. Santhanagopalan, K. Smith, E. Wood, S. Ahmed, I. Bloom, E. Dufek, M. Shirk, A. Meintz, C. Kreuzer, C. Michelbacher, A. Burnham, T. Stephens, J. Francfort, B. Carlson, J. Zhang, R. Vijayagopal, K. Hardy, F. Dias, M. Mohanpurkar, D. Scofield, A. N. Jansen, T. Tanim, A. Markel, *J. Power Sources* **2017**, 367, 228.
- [292] D. Chen, J. Jiang, G.-H. Kim, C. Yang, A. Pesaran, *Appl. Therm. Eng.* **2016**, 94, 846.
- [293] C. Wang, G. Zhang, L. Meng, X. Li, W. Situ, Y. Lv, M. Rao, *Int. J. Energy Res.* **2017**, 41, 2468.

- [294] Y. Zheng, Y. Shi, Y. Huang, *Appl. Therm. Eng.* **2019**, *147*, 636.
- [295] S.-Y. Choe, X. Li, M. Xiao, *World Electr. Veh. J.* **2013**, *6*, 782.
- [296] S. S. Zhang, *J. Power Sources* **2006**, *161*, 1385.
- [297] Z. Guo, B. Y. Liaw, X. Qiu, L. Gao, C. Zhang, *J. Power Sources* **2015**, *274*, 957.
- [298] A. Aryanfar, D. Brooks, B. V. Merinov, W. A. Goddard, A. J. Colussi, M. R. Hoffmann, *J. Phys. Chem. Lett.* **2014**, *5*, 1721.
- [299] J. Amanor-Boadu, A. Guiseppi-Elie, E. Sánchez-Sinencio, *Energies* **2018**, *11*, 2162.
- [300] B. Lu, Y. Zhao, Y. Song, J. Zhang, *Electrochim. Acta* **2018**, *288*, 144.
- [301] a) B. Kwak, M. Kim, J. Kim, *Electronics* **2020**, *9*, 227;
b) N. Majid, S. Hafiz, S. Arianto, R. Y. Yuono, E. T. Astuti, B. Prihandoko, *J. Phys.: Conf. Ser.* **2017**, *817*, 012008.



Manuel Weiss received his M.Sc. degree in Advanced Materials from Justus Liebig University Giessen. Afterward, he obtained his Ph.D. in the field of physical chemistry under supervision of Prof. Jürgen Janek. Currently, he is working as a postdoctoral researcher in Prof. Janek's group, investigating interfacial processes between different ionic conductors, liquid electrolytes for metal–oxygen batteries, and structure–property relationships in solid electrolytes.



Johannes Kasnatscheew studied chemistry at University of Münster and was granted an M.Sc. degree in 2012 under the supervision of Prof. Martin Winter. He continued his research in Prof. Winter's group in the department of "Münster's Electrochemical Energy Technology" (MEET) and obtained his Ph.D. in Physical Chemistry in 2017. That same year he joined the Helmholtz-Institute Münster (HIMS) "Ionics in Energy Storage" (IEK-12), an institute branch of Research Center Jülich, as a Post-Doc in Prof. Winter's group. His research focuses on failure diagnosis within Li-Ion batteries (LIBs) and all-solid-state-batteries at harsh conditions, in particular on electrolyte- and cathode materials.



Yehonatan Levartovsky received his B.Sc. in Chemistry from Tel-Aviv University in 2015, and his M.Sc. in Chemistry from the Hebrew University in Jerusalem in 2018. He is about to complete his Ph.D. in Chemistry under the guidance of Prof. Doron Aurbach at Bar-Ilan University, and then he will begin a fellowship at the UCL Electrochemical Innovation Lab. Currently, he is working on the design and synthesis of high-energy cathode materials for electric vehicles.



Natasha Ronith Levy received her B.Sc. degrees in Materials Science and Engineering (2016) and Chemistry (2016) and M.S. degree (2018) in Material Science and Engineering, all from the Technion-Israel Institute of Technology, Haifa, Israel. She started a Ph.D. in the Electrochemistry and Energy Storage field under the supervision of Prof. Y. Ein-Eli in 2018. Her research interests are focused on developing innovative air cathodes and study nonaqueous electrolytes for aluminum–air batteries.



Thomas Waldmann studied chemistry at Ulm University and received his Ph.D. degree in 2012. He joined the Zentrum für Sonnenenergie- und Wasserstoff-Forschung Baden-Württemberg (ZSW) in 2011 where he started working on degradation mechanisms of Li-ion batteries. His interests are focused on fast-charging, unraveling of aging mechanisms, especially on Li plating, knowledge-based extension of battery life-time, as well as interactions of safety and aging. Since 2018, he is team leader for Post-Mortem analysis and aging mechanisms at ZSW.



Doron Aurbach is full professor at the Department of Chemistry, which he chaired during 2001–2005, leading the electrochemistry group (founded in 1985) at Bar Ilan University and the Israel National Research Center for Electrochemical Propulsion (INREP). Professor Aurbach's group studies the electrochemistry of active metals, non-aqueous electrochemistry, intercalation processes, electronically conducting polymers, and water desalination and develop rechargeable batteries and supercapacitors with high energy density including spectroscopic methods for sensitive electrochemical systems. He has published over 720 papers and 30 patents, cited over 77 000 times. He is technical editor for the Journal of the Electrochemical Society (JES).



Yair Ein-Eli graduated from Bar-Ilan University (1995) and he joined (2001) the Department of Materials Engineering at the Technion-Israel Institute of Technology, after serving 3 years as the VP of R&D of Electric Fuel Ltd. (Israel). Before that (1995–1998), he was a post-doctoral fellow at Covalent Assoc. Inc. (MA, USA). Current research projects of Yair in the field of power sources involve advanced materials for Li-ion batteries, alkaline batteries, metal–air cells, and fuel cells. He is also engaged in research and development of electroplating methods, as well as corrosion inhibitors studies.



Jürgen Janek holds a chair for Physical Chemistry at Justus Liebig University in Giessen (Germany) and is scientific director of BELLA, a joint lab of BASF SE and KIT in Karlsruhe/ Germany. He received his doctoral degree in Physical Chemistry and was visiting professor at Seoul National University, Tohoku University, and Université d'Aix-Marseille. His research spans a wide range from transport studies in mixed conductors and at interfaces to in situ studies in electrochemical cells. Current key interests include all-solid state batteries, solid electrolytes, and solid electrolyte interfaces. He is particularly interested in kinetics at interfaces.